UNLV Theses, Dissertations, Professional Papers, and Capstones

2009

# Zirconia-magnesia inert matrix fuel and waste form: Synthesis, characterization and chemical performance in an advanced fuel cycle

Kiel Steven Holliday
*University of Nevada, Las Vegas*

## Repository Citation

ZIRCONIA-MAGNESIA INERT MATRIX FUEL AND WASTE FORM:

SYNTHESIS, CHARACTERIZATION AND CHEMICAL

PERFORMANCE IN AN ADVANCED FUEL CYCLE

by

Kiel Steven Holliday

Bachelor of Science
California State University, San Marcos
2005

A dissertation submitted in partial fulfillment
of the requirements for the

**Doctor of Philosophy Degree in Radiochemistry**
**Department of Chemistry**
**College of Sciences**

**Graduate College**
**University of Nevada, Las Vegas**
**August 2009**

ABSTRACT

**Zirconia-Magnesia Inert Matrix Fuel and Waste Form:**
**Synthesis, Characterization and Chemical**
**Performance in an Advanced Fuel Cycle**

by

Kiel Steven Holliday

Dr. Ken Czerwinski, Examination Committee Chair
Professor of Chemistry
Chair of the Department of Radiochemistry
University of Nevada, Las Vegas

There is a significant buildup in plutonium stockpiles throughout the world, because
of spent nuclear fuel and the dismantling of weapons. The radiotoxicity of this material
and proliferation risk has led to a desire for destroying excess plutonium. To do this
effectively, it must be fissioned in a reactor as part of a uranium free fuel to eliminate the
generation of more plutonium. This requires an inert matrix to volumetrically dilute the
fissile plutonium. Zirconia-magnesia dual phase ceramic has been demonstrated to be a
favorable material for this task. It is neutron transparent, zirconia is chemically robust,
magnesia has good thermal conductivity and the ceramic has been calculated to conform
to current economic and safety standards. This dissertation contributes to the knowledge
of zirconia-magnesia as an inert matrix fuel to establish behavior of the material
containing a fissile component. First, the zirconia-magnesia inert matrix is synthesized in
a dual phase ceramic containing a fissile component and a burnable poison. The
chemical constitution of the ceramic is then determined. Next, the material performance
is assessed under conditions relevant to an advanced fuel cycle. Reactor conditions were
assessed with high temperature, high pressure water. Various acid solutions were used in
an effort to dissolve the material for reprocessing. The ceramic was also tested as a waste

form under environmental conditions, should it go directly to a repository as a spent fuel. The applicability of zirconia-magnesia as an inert matrix fuel and waste form was tested and found to be a promising material for such applications.

TABLE OF CONTENTS

# LIST OF TABLES

## LIST OF FIGURES

ACKNOWLEDGEMENTS

CHAPTER 1


INTRODUCTION

1.1 Inert matrix fuels: general description

Current nuclear power technology uses a small range of different fuels including

uranium oxide based fuel (UOX), mixed oxide fuel (MOX) or metal fuel. (1). No matter

what the fuel type, it is still based on the fissile material ($^{235}$U or $^{239}$Pu) being

volumetrically diluted by the most abundant uranium isotope, namely $^{238}$U. This volume

of $^{238}$U leads to the production of plutonium through neutron capture and the subsequent

beta decay of $^{239}$U and $^{239}$Np (half lives of 23.47 minutes and 2.355 days, respectively) to

$^{239}$Pu with a half life of 24,100 years. Because of this and the dismantling of nuclear

weapons, there is a significant buildup of civil plutonium stockpiles (2). It was found

that at the end of 2003 the total amount of civil plutonium was about 1,600 tonnes (3). It

is estimated to be on the order of 1,800 tonnes today (2).

The current strategy for destroying plutonium is through fission in mixed oxide fuel.

Present regulations allow for about 7 % plutonium (containing 65 % fissile plutonium

isotopes) in MOX fuel. This fuel composition puts the net plutonium consumption at

unity and is only successful at altering the isotopics of the fuel (2). It only addresses

proliferation concerns and does nothing to reduce the radiotoxicity of the spent fuel,

which is dominated by plutonium from ~$10^2$ to $10^5$ years (2, 4). To eliminate the

production of plutonium over the life of the fuel, a uranium free fuel must be developed.

In uranium free fuel the fissile component, typically Pu-239, is volumetrically diluted by

a neutron transparent matrix. This composite is known as an inert matrix fuel. As can be

1

seen in Table 1, such a mixture using plutonium as the fissile component can have a net consumption of 142 kg/TWhe (2).

Table 1: Comparison of the net plutonium and minor actinide (MA) consumption rate (in kg/TWhe) for different fuel loadings (2).

| Reactor type | Net consumption rate (kg/TWhe) | | Reference |
| --- | --- | --- | --- |
| | Pu | MA | |
| LWR, 100% UOX | -25 | -5 | OECD/NEA (2002, p. 70) |
| LWR, 30% MOX | 1 | -9 | OECD/NEA (2002, p. 70) |
| LWR, 100% MOX | 62 | -18 | OECD/NEA (2002, p. 70-71) |
| LWR, 100% Th/Pu core | 115 | -9 | Phlippen et al. (2006) |
| LWR, 100% Pu-IMF | 142 | -23 | Akie et al. (1999) |

One study showed that 98 % of the Pu-239 could be burnt in an existing pressurized water reactor, while 73.24 % and 81.39 % of the total plutonium was fissioned for reactor grade and weapons grade plutonium, respectively (4) [Table 2].

Table 2: Plutonium isotopic balance in the inert matrix fuel by Lombardi and Mazzola (4).

| | Reactor Grade Pu | | | Weapons Grade Pu | | |
| --- | --- | --- | --- | --- | --- | --- |
| | BOL | EOL | Burnt % | BOL | EOL | Burnt % |
| Pu-239 | 58 | 1.06 | 98.17 | 93 | 1.15 | 98.76 |
| Pu-240 | 24 | 10.26 | 57.25 | 6 | 7.51 | - |
| Pu-241 | 13 | 6.17 | 52.56 | 0.8 | 5.11 | - |
| Pu-242 | 5 | 9.27 | - | 0.2 | 4.83 | - |
| Fissile Pu | 71 | 7.23 | 89.82 | 93.8 | 6.26 | 93.33 |
| Fertile Pu | 29 | 19.53 | 32.64 | 6.2 | 12.34 | - |
| Total Pu | 100 | 26.76 | 73.24 | 100 | 18.61 | 81.39 |
| Fiss./fert. Pu | 2.45 | 0.37 | | 15.13 | 0.51 | |

The concept of an inert matrix fuel is not new, and research on the subject was first performed in the early sixties (5-7). Due to the postponement and perhaps abandonment of fast breeder reactors as a means of plutonium disposal and the growing concerns of proliferation and waste radiotoxicity, inert matrix fuels have seen a renewed interest since the early nineties (5). Inert matrix fuels have been identified as useful to three different applications with three different time scales. The first application would be deployment in current pressurized light water reactors (PWRs). This would enable the burning of plutonium with current technology making it the fastest way of utilizing inert matrix fuel. The second would be to burn plutonium via inert matrix fuel in fast reactors, which could be envisioned on an intermediate time scale. Lastly, minor actinides could be fissioned in an inert matrix after separation by a recycling scheme. This would incorporate various new technologies and would therefore be considered on the longest time scale (6). The focus of the studies presented in this work will be to address the deployment of an inert matrix fuel in existing PWRs on the shortest time scale.

For an inert matrix fuel to be deployed in current PWRs it must conform to a series of guidelines, if it is to be used in the near future. By definition the inert matrix fuel must be neutron transparent. The material selected should also be easy to manufacture, have a widespread availability and a low cost of starting material. The material also has to have favorable material properties. This includes: high melting point, good thermal conductivity and an absence of phase changes and significant dissociation at high temperatures. In addition nuclear fuel needs to be compatible with reactor components including cladding (Zircaloy or steel) and coolant (high temperature water). A potential

inert matrix fuel needs to have good mechanical properties to provide mechanical stability in the harsh environment of a nuclear reactor. Lastly, the material must exhibit good stability against radiation. This will prevent it from crystal structure changes as well as swelling and other undesirable affects. A detailed explanation of the requirements summarized here can be found in Matzke et. al. (5).

The process of directing research efforts to find an appropriate inert matrix fuel candidate is outlined in a paper by Degueldre and Paratte (7). The first step is to identify material with appropriate neutronics properties through simple cell calculations. This is done to characterize the reactivity of the inert matrix components, the fissile vector, and any burnable poison that is used to improve the neutronics. Next the physico-chemical screening is performed to identify material with favorable thermodynamic, compatibility and solubility properties. This is mainly done through literature review of material studied for both fuel and waste form applications. Material that shows promise for application as an inert matrix fuel is then synthesized. It should be noted that material used for this purpose typically has cerium oxide used as a plutonium oxide homolog. The material is then characterized using X-ray diffraction to identify phases present and theoretical density, which is then compared with geometric density. At the microscopic level, both optical and scanning electron microscopes are used to study pore space and grain structure. The characterization is completed by irradiation studies via accelerators or research reactors. These studies monitor such aspects as swelling, crystal structure, temperature and mechanical behavior. The next step for potential material would be advanced nuclear engineering calculations based on the precept: "The new fuel must be conceived such as to be suitable for loading into present-day power reactors, without any

geometrical modifications of the core (7)." This limits the reactor design, total power, length of cycles and safety restraints to the plant. It does not limit how the fuel is loaded. Therefore, several concepts have been proposed including a homogenous IMF core, heterogeneous IMF and $UO_2$ core or a homogenous (with respect to neutronic calculations) IMF and $UO_2$. Finally, these calculations are used to address issues specific to inert matrix fuel such as high burnup and core behavior with respect to accident and transient conditions. One aspect of the fuel that needs to be determined is the fate of the spent fuel. It can be sent directly to the repository in the case of a high burn-up fuel that is very chemically stable or to a reprocessing scheme in which the material is recycled mainly to reduce the radiotoxicity of the minor actinides and fission products produced. A more detailed discussion of the methodology discussed here can be found in the literature (7).

This methodology has been applied to inert matrix fuel for fast reactors and accelerator systems (8), but the most advanced has been for existing light water reactors. It has been shown that the life of an inert matrix fuel can be as much as 1,000 days with a loading of 20 % standard $UO_2$ fuel with inert matrix fuel making up the other 80 % in current reactor designs (9). The type of inert matrix can have little effect on certain aspects of the neutronics, such as criticality (10). In such cases the thermal properties of the inert matrix become significant. Studies have been performed in an attempt to identify such materials that have favorable thermal properties as described earlier (11). These thermal properties have been incorporated into detailed calculations with various inert matrix fuels to determine temperature coefficient, moderator coefficient and boron reactivity worth (12). These calculations indicated that thermal conductivity and melting

point have drastic effects on accident performance related to reactivity induced and moderator void incidents. Thorium oxide additives or burnable poisons such as erbium oxide were shown to greatly improve the performance of the inert matrix fuel under these scenarios (12). The addition of thorium does drastically change the characteristics of an inert matrix fuel, as thorium is a fertile fuel [Figure 1]. Because this results in the production of U-233 it replaces one proliferation concern with another, even though this is mitigated through the presence of U-232. The addition of a small amount (5-7 %) of natural uranium will virtually eliminate this proliferation risk with only a moderate decrease in burnup potential (13).

These studies have led to the identification of several potential inert matrix fuels that each have their own advantages, but without the identification of a perfect candidate. Metals have superior thermal conductivity, but tend to have higher corrosion rates and low compatibility with reactor components such as cladding (14). Carbides have also been investigated, but have a low tolerance to radioactivity in aqueous media (15). At high doses the carbide structure weakens making it more soluble in aqueous media. Nitrides were also explored as an option for inert matrix fuels, but manufacturing
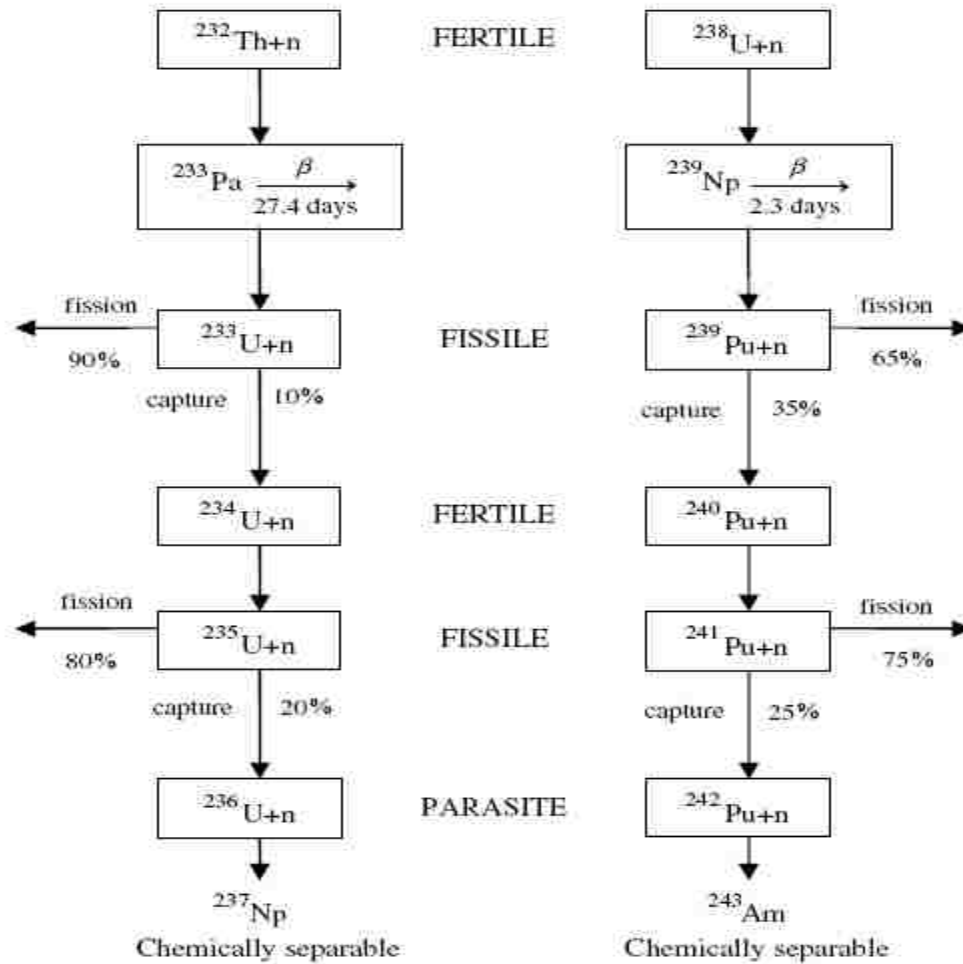
Figure 1: Analogy in thorium and uranium fertilization (1).

challenges have proven to be difficult to overcome (16). Ordered fluorite derivatives such as spinel ($MgAl_2O_4$) (20, 21) and zirconium neodymium pyrochlore ($Zr_2Nd_2O_7$) (17) have also been studied in great detail, but have been found to undergo structural changes and significant swelling due to radiation. The mostly widely studied material, however, is cubic stabilized zirconium oxide or zirconia. The research on this material in recent years has made this the most promising material for near term deployment in existing reactors (2).

1.2 Zirconia as an inert matrix fuel

More research has been done on cubic stabilized zirconia than on any other inert matrix material.  Because of this, its strengths and weakness are well studied and solutions to its shortcomings have been investigated to a greater degree than other matrices.  Burnup calculations have been performed with zirconia as the inert matrix specifically (18).  It was found that more than 95 % of the Pu-239 and more than 77 % of the total plutonium could be burnt in a zirconia matrix.  In addition to plutonium, americium and neptunium could also be fissioned to reduce their quantities by 75 % and 85 % respectively (18).  The idea of burning minor actinides in addition to plutonium by a zirconia inert matrix fuel has also been investigated by others and shows promise on a longer time scale (19).  These burnup calculations were then verified by experimentation in reactor irradiation studies and showed reasonable agreement (20).

Next calculations were performed to determine the materials thermal properties under irradiation in a pressurized water reactor (26-28).  It was found through these calculations that the addition of plutonium, erbium, or yttrium in the zirconia solid solution did not affect the thermal properties of the matrix to a large extent.  This is true not only for the concentration of the substituting ions, but also for the distribution of the foreign atoms.  What did, however, affect the thermal conductivity of the matrix were oxygen vacancies.  As oxygen vacancies increased, the thermal conductivity of the material decreased (21).  In this way, adding lower valent cations to the zirconia solid solution does lower the thermal conductivity, but only because of the influence on oxygen vacancy and not because of the cation itself.  Therefore, there should be no difference in thermal properties for the addition of tetravalent species and the choice of element given a

particular oxidation state should not affect thermal conductivity. This lends itself to a greater flexibility in choice of stabilizer and burnable poison selection. These calculations were verified by monitoring temperatures during reactor irradiations (30, 31).

To perform these studies simulated inert matrix fuel was synthesized (22). A significant amount of research was devoted to optimizing the synthesis for the desired properties such as density and microstructure (23). Various synthesis methods have been employed to help improve materials properties including microwave synthesis (24), coprecipitation methods (25) and the use of heterogeneous pellets (26). The density of the synthesized pellet is of particular importance and has been studied in depth (27). In addition to physical properties, phase relationships were also examined for various components that could be incorporated into a zirconia based inert matrix fuel. In one study the phase relationship between zirconia, thoria, and urania was examined (28). It was found that zirconia and thoria were not mutually soluble while urania was distributed evenly throughout both phases. The phase relationship between zirconia and plutonia was also examined and the cubic phase transition was examined in more detail (29). The phase relationship between zirconia and various burnable poisons was also calculated (30). In addition to various burnable poisons, these materials were then synthesized and characterized with various stabilizers including yttrium, lanthanum and praseodymium (31).

Once the material is synthesized to a suitable density, it can be characterized. A review of material characterization studies summarizes a great deal of the work that has been performed on the physical properties of zirconia (32). It was found that

microstructure has a large influence on the strength of the material and therefore the fabrication process is important as it is what dictates grain size through initial mixing and temperature and duration of sintering. Zirconia was, however, found to be comparable to urania in strength and durability and is therefore not believed to deviate from experience gained with $UO_2$ as a nuclear fuel.

After synthesis and characterization the simulated inert matrix fuel generally undergoes irradiation studies either in a reactor or with an accelerator driven system. Accelerator driven systems have the advantage of being able to impart a large dose to a sample over a relatively short time. It is also possible to study the fission gas retention in an inert matrix with an accelerator system if a noble gas is used as the bombarding ion (33). From this it was found that fission gases should not escape the fuel pellet. They do have a higher mobility in zirconia than in urania because of higher operating temperature. Therefore, it should be noted that increasing the thermal conductivity of the material would correct this potential problem. In terms of radiation damage single crystal zirconia bombarded by an accelerator driven system behaved similar to that of $UO_2$ (34). Because of its potential as a highly radiation resistant inert matrix fuel, zirconia has undergone several reactor irradiations to determine its radiation tolerance and performance in reactor conditions. It was shown in irradiations that both calcium and yttrium stabilized zirconia exhibit stable and consistent irradiation behavior and that homogenous distribution of the fissile material was superior to a heterogeneous distribution (35). A more recent paper on the irradiations also reports a higher fission gas mobility as compared to $UO_2$ fuel due to the higher operating temperature as previously discussed (36). That study still concludes that zirconia has a good radiation tolerance and has been shown to be chemically inert to

reactor components. There is evidence of swelling due to irradiation in earlier studies, but only in samples synthesized by a dry synthesis route of mixing the oxide powders (37). This suggests that it is a problem that may be overcome through better synthesis methods, such as coprecipitation. A review on the irradiation of zirconia inert matrix fuel reports good radiation tolerance, low fission gas release comparable to MOX and excellent chemical inertness (38). The only problems that have arisen are fission gas mobility and unfavorable reaction to accident conditions due to low thermal conductivity, which could be improved through the addition of a secondary phase with higher thermal conductivity (39). Magnesium oxide has been proposed as a secondary phase to improve thermal conductivity could be magnesium oxide.

## 1.3 Magnesium oxide as an inert matrix fuel

Magnesium oxide is another material well suited to be an inert matrix fuel for nuclear applications. It is neutron transparent and has the potential for extremely high burnup, especially in the case of americium and curium (14). This would indicate that if magnesium oxide were added to our inert matrix, it would not significantly change the neutronics characteristics from previous studies. The neutronics calculation for MgO was performed to analyze the material in various accident scenarios and was found to behave as good as or better than $UO_2$ (14). Because of this potential, material was synthesized and the process for making magnesium oxide inert matrix fuel was optimized (40). It was possible through the dry route synthesis of mixing oxide powders and the sol-gel process to synthesize simulated fuel pellets with suitable densities.

Samples were then irradiated in research reactors to assess their performance. One such irradiation was performed to determine the ability of MgO to be used as an inert matrix for the burning of minor actinides, such as americium and curium (41). It was determined that magnesium oxide was well suited for such a task. It had a high radiation tolerance that was tested in multiple irradiation studies (42). Even as a dual phase mixture with pyrochlore, magnesium oxide exhibited superior radiation resistance and excellent neutronic properties (43). There was one negative result that was discovered in a particular irradiation involving MgO as an inert matrix for $UO_2$. In this case the $UO_2$ experienced volume swelling due to irradiation and cracked the magnesium oxide inert matrix (44). This could be mitigated if the fissile material was incorporated into a solid solution such as zirconia. In that case it would not undergo swelling and crack the magnesium oxide matrix. Other than this single event, which had more to do with $UO_2$ than the magnesium oxide (several other potential inert matrix fuels also cracked under similar conditions) the irradiations have been successful. In fact, it was shown that the magnesium oxide matrix exhibited less than 1 % volumetric swelling and less than 15 % fission gas release (45) and these were confirmed for as a dual phase inert matrix fuel in future irradiations (46). These studies point to magnesium oxide as a suitable material in terms of radiation resistance and neutronic properties for an inert matrix fuel.

The real advantage to magnesium oxide is not its radiation resistance or neutronic properties, but its thermal characteristics. Magnesium oxide has a much higher thermal conductivity than standard $UO_2$ or MOX fuel. Because of this, it is possible to use magnesium oxide as a secondary phase to improve the thermal conductivity of a material (5). Magnesium oxide has a low mutual solubility with the actinides and thereby retains

it superior heat transfer properties as a pure phase. This concept was exploited in the case of MgO and $Nd_2Zr_2O_7$ pyrochlore as a dual phase inert matrix fuel. Molecular dynamics calculations were carried out to estimate the thermal conductivity of the simulated fuel and to determine its dependence on grain size and temperature (47). It was found that the thermal conductivity of the material could be brought to similar values of existing fuels with the addition of magnesium oxide. Magnesium oxide also exhibited acceptable mechanical behavior that was suitable to its use as a nuclear fuel (32).

Magnesium oxide, as with other material, is not the perfect inert matrix fuel. The problem is its compatibility with reactor components. Specifically, with coolant water in the event of a cladding failure the magnesium oxide is hydrolyzed to magnesium hydroxide, which is then dissolved (40). This results in releasing the fissile phase from the fuel and although it is not soluble, it leaves the fuel pin via coolant flow before settling in the reactor vessel. To improve the corrosion resistance of the magnesium oxide a highly durable secondary phase such as zirconia could be added to retard the dissolution of the magnesia phase.

1.4 Dual phase zirconia-magnesia inert matrix fuel

The zirconia-magnesia system has been under investigation for nearly a century. The phase diagram that is currently in use was first proposed in an incomplete form in 1933 by Ebert and Cohn (48). Since then phase boundaries have been more accurately determined and more temperatures have been investigated. In 1952, it was established that at 2000$^o$C the range of a single phase of cubic solid solution existed between 5 and 16 mol. % MgO (49). It was also demonstrated that magnesia was adequate to stabilize

the cubic phase at high temperatures. Later, these phase relationships were found to hold true at 1600$^{o}$C (50). Specifically, it was determined that the limit of isomorphic substitution for magnesium oxide in cubic zirconia at 1600$^{o}$C was 16 mol %. Studies were also performed on ternary systems by adding different components such as calcium and yttrium to the zirconia-magnesia system (60-61). In addition to chemical properties, the physical properties such as hardness and fracture strength were also established for these materials (51).

Lately, this system has been investigated for its potential as an inert matrix fuel (52). A synthesis method was established for a dry route synthesis of mixing oxide powders to create a high density zirconia-magnesia ceramic that included erbium (53). It was also determined that the addition of zirconia to magnesia resulted in an exponential decrease in the rate of mass loss due to corrosion by 300$^{o}$C water (53). It should be noted that the corrosion studies were done under static conditions. The presence of boric acid also lowered the corrosion rate of the material through the formation of a magnesium hydrated borate by the equation shown below:

$$1) \; MgO + H_3BO_3 \rightarrow Mg(OH)BO_2 + H_2O$$
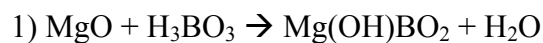
A scheme for the corrosion of magnesia in the presence of zirconia was also proposed. This scheme explains the increased corrosion resistance of magnesia in the presence of zirconia through the path that the corrosion takes. It is proposed that in pure magnesia the corrosion progresses along grain boundaries resulting in swelling and cracking to remove entire grains that are subsequently dissolved. In the presence of adequate amounts of zirconia (nearly 50 vol. %) it is proposed that the swelling is insufficient to break off entire grains and because of this the corrosion only propagates along the face of

the grain. This mechanism progresses much slower (53). A diagram of this proposed scheme in the presence of zirconia is shown in Figure 2.
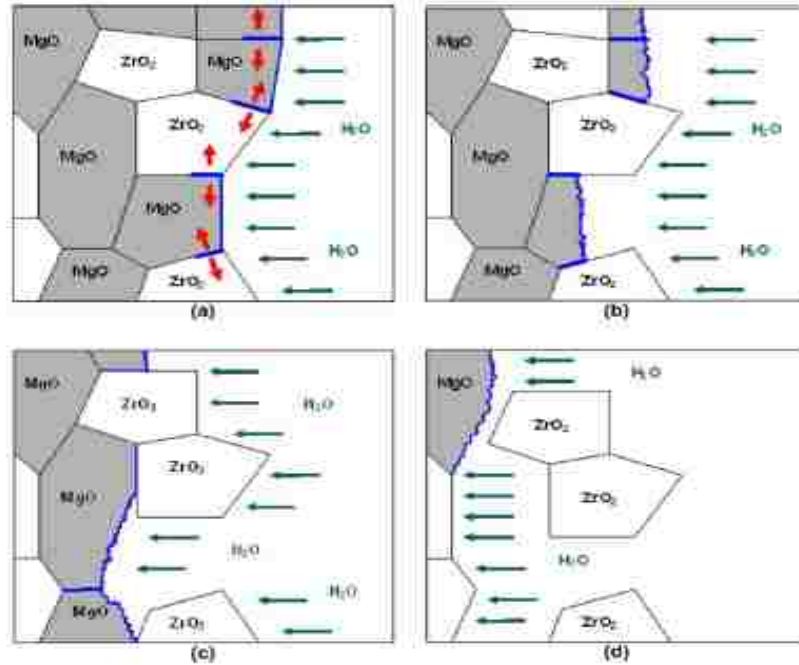


Figure 2: Schematic of the hydration process in zirconia-magnesia ceramics as proposed by Medvedev et. al. (53).

Once the hydration resistance was established, the second main issue to the feasibility of zirconia-magnesia inert matrix fuel was thermal conductivity. Material was synthesized in the same manner described above incorporating erbium into a zirconia-magnesia matrix and the thermal conductivity was determined for compositions with 40-60 wt. % magnesium oxide (54). It was found that all compositions that have greater than 40 wt. % magnesium oxide, regardless of the presence of erbium oxide, have a thermal conductivity greater than that of standard $UO_2$ fuel as can be seen in Figure 3 and Figure 4.
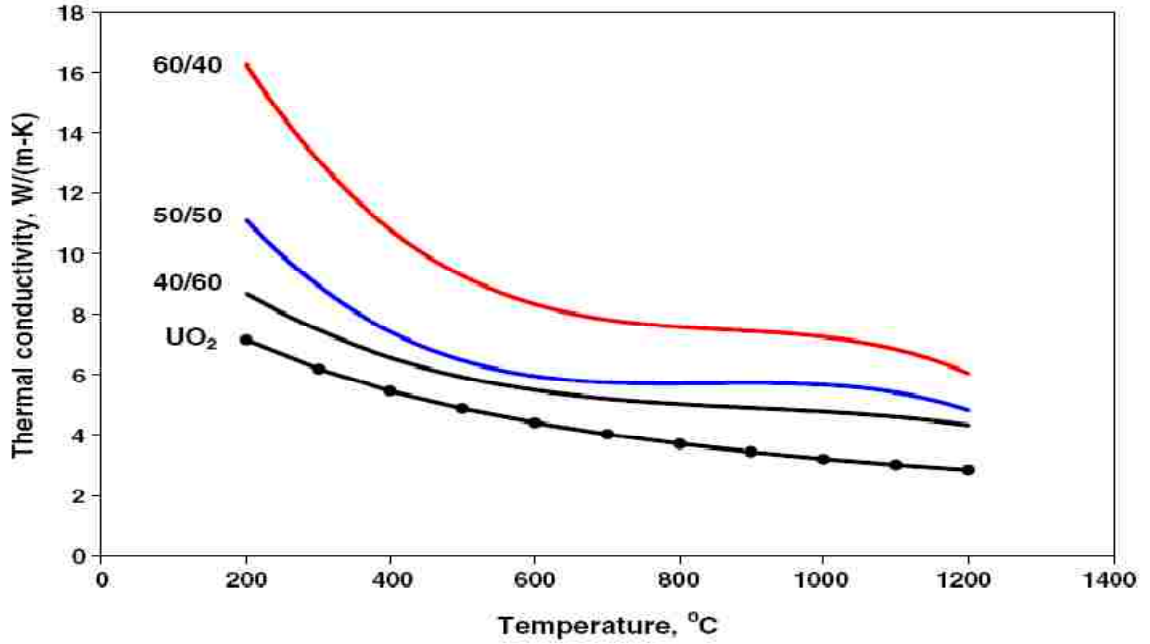
Figure 3: Thermal conductivity calculated from experimental data on the binary system
ZrO$_2$-MgO as compared to UO$_2$ (54).
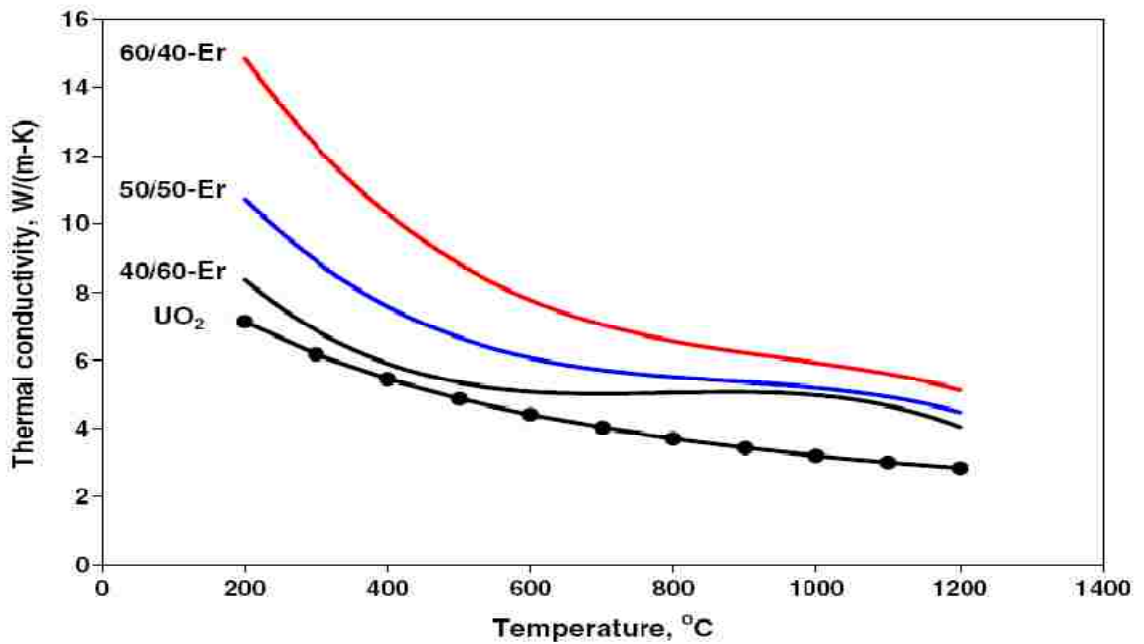


Figure 4: Thermal conductivity calculated from experimental data on the ternary
system ZrO$_2$-MgO-ErO$_{1.5}$ as compared to UO$_2$ (54).

The feasibility of recycling the zirconia-magnesia inert matrix fuel was also explored by examining its solubility in nitric acid, which is the media of choice for current reprocessing schemes. Ceramic samples were added to concentrated nitric acid and heated to 55 $^{o}$C with stirring. Analysis was done by mass throughout the experiment and samples were characterized by microscopy at the conclusion of the study (54). It was found that all of the magnesia phase was soluble in nitric acid and dissolved throughout the volume of the pellet. The zirconia phase was not soluble to any degree in the concentrated nitric acid. This dissolution study resulted in no change in pellet dimension, but a drastic mass loss due to the dissolution of the magnesia, resulting in a porous zirconia ceramic (54). These results would indicate that nitric acid alone is not suitable for dissolving this inert matrix fuel for reprocessing. It should be noted that these samples did not contain a fissile component or fissile component homolog.

Samples were prepared in an effort to demonstrate the synthesis of zirconia-magnesia inert matrix fuel containing plutonium oxide as the fissile component (55). The solid oxides of zirconium and magnesium were mixed, calcined, pressed, and ground to less that 250 μm before being mixed with plutonium oxide and pressed into pellets. The green pellets were then sintered under air to 1700 $^{o}$C for 7.5 hours. This resulted in two dominant phases of pure cubic MgO (periclase) and a cubic zirconia solid solution of zirconium, magnesium and plutonium oxides. There was, however, another minor phase of plutonium oxide inclusions as can be seen in Figure 5 (55). These plutonium oxide inclusion contained some dissolved zirconium and magnesium oxide. These results indicate that the synthesis method was inadequate at making a two phase mixture capable

of dissolving all of the fissile material and no attempt was made to incorporate a burnable poison into these samples.
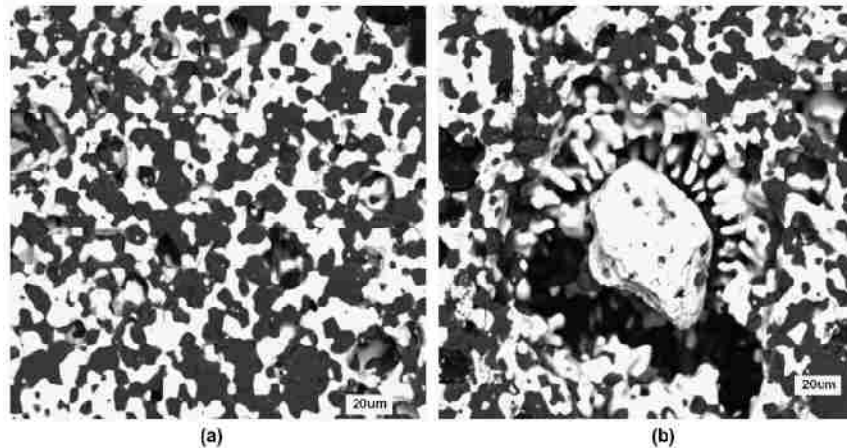


Figure 5: Key microstructural features identified in the sample are a two-phase matrix (a) and a PuO2-rich inclusion (b) (55).

## 1.5 Research goals and objectives

From the previous studies it is possible to identify research needs in order to determine the feasibility of zirconia-magnesia inert matrix fuel. First, it must be demonstrated that a dual phase zirconia-magnesia inert matrix fuel can be synthesized with both a fissile component and a burnable poison. Secondly, the material dissolution behavior under environmental conditions must be investigated to assess its suitability as a waste form should this fuel be incorporated into a once through fuel cycle. Third, a suitable means of dissolving the material must be engineered if reprocessing is going to be possible with this advanced fuel form. Lastly, the irradiation behavior of this material should be investigated to confirm that there is no change in structure, so that dissolution studies and long term behavior are validated.

The first objective, demonstrating that a dual phase zirconia-magnesia inert matrix fuel can be synthesized with a fissile component and burnable poison is addressed in Chapter 3. This was done by utilizing a coprecipitation method to synthesize ceramics containing zirconium oxide, magnesium oxide, erbium oxide (as the burnable poison) and a fissile component. Three elements were used as the fissile component. Cerium oxide was first used as a plutonium oxide homolog, so that procedures could be established in the absence of radioactivity and to assess the suitability of cerium as a plutonium homolog. Next, uranium oxide was used as a fissile component and plutonium homolog, which was believed to be more suitable because of its similar oxidation-reduction behavior to plutonium. Lastly, plutonium was used to verify homolog studies and fulfill the objective by demonstrating a two phase inert matrix fuel of cubic zirconia solid solution and pure magnesia.

The second objective, determining the materials dissolution behavior under environmental conditions is addressed in Chapter 4. There are two experiments that were designed to deal with this problem. One was a corrosion study performed with a Soxhlet apparatus in which the sample was constantly contacted with, but never submerged in, hot water. Corrosion was monitored by mass loss and samples were examined before and after the experiment by microscopy methods. The other experiment designed to address this problem was to submerge samples of the material in environmental type solutions of deionized water, silicate-bicarbonate solution and brine for extended periods of time. Samples were taken from the solutions and analyzed for dissolved material by inductively coupled plasma – atomic emission spectroscopy. Experiments were conducted with either cerium, uranium or plutonium oxide as the fissile component and compared.

Samples were also assessed for their dissolution behavior under reactor condition in this chapter in order to verify results from previous studies (53) and extend them to material that contains a fissile component.

The third objective of discovering a means to dissolve the ceramic in an effort to reprocess the material is discussed in Chapter 5. This objective was assessed by submerging samples in acid contained in a round bottom flask with condenser so that samples could be heated to the boiling point of the acid. Acids used for these experiments included nitric, sulfuric and a solution of nitric and hydrofluoric acid with peroxide. Various concentrations and temperatures were used in this investigation. Samples containing cerium, uranium and plutonium oxide as the fissile component were used and compared to assess the accuracy of uranium and cerium as a plutonium homolog.

The fourth objective was to determine the irradiation behavior of the zirconia-magnesia inert matrix fuel and is reported in Chapter 6. This is important for two reasons. First, the irradiation behavior alone is important to material performance. Secondly, if the material does not undergo significant change due to irradiation its dissolution behavior is likely to remain similar to the unirradiated sample. The radiation tolerance of the material was determined by bombarding it with heavy ions via an accelerator. Dose was calculated so that the irradiation could be compared to previous studies and material changes were determined by grazing incident X-ray diffraction.

These objectives were identified as gaps in the knowledge of zirconia-magnesia inert matrix fuel. Addressed in this thesis is the synthesis and characterization of zirconia-magnesia inert matrix containing a fissile component and erbium oxide as a burnable

poison. The dissolution behavior of the material in aqueous media including reactor and environmental conditions is determined to assess its feasibility as a fuel and waste form. Possible means of dissolving the material so that it can be reprocessed have been identified. The materials radiation tolerance has been established and compared to related structures. This synthesis, characterization and dissolution behavior determination is to assess the feasibility of zirconia-magnesia as an inert matrix fuel and waste form.

CHAPTER 2

INSTRUMENTATION AND METHODS

2.1 Synthesis

2.1.1 Precipitation

Nitrate salt solutions of Pu, U, Zr, Mg, Ce, and Er were mixed with a stir rod in a 1L plastic beaker in the fume hood, on a tray as secondary containment. All chemicals are reagent grade and obtained from Alpha Aesar with the exception of uranium and plutonium. Uranium was obtained from J.T. Baker Laboratories and plutonium was obtained from Isotope Production Laboratories. The metal ions were precipitated as oxy-hydroxide by adding excess ammonium oxalate in concentrated ammonium hydroxide. This precipitate was then filtered in a designated Buchner funnel and transferred to a beaker. The liquid filtrate was monitored by scintillation counting and disposed. The precipitate contained in the beaker was placed in a secondary container and transferred to a dry-furnace. The dried precipitate was then removed from the dry-furnace and placed in a designated sample preparation box (alpha-box without gloves), which allows one to retain dexterity, while working in a slight negative pressure with little air flow. In the sample preparation box, the precipitate and a few drops of water were transferred into a grinding jar designated for radiological work. The grinding jar was placed in the secondary container to be transported to the ball mill and the sample preparation box was monitored for potential contamination. The grinding jar and the ball mill were surveyed before and after the milling.

## 2.1.2 Solid synthesis

All chemicals are reagent grade and obtained from Alpha Aesar with the exception of uranium and plutonium. Uranium was obtained from J.T. Baker Laboratories and plutonium was obtained from Isotope Production Laboratories. Solid oxides of zirconium, magnesium, erbium and cerium or uranium were fired at $900^{o}$C. After cooling they were weighed and placed in the sample preparation box where they were transferred to a grinding jar designated for radiological materials. The grinding jar was placed in the secondary container, transported to the ball mill and the sample preparation box was monitored for potential contamination. The grinding jar and ball mill were surveyed before and after the milling.

## 2.1.3 Calcination

The grinding jar was placed in the secondary container to be returned to the sample preparation box where the ground material was transferred to a large crucible. The crucible was covered by a lid and placed in a secondary container that was transferred to the muffle furnace. A label was posted for information on radionuclide and activity. The sample preparation box was monitored for contamination after transferring material from grinding jar to crucible and furnace. The material was calcined in a muffle furnace at $700^{o}$C for four to twelve hours. The crucible was removed from the furnace, covered, placed in a secondary container and taken to the sample preparation box.

## 2.1.4 Pellet pressing

In the sample preparation box the material was transferred to a press die designated for radiological work. The die was doubly contained and transferred to the hydraulic press. The press was surveyed before and after pressing. The die was then transferred to

the sample preparation box and the pellet removed.  The pellet and remaining sample material was placed in properly labeled containers and stored.  The sample preparation box was surveyed for potential contamination.

## 2.1.5 Sintering/annealing

The pellets were placed in a sintering boat, the sintering boat covered with alumina foil, and transported from the sample preparation box to the high-temperature furnace using a tray as a secondary containment. The sintering boat was placed on a ceramic plate and inserted in the working tube of the high temperature furnace.  The furnace was sealed via two 40 mm water-cooled KF flanges with Viton™ O-rings.  The furnace atmosphere was controlled and purged by $CO_2$, Ar, Ar/5%$H_2$, $N_2$, or $N_2$/8%$H_2$ gas, and the off-gasses were directed into a fume hood.  The maximum achievable furnace temperature is 1750°C, however temperatures of >1700°C are not necessary during dry-chemical processing of oxide fuels. Annealing times of 8 to 24 hours were required with a ramp up and down of 5 K/min.  A label was placed close to the furnace to inform about radionuclide and activity inserted into the furnace.  The furnace temperature was programmed to decrease to 200°C and the boat with the sintered pellets was then removed from the working tube and temporarily placed on a ceramic plate. The sinter boat with pellets was covered with aluminum foil and transferred to the sample preparation box via a tray. The high-temperature furnace was surveyed before and after its use.

## 2.2 Thermal gravimetric analysis/differential scanning calorimetry

Samples of 5 – 15 mg of precipitate were removed from the drying oven before they were completely dry. These samples were placed in an alumina crucible and transferred via double containment to the TGA/DSC instrument. Samples were analyzed by a Netzsch STA 449 C Jupiter TGA/DSC under Ar atmosphere and heated from $20^{o}$C to $1000^{o}$C. Thermal gravimetric analysis was used to quantify mass loss over a range of temperature. Differential scanning calorimetry was used to determine the temperature at which reactions take place by monitoring energy absorbed or evolved from the sample over a temperature range.

## 2.3 X-ray fluorescence

The preparation of standards for x-ray fluorescence was performed by mixing the oxide powders of zirconium, magnesium, uranium and erbium after they had been ashed at $1000^{o}$C and massed. This mixture was mechanically mixed for 1 hour in a Retsch PM100 ball mill at 500 rpm then pressed at 500 to 600 MPa with a SPEX Carver hydraulic press in a SPEX 13mm die to produce pellets. These pellets were then sintered as previously described.

Standards and samples were then ground to a powder via mortar and pestle and diluted 1:1 by mass with ground quartz. This mixture was ball milled for one hour as previously described to achieve a homogeneous mixture. One gram of this mixture was mechanically stirred into 6 grams lithium tetraborate and poured into a carbon crucible. The sample was then placed in a Barnstead/Thermolyne F48000 muffle furnace at $1050^{o}$C for 30 minutes, stirring every five minutes to create a glass disc that can be used

for x-ray fluorescence.  X-ray fluorescence was done using a PANalytical Axios instrument.  This was used to quantify the amount of each element within the bulk sample by the intensity of the characteristic x-rays emitted from the sample.

## 2.4 X-ray diffraction

Sintered pellets were ground to a powder and 10 mg were mixed with 2-4 mg of $LaB_6$ standard (NIST SRM 660a) as an internal line standard. The internal standard allows for correcting the sample displacement and goniometer off-set.  This mixture was spread in a thin layer over a low-background sample holder (single crystal silicon wafer) with the aid of methanol.  The analysis was performed on a PANalytical X'pert Pro diffractometer, which uses a Cu anode with Ni filter (wavelength $K\alpha_1$ at 0.1540598 nm and $K\alpha_2$ at 0.1544426 nm) and a fast multiple-Si-strip solid state detector (X'Celerator).  Patterns were taken using 40 mV and 40 mA from 10 to 120 $^o2\theta$ with a step size of 0.0083556 $^o2\theta$ and 50.165 seconds per step.  Phases were identified using PANalytical X'pert High Score Plus.  Bruker-AXS TOPAS2 was then used to perform the least-square lattice parameter refinement and Rietveld analysis.  Structure input parameters were taken from Inorganic Crystal Structure Database (ICSD).  Instrument parameter inputs were as follows: primary radius (mm) 240, secondary radius (mm) 240, receiving slit width (mm) 0.1, divergence angle (°) 1, filament length (mm) 10, sample length (mm) 20, receiving slit length (mm) 30, primary sollers (°) 2.3, and secondary sollers (°) 2.3.

Plutonium samples were analyzed by grinding the sample to a powder and spreading it in a thin layer over a low-background sample holder (single crystal silicon wafer) with the aid of methanol.  XRD patterns were collected on a Bruker D8 Advance

diffractometer, which uses a Cu anode with monochrometer (wavelength $K\alpha_1$ at 0.1540598 nm). Patterns were taken using 40 mV and 40 mA from 10 to 120 $^o2\theta$ with a step size of 0.01 $^o2\theta$ and 4 seconds per step. Phases were identified using Bruker-AXS EVA. Bruker-AXS TOPAS3 was then used to fit the diffracted intensities and to perform least-square and Rietveld analysis. Structure input parameters were taken from Inorganic Crystal Structure Database. Instrument parameter inputs were as follows: primary radius (mm) 435, secondary radius (mm) 435, receiving slit width (mm) 0.1, divergence angle (°) 1, filament length (mm) 12, sample length (mm) 8, receiving slit length (mm) 12, primary sollers (°) 2.3 and Lorenz polarization factor was set to 26.6.

## 2.5 Optical Microscopy

Pellets were vacuum mounted with Struers Epofix resin. Sample mounts were then ground and polished to a mirrored finish (1 micron) using a Struers TegraPol-15. Pellets were imaged using a Leica DM inverted reflectance microscope equipped with a digital Leica DFC 480 camera or a Leica 2500P microscope with a DFC 295 camera. Images were analyzed using Leica Application Suite 3.3.0. These microscopes are capable of 10x to 1000x magnification.

## 2.6 Secondary electron microscopy and electron probe microanalysis

A Joel 5600 secondary electron microscope equipped with energy dispersive spectroscopy was used to evaluate microstructure evolution and to determine stoiciometry of phases for plutonium containing samples. It was run at 20 keV at a working distance of 20 mm and a spot size of 30. Spot size is a Joel unit proportional to

current. Samples were either set in resin or fixed to carbon tape and carbon coated. They were then imaged and semi-quantitative analysis was used to determine the concentrations of each element within each phase. With well characterized standards this method has proven to be accurate within 1 wt. %. For unknown samples such as the ones used in this study it is estimated to be accurate to 5 wt. %. Mounted pellets were carbon coated and analyzed with a Joel JXA 8900R electron probe microanalyzer. Elemental mapping was done up to 9 mm$^2$ at 15 keV and 100 nanoamps. Quantitative measurements were performed at 15 keV and 30 nanoamps.

### 2.7 X-ray absorption fine structure / X-ray absorption near edge spectroscopy

Samples were prepared by 1:10 dilution of sample to boron nitride by mass, so that total uranium concentration was 0.5% (wt/wt). Uranium $L_{III}$ edge (17,166 eV) and zirconium K edge (17,663 eV) x-ray absorption spectra were collected at the Advanced Photon Source at Argonne National Lab (BESSERC-CAT Beamline 12) using a Si (1, 1, 1) double crystal monochromator. Spectra were recorded in transmission geometry using Ar filled ionization chamber and in fluorescence using a 13 element detector. Energy calibration was done using an yttrium foil (K edge = 17,998 eV).

For each sample, several EXAFS spectra were recorded up to 13 Å$^{-1}$ and averaged. The background contribution was removed using Autobk software and data analysis was performed using WINXAS. For the fitting procedure, amplitude and phase shift functions were calculated by FEFF8.2. The feff.inp files were generated by ATOMS using crystallographic structures taken from literature in the Inorganic Crystal Structure Database (ICSD). The adjustments of EXAFS spectra were performed under the

constraints $S_o^2 = 0.9$, a single value of energy shift $\Delta E_o$ was used for all scattering, and coordination number was fixed at the values given by literature.

## 2.8 Pressure vessel dissolution

To mimic fuel behavior under reactor conditions, a pressure vessel was assembled to determine solubility and corrosion of the ceramic fuel pellets at temperatures exceeding $300^o$C and at pressures over 10.3 MPa (1500 psi). The setup allows *in-situ* sampling throughout the experiment and samples were analyzed by ICP-AES. The sample and deionized water were placed inside the pressure vessel and the integrity of the vessel was confirmed by high pressure argon gas. The temperature was set and stirrer initiated. Once at temperature samples were obtained by opening a valve allowing the pressurized water to fill a side arm attached to the vessel. The valve was closed sealing the pressure vessel. A second valve further down the line was then opened to evacuate the side arm and obtain the sample.

## 2.9 Acid dissolution

Acid dissolution studies were carried out to determine solubility of the matrix in various media. Samples were either pelletized where surface area was determined by geometric methods or ground to a coarse powder and surface area determined by gas sorption techniques. Samples were placed in 250 mL round bottom flasks that were equipped with a condenser and positioned in a heating mantle. The acid (nitric acid or sulfuric acid) was added to the round bottom flask in an amount of either 150 mL or 200 mL. Samples were taken by pipette and diluted to 1 % acid by volume to facilitate

29

analysis by ICP-AES.  Samples that were exposed to hydrofluoric acid were handled in the same way but in a Teflon vessel without heating.

### 2.10 Pulse flow environmental dissolution

Teflon vessels with air tight screw lids were filled with 50 mL of solution to be used for environmental dissolution studies.  A 5 mm diameter pellet was then placed in the solution.   Three different compositions were used.   They are as follows: $Zr_{0.625}Mg_{0.3}U_{0.05}Er_{0.025}O_{1.7}$, $Zr_{0.475}Mg_{0.45}U_{0.05}Er_{0.025}O_{1.5}$, and  $Zr_{0.325}Mg_{0.6}U_{0.05}Er_{0.025}O_{1.4}$. Three different solutions were used for the dissolutions.  They are as follows: deionized water, silicate water made by dissolving 0.179 g $NaHCO_3$ and 0.058 g $SiO_2$ as silicic acid in 1 L of water and adjusting the pH to 7.5, and brine prepared by dissolving 48.2 g KCl, 90 g NaCl, and 116 g $MgCl_2$ in 1 L of water and adjusting the pH to 6.5.  The lid was screwed on tightly and total mass of container, water and sample was determined and labeled to assess loss of solution.  Samples were then placed in an oven capable of maintaining $90^{o}C$.  The lid was retightened at one hour and every 24 hours to ensure a good seal for the first three days.  The bulk of the samples were collected every two weeks.  However, a duplicate sample was obtained at one week and another at three weeks to assess any differences due to sampling time.  Samples were taken by removing the vessel from the oven and letting it cool for one hour.  Then a 5 mL aliquot was removed from the vessel.  The vessel was then brought back to original volume with appropriate solution by mass of total solution, sample, and vessel to account for losses due to evaporation.  Each combination of sample and solution was run in triplicate with a

single blank of solution without sample.  Elemental concentrations were analyzed by ICP-AES.

## 2.11 Soxhlet corrosion study

To determine the corrosion resistance of the ceramics, samples were placed via a cellulose thimble in a Soxhlet apparatus, and the pellets were continuously contacted with distilled hot water (65-70$^\circ$C).  To evaluation this type of experiments, the specific mass loss was determined over an extended time period, typically 2,000 hrs. The specific mass loss was characterized by a first order reaction and allows the extrapolation of long-term behavior.

## 2.12 Inductively coupled plasma – atomic emission spectroscopy

Samples from dissolution studies were analyzed by inductively coupled plasma – atomic emission spectroscopy (ICP-AES) on a Thermo iCAP 6000 with iTEVA software. The instrument was run at 1150 watts and the following lines were used to analyze the elements of interest: Er at 337.271 nm, Mg at 202.582 nm, U at 367.007 nm, and Zr at 343.823 nm.  A seven point calibration was used, samples were measured in triplicate, and a calibration check was performed every 50 samples.

## 2.13 Scintillation counting

A Perkin Elmer model 3100TR liquid scintillation counter was used to determine plutonium dissolution from the zirconia – magnesia matrix.  Background was subtracted manually by counting a blank sample.  Counting time was determined by setting the 2

sigma terminator at 2 %. Counts greater than three times background were considered significant. Samples in concentrated acids were diluted to eliminate quenching concerns.

## 2.14 Transmission electron microscopy

A TECNAI-G2-F30 Supertwin transmission electron microscope with a 300 keV field emission gun was used to study the material at high magnification. Bright-field mode (TEM-BF) was used to study the morphology of samples, while high resolution mode (HRTEM) in combination with selected area diffraction (SAD) was used to characterize microstructure. TEM images were recorded using a slowscan CCD camera attached on a Gatan GIF 2000 (Gatan Image Filter). Elemental composition and distribution were investigated by STEM and the corresponding XEDS.

## 2.15 Irradiation studies

Ion irradiations were performed at cryogenic temperature (~100 K) in the Ion-Beam Materials Laboratory at Los Alamos National Laboratory, using a Varian ion implanter operating at 150 kV. About 300 keV $Kr^{++}$ ions were implanted at normal incidence using a dose rate of 1 x $10^{16}$ $Kr/m^2$ s to fluencies ranging from 0.5 to 2 x $10^{20}$ $Kr/m^2$. Irradiated samples were analyzed using both grazing incidence X-ray diffraction (GIXRD) and transmission electron microscopy (TEM). GIXRD measurements were performed using a Bruker AXS D8 Advanced X-ray diffractometer at a gracing incidence angle of a = $0.25^o$. Irradiated samples were prepared in cross-sectional geometry for TEM examination using a focused-ion-beam (FIB) apparatus. TEM investigations were performed using a Philips CM-30 instrument operating at 300 kV.

CHAPTER 3


SYNTHESIS AND CHARACTERIZATION

3.1 Synthesis with cerium as a plutonium homolog

Zironia-magnesia inert matrix ceramic containing cerium oxide as a plutonium oxide homolog and erbium oxide as a burnable poison was synthesized using the precipitation method described in Section 2.1. Cerium oxide is believed to be a suitable structural homolog for plutonium oxide because it can occupy the tetravalent oxidation state in which plutonium is expected to be in under these conditions and it is a similar size (38). The atomic radii of cerium is 185 pm while plutonium is 175 pm. Cerium is however expected to be a poor chemical homolog for plutonium due to the limited number of oxidation states accessible to cerium when compared to plutonium. Because of this, future studies were performed with uranium as a plutonium chemical homolog and final studies were conducted with plutonium.

To monitor the calcination process and establish suitable temperatures and times for sintering, a sample was analyzed by thermal gravimetric analysis and differential scanning calorimetry (TGA/DSC) according to the procedure described in Section 2.2. The TGA/DSC analysis shows that the oxy-hydroxide precipitate is converted to the oxide at $262^{o}C$ by an exothermic reaction and solid solution formation begins with a phase transition at $510^{o}C$ as evident by an exothermic reaction corresponding to constant mass [Figure 6]. This was confirmed to be the monoclinic to tetragonal phase transition of zirconium oxide by X-ray diffraction. The calcinations process at $700^{o}C$ for eight hours promotes complete solid solution formation which is also confirmed by X-ray

diffraction (56). This isomorphic substitution is diffusion controlled. This shows solid solution formation at less severe temperatures and durations than the corresponding dry synthesis route described in Section 2.1.2.
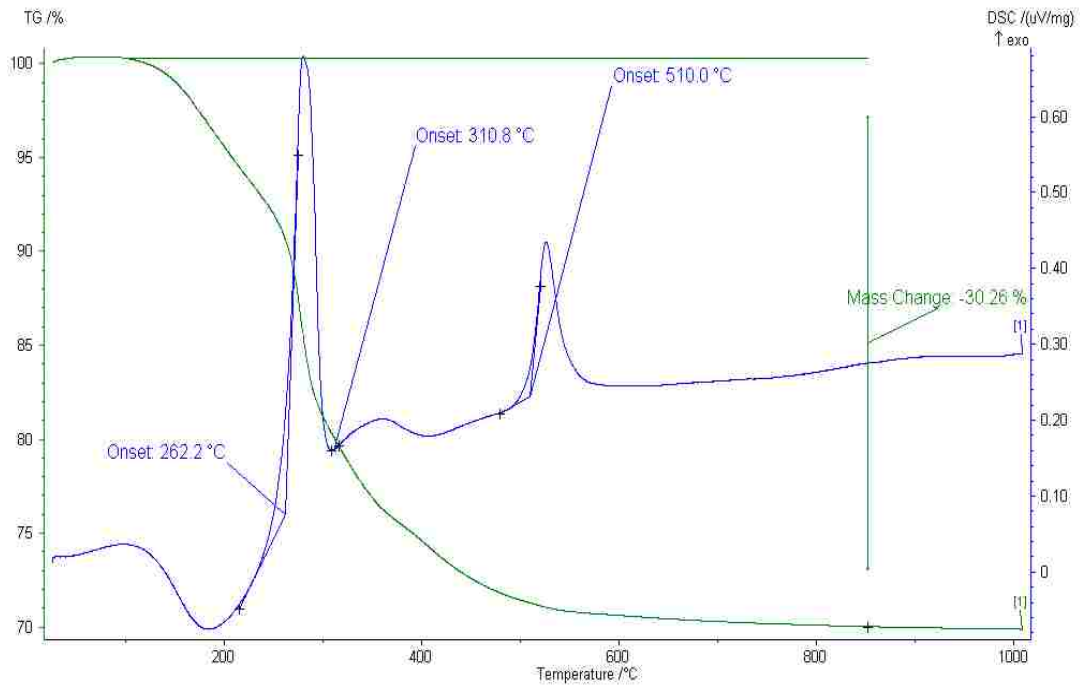


Figure 6: Thermal gravimetric analysis and differential scanning calorimetry of $Zr_{0.943}Ce_{0.035}Er_{0.022}O_{1.95}$
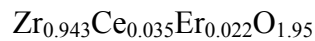
Cerium oxide, as $CeO_2$, content in the ceramics varied from 3.5-10.5% (wt/wt) as this is the likely range of fissile material to be incorporated into an inert matrix fuel (57). Neutronic calculations have shown an optimal volume ratio of burnable poison to be half of the fissile phase (57). Because of this, the erbium oxide ($ErO_{1.5}$) content was varied from 2.2-6.6% (wt/wt). The inert matrix was varied from only zirconium oxide to being completely magnesium oxide over ten compositions [Table 3].

Table 3: Oxide concentration synthesized with cerium as a plutonium homolog (wt. %)

| sample # | % $ZrO_2$ | % MgO | % $CeO_2$ | % $ErO_{1.5}$ |
|----------|-----------|-------|-----------|---------------|
| 1 | 94.3 | 0.0 | 3.5 | 2.2 |
| 2 | 90.7 | 3.2 | 3.8 | 2.3 |
| 3 | 86.5 | 6.9 | 4.1 | 2.5 |
| 4 | 81.4 | 11.3 | 4.4 | 2.8 |
| 5 | 75.4 | 16.7 | 4.9 | 3.1 |
| 6 | 67.9 | 23.2 | 5.5 | 3.4 |
| 7 | 58.6 | 31.4 | 6.2 | 3.9 |
| 8 | 46.5 | 42.0 | 7.1 | 4.4 |
| 9 | 30.3 | 56.3 | 8.3 | 5.2 |
| 10 | 0.0 | 82.9 | 10.5 | 6.6 |

3.2 Synthesis with uranium as a plutonium homolog

Zironia-magnesia inert matrix fuel containing uranium oxide as fissile component and plutonium oxide homolog and erbium oxide as a burnable poison was synthesized using the precipitation method described in Section 2.1. Uranium oxide content in the ceramics was held constant at 5% (wt/wt) as this is around the minimum of the likely range of fissile material to be incorporated into an inert matrix fuel for thermal reactor applications (57). Neutronic calculations have shown an optimal volume ratio of burnable poison to be half that of the fissile phase (57). Because of this, the erbium oxide content was held at 2.5% (wt/wt). The inert matrix was composed of zirconium oxide

and magnesium oxide and was varied from being exclusively zirconium oxide to being completely magnesium oxide over ten compositions listed in Table 4.

Table 4: Oxide concentration synthesized with uranium as a plutonium homolog (wt. %)

| Sample # | % $ZrO_2$ | % MgO | % $UO_2$ | % $ErO_{1.5}$ |
|---|---|---|---|---|
| 1 | 92.5 | 0 | 5 | 2.5 |
| 2 | 87.5 | 5 | 5 | 2.5 |
| 3 | 82.5 | 10 | 5 | 2.5 |
| 4 | 77.5 | 15 | 5 | 2.5 |
| 5 | 72.5 | 20 | 5 | 2.5 |
| 6 | 62.5 | 30 | 5 | 2.5 |
| 7 | 47.5 | 45 | 5 | 2.5 |
| 8 | 32.5 | 60 | 5 | 2.5 |
| 9 | 17.5 | 75 | 5 | 2.5 |
| 10 | 0 | 92.5 | 5 | 2.5 |

The synthesis of the uranium containing inert matrix fuel progressed as expected from previous studies using cerium as a plutonium homolog (Section 3.1). One notable difference was in the higher oxidation states accessible to uranium. The uranium precipitated as the oxy-hydroxide in the hexavalent oxidation state to form a bright yellow solid. As this is calcined and subsequently converted to oxide ($UO_3$) it develops a deeper orange color [Figure 7]. This compound is then sintered under Ar/$H_2$ to reduce the uranium to the tetravalent oxidation state, giving the ceramic pellet a brown to black

color after sintering (58). X-ray fluorescence spectroscopy was used to verify elemental concentrations within the synthesized ceramics as described in Section 2.3. All quantities were within expected values with standard deviations averaging 2-5 %. XRF has verified that coprecipitation can be used to reliably synthesize inert matrix ceramics at consistent concentrations.
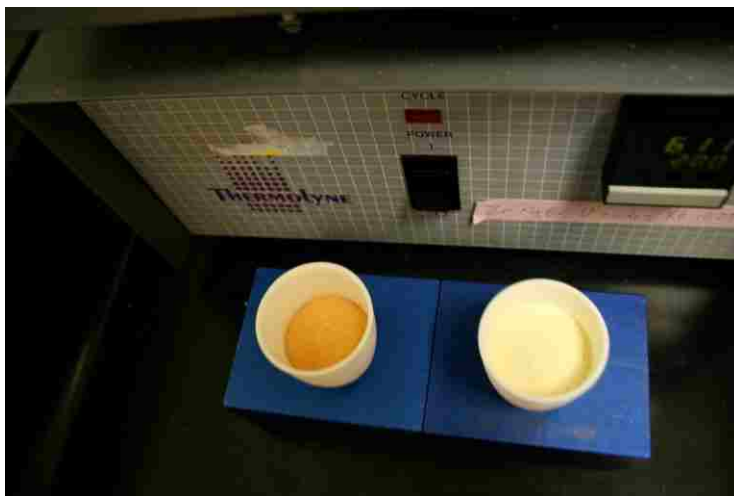


Figure 7: Precipitated oxy-hydroxide (right) and calcined oxide (left) precursors of uranium containing zirconia-magnesia inert matrix fuel

### 3.3 Synthesis with plutonium

Zironia-magnesia inert matrix fuel containing plutonium oxide as the fissile material and erbium oxide as a burnable poison was synthesized using the precipitation method described in Section 2.1. However, due to the high solubility of magnesium it was found that a large portion of this element remained in the filtrate. This became evident in this study because of mass and volume reduction in the synthesis from several grams to around 100 mg due to the high radiological activity of plutonium (59). The small

differences in solubility of the cations after precipitation manifests as fluctuations in the concentrations within the solid. Most notably the high solubility of magnesium results in a drop in magnesium oxide concentration in the solid. To avoid this loss the precipitate was not filtered but heated to dryness to synthesize the samples with high magnesium oxide concentrations. Since the nitrate and chloride counter ions are volatile it was possible to avoid any loss of material without the incorporation of impurities. In a larger scale production this should not be necessary as the differences in solubility are insignificant when compared to the amount of material that is produced. The resulting oxy-hydroxide precipitate was then dried, calcined, and pressed into pellets as previously described (Section 2.1). These pellets were then sintered at $1600^{o}$C in a Reetz LORA tube furnace for 10 hours under argon atmosphere, plutonium oxide remaining in the tetravalent valence state.

Plutonium oxide and erbium oxide content was varied to determine the solubility of plutonium and erbium within the zirconia phase. The inert matrix was composed of zirconium oxide and magnesium oxide and was varied to explore the composition range. The bulk concentrations used to synthesize the pellets in this study are listed in Table 5. One of the main goals of this study was to synthesize a two phase inert matrix fuel of periclase (a pure MgO phase) and cubic zirconia, which would incorporate the fissile material and burnable poison through isomorphic substitution. This was previously attempted by mixing the oxide powders and sintering, which resulted in the formation of a third phase consisting of plutonium oxide rich microspheres (55). A burnable poison was not used in the previous study. Because of this, a precipitation method was used for

38

this study. This allows for more complete mixing and has been shown to form solid solutions at less extreme temperatures and times during sintering (Section 3.1).

Table 5: Oxide concentration synthesized with plutonium (wt. %)

| Sample # | % $ZrO_2$ | % $MgO$ | % $PuO_2$ | % $ErO_{1.5}$ |
|----------|-----------|---------|-----------|---------------|
| 1 | 71 | 3.0 | 16 | 9.0 |
| 2 | 75 | 11 | 7.5 | 7.5 |
| 3 | 67 | 14 | 9.8 | 8.2 |
| 4 | 58 | 20 | 12 | 9.8 |
| 5 | 42 | 50 | 4.7 | 2.4 |
| 6 | 23 | 72 | 3.5 | 2.0 |
| 7 | 16 | 79 | 3.4 | 1.8 |

3.4 Characterization of cerium oxide containing inert matrix fuel

3.4.1 X-ray diffraction (XRD) of cerium oxide containing inert matrix fuel

An XRD pattern was taken of the sample $Zr_{0.943}Ce_{0.035}Er_{0.022}O_{1.95}$ after calcining at $700^oC$ for eight hours. Broad peaks show that the reaction has not gone to completion [Figure 8]. There is not a constant concentration throughout the sample. It does show that the reaction has started, because there is no evidence of the starting materials $Er_2O_3$ or $CeO_2$. The presence of tetragonal zirconium oxide is due to the Ce and Er isomorphically substituting onto the zirconium oxide lattice stabilizing the tetragonal $ZrO_2$, however there is not enough substitution to fully stabilize the cubic zirconia phase or the transition temperature to the cubic phase was not reached.
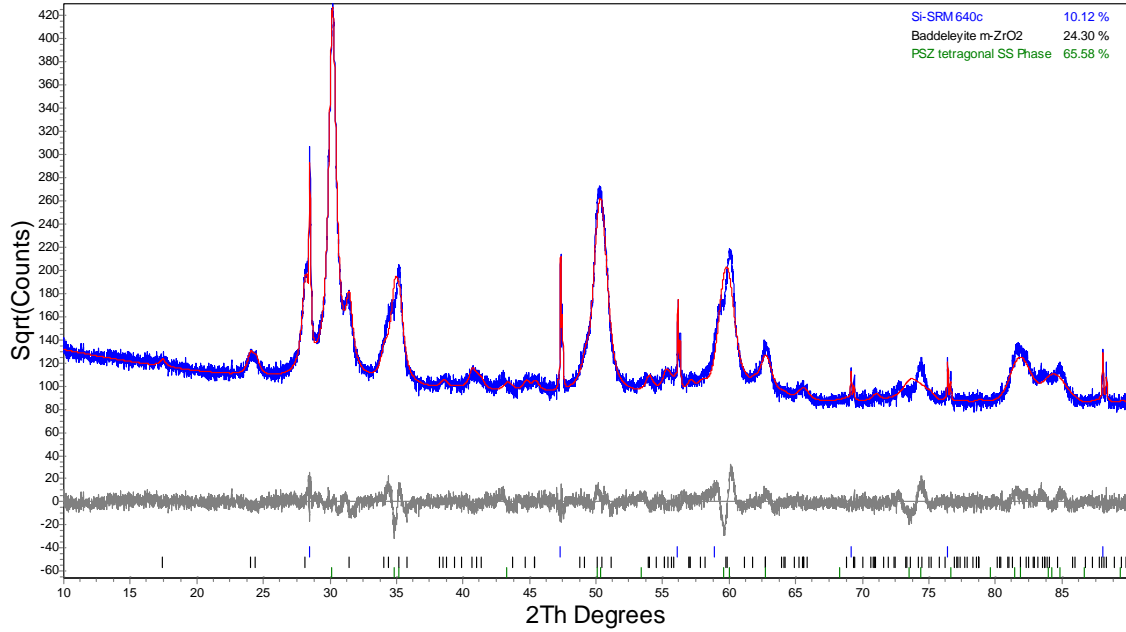
Figure 8: X-ray diffraction pattern of calcined $Zr_{0.960}Ce_{0.025}Er_{0.014}O_{1.99}$ (blue) with fit

(red) and difference curve (grey).

At low magnesium oxide concentrations (less than 7 wt. %) a single cubic zirconia phase is evident by XRD. This was observed in samples $Zr_{0.866}Mg_{0.093}Ce_{0.026}Er_{0.014}O_{1.90}$ and $Zr_{0.771}Mg_{0.188}Ce_{0.026}Er_{0.014}O_{1.80}$ [Figure 9]. This suggests that all of the magnesium, cerium, and erbium oxides are isomorphically substituted into the zirconia lattice. The magnesium oxide is required to stabilize the cubic zirconia as evident by the tetragonal zirconium oxide in the absence of magnesium oxide.

If the magnesium content is increased, the limit of isomorphic substitution of zirconium by magnesium is exceeded and the excess magnesium is precipitated as a cubic MgO phase (periclase). This is observed in samples with as little as 11.3 wt. % MgO [Figure 10]. This two phase mixture of cubic zirconia and periclase persists for all samples with magnesium oxide concentration of 11.3 to 42 wt. % MgO [Figure 11].
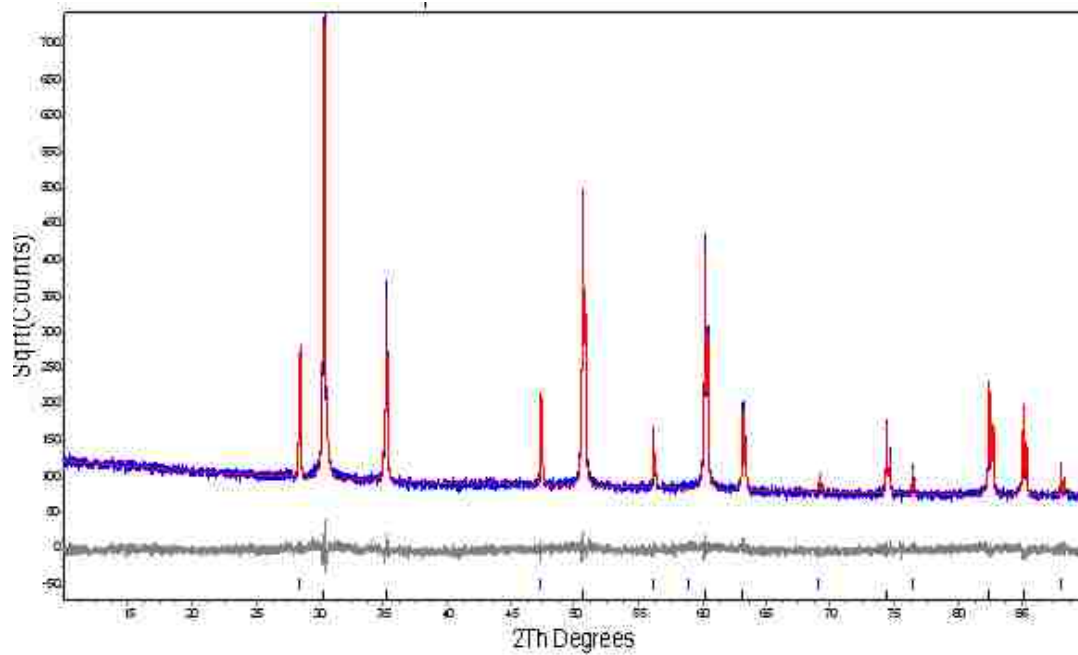
Figure 9: X-ray diffraction pattern of sintered $Zr_{0.866}Mg_{0.093}Ce_{0.026}Er_{0.014}O_{1.90}$ (blue) with

fit (red) and difference curve (grey).
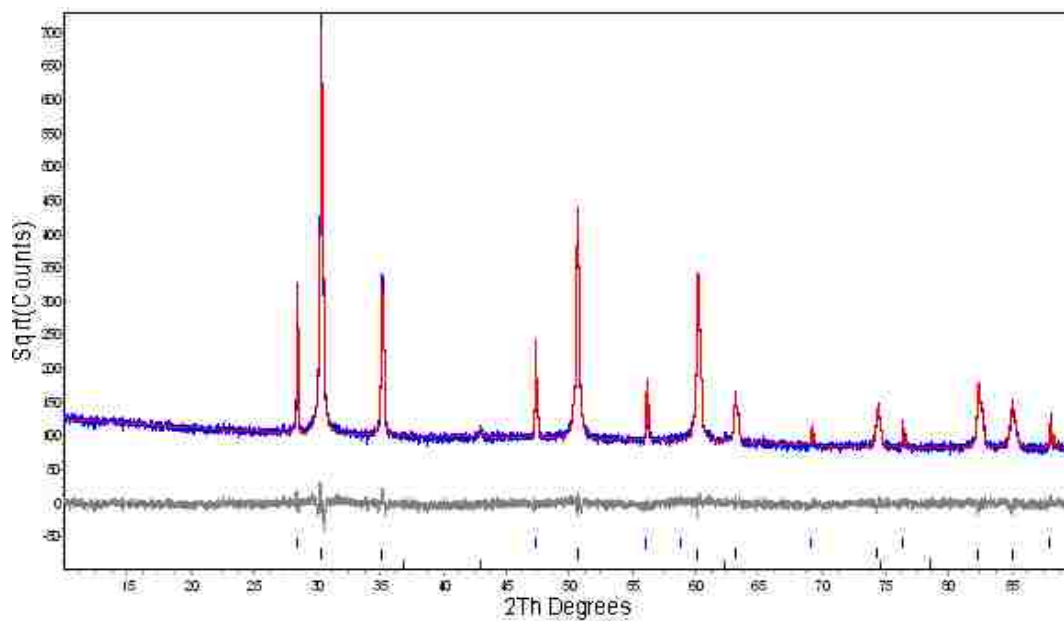


Figure 10: X-ray diffraction pattern of sintered $Zr_{0.673}Mg_{0.286}Ce_{0.026}Er_{0.015}O_{1.71}$ (blue) with

fit (red) and difference curve (grey).
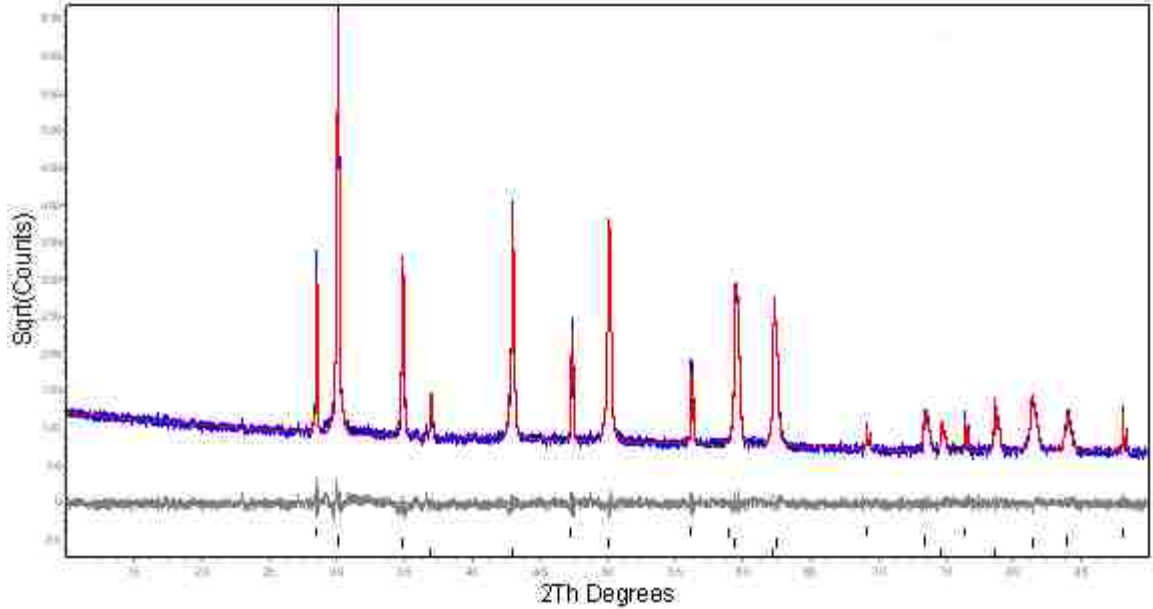
Figure 11: X-ray diffraction pattern of sintered $Zr_{0.254}Mg_{0.702}Ce_{0.028}Er_{0.016}O_{1.29}$ (blue) with fit (red) and difference curve (grey).

The periclase phase continues to build in until the $ZrO_2$ concentration is too low to accommodate the level of $CeO_2$ and $Er_2O_3$ that is in the sample; nominally around 30 % (wt/wt) of $ZrO_2$ at $CeO_2$ and $Er_2O_3$ levels of 8.3 % and 5.2 % (wt/wt) respectively. At sufficiently low levels of $ZrO_2$, $CeO_2$ together with $Er_2O_3$ form a cubic solid solution resulting in a third phase observed in sample $Zr_{0.143}Mg_{0.813}Ce_{0.028}Er_{0.016}O_{1.18}$ [Figure 12]. This $CeO_2$ and $Er_2O_3$ phase is also present when there is no $ZrO_2$ ($Mg_{0.956}Ce_{0.028}Er_{0.016}O_{1.04}$) [Figure 13].

A list of the phases present, space groups, and quantity of phases present for each sample is in Table 6. The lattice parameter for the MgO phase is unchanged by the composition, which suggests that the larger cations are not being incorporated into the periclase crystal structure. In contrast the more $CeO_2$ and $Er_2O_3$ in the sample the larger

42

the unit cell of the cubic zirconia, indicating the progress in solid solution formation and the associated incorporation of $Ce^{4+}$ and $Er^{3+}$ cations into the zirconia lattice.
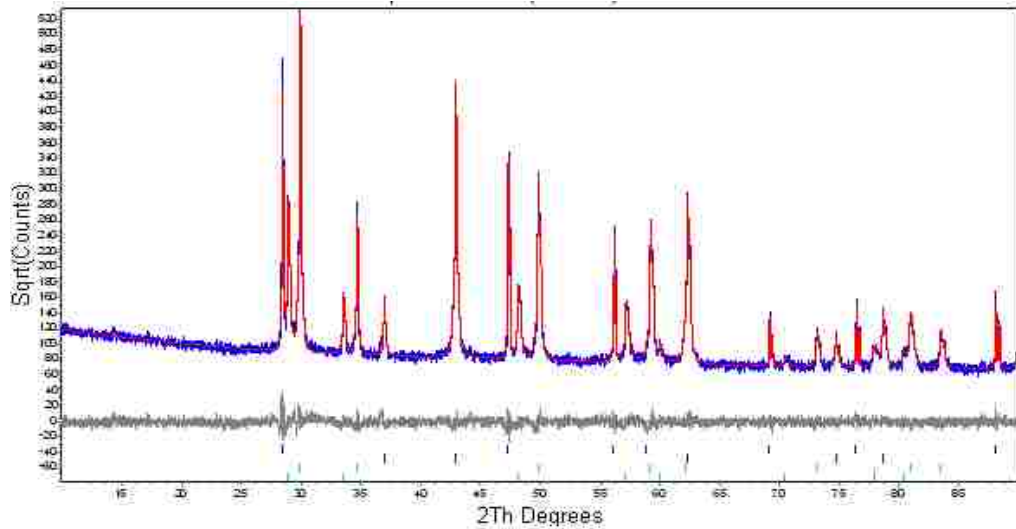


Figure 12: X-ray diffraction pattern of sintered $Zr_{0.143}Mg_{0.813}Ce_{0.028}Er_{0.016}O_{1.18}$ (blue) with fit (red) and difference curve (grey).
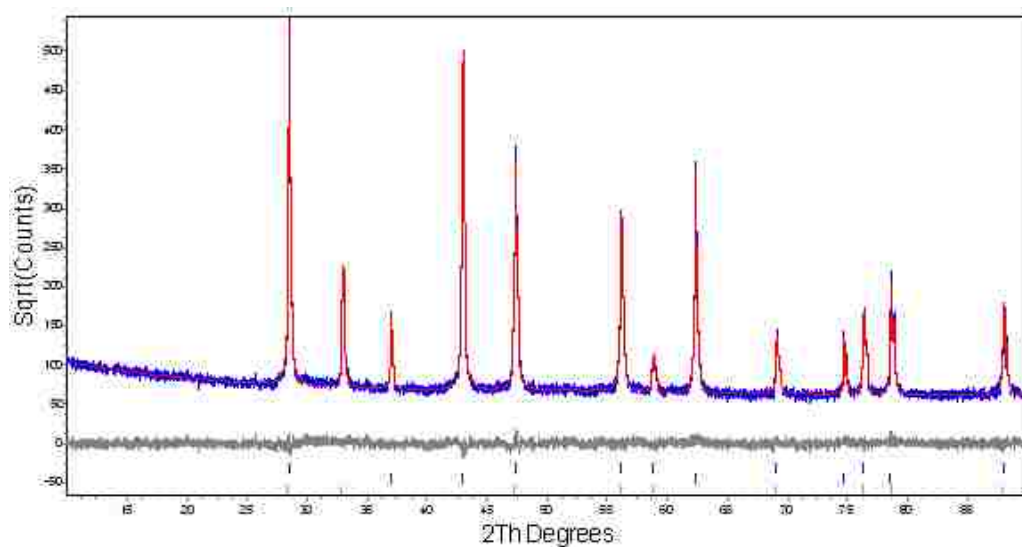


Figure 13: X-ray diffraction pattern of sintered $Mg_{0.956}Ce_{0.028}Er_{0.016}O_{1.04}$ (blue) with fit (red) and difference curve (grey).

Table 6: Phases present and lattice parameters for cerium containing samples as determined by x-ray diffraction

| Sample # | Bulk Sample Composition (Calculated) | Phases Present (space group) | Lattice Parameters (nm) | Stoichiometry of Phase as Determined by EPMA | Quantity (wt. %) |
|---|---|---|---|---|---|
| 1 | $Zr_{0.960}Ce_{0.025}Er_{0.014}O_{1.99}$ | $ZrO_2$ (P12$_1$/c1) | 0.51585(2) 0.52123(7) 0.53341(8) | Not Determined | 27.0 |
| | | $ZrO_2$ (P42/nmcS) | 0.36397(10) 0.50966(7) | Not Determined | 73.0 |
| 2 | $Zr_{0.866}Mg_{0.093}Ce_{0.026}Er_{0.014}O_{1.90}$ | $ZrO_2$ (Fm-3m) | 0.50964(5) | $Zr_{0.892}Mg_{0.075}Ce_{0.019}Er_{0.014}O_{1.92}$ | 100.0 |
| 3 | $Zr_{0.771}Mg_{0.188}Ce_{0.026}Er_{0.014}O_{1.80}$ | $ZrO_2$ (Fm-3m) | 0.50978(3) | $Zr_{0.814}Mg_{0.141}Ce_{0.029}Er_{0.014}O_{1.85}$ | 100.0 |
| 4 | $Zr_{0.673}Mg_{0.286}Ce_{0.026}Er_{0.015}O_{1.71}$ | $ZrO_2$ (Fm-3m) | 0.50988(5) | $Zr_{0.834}Mg_{0.112}Ce_{0.036}Er_{0.017}O_{1.88}$ | 98.3 |
| | | MgO (Fm-3m) | 0.42135(4) | MgO | 1.7 |
| 5 | $Zr_{0.571}Mg_{0.387}Ce_{0.027}Er_{0.015}O_{1.61}$ | $ZrO_2$ (Fm-3m) | 0.51113(8) | $Zr_{0.792}Mg_{0.143}Ce_{0.044}Er_{0.021}O_{1.85}$ | 83.7 |
| | | MgO (Fm-3m) | 0.42139(3) | MgO | 16.3 |
| 6 | $Zr_{0.468}Mg_{0.489}Ce_{0.027}Er_{0.015}O_{1.50}$ | $ZrO_2$ (Fm-3m) | 0.51156(5) | $Zr_{0.774}Mg_{0.152}Ce_{0.049}Er_{0.025}O_{1.84}$ | 62.6 |
| | | MgO (Fm-3m) | 0.42129(9) | MgO | 37.4 |
| 7 | $Zr_{0.363}Mg_{0.594}Ce_{0.027}Er_{0.016}O_{1.40}$ | $ZrO_2$ (Fm-3m) | 0.51202(9) | Not Determined | 55.8 |
| | | MgO (Fm-3m) | 0.42126(4) | Not Determined | 44.2 |
| 8 | $Zr_{0.254}Mg_{0.702}Ce_{0.028}Er_{0.016}O_{1.29}$ | $ZrO_2$ (Fm-3m) | 0.51516(9) | $Zr_{0.722}Mg_{0.139}Ce_{0.094}Er_{0.045}O_{1.84}$ | 43.4 |
| | | MgO (Fm-3m) | 0.42125(10) | MgO | 56.6 |
| 9 | $Zr_{0.143}Mg_{0.813}Ce_{0.028}Er_{0.016}O_{1.18}$ | $ZrO_2$ (Fm-3m) | 0.51747(10) | $Zr_{0.682}Mg_{0.118}Ce_{0.114}Er_{0.086}O_{1.84}$ | 20.5 |
| | | MgO (Fm-3m) | 0.42125(8) | MgO | 72.6 |
| | | $Ce_xEr_yO_{2x+1.5y}$ (Fm-3m) | 0.53419(9) | Not Determined | 6.9 |
| 10 | $Mg_{0.956}Ce_{0.028}Er_{0.016}O_{1.04}$ | MgO (Fm-3m) | 0.42119(8) | MgO | 87.7 |
| | | $Ce_xEr_yO_{2x+1.5y}$ (Fm-3m) | 0.54342(6) | Not Determined | 12.3 |

### 3.4.2 Optical microscopy of cerium oxide containing ceramics

Optical microscopy shows zirconia as a light grey phase and periclase as a dark gray phase in reflectance permitting the identification of small quantities of MgO which may be concentrated in the grain boundaries in samples containing as little as 3 % (wt/wt) MgO [Figure 14]. A MgO phase was not identified by XRD in this sample containing 3 wt. % MgO, as its concentration is either below the detection limit of XRD (typically 0.1 wt.-%) or X-ray amorphous. It is believed that a small amount of MgO is incorporated into grain boundaries and goes undetected by x-ray diffraction. By optical microscopy it was possible to illustrate the intimate mixing of the periclase and zirconia phases [Figure 15].
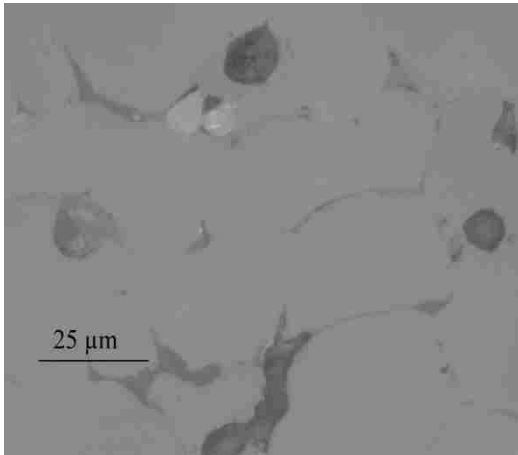


Figure 14: Optical microscope image of $Zr_{0.907}Mg_{0.032}Ce_{0.038}Er_{0.023}O_{1.96}$ x1000 magnification. Zirconia-based fuel phase (light grey), MgO phase (dark grey), and pore space (darkest grey).
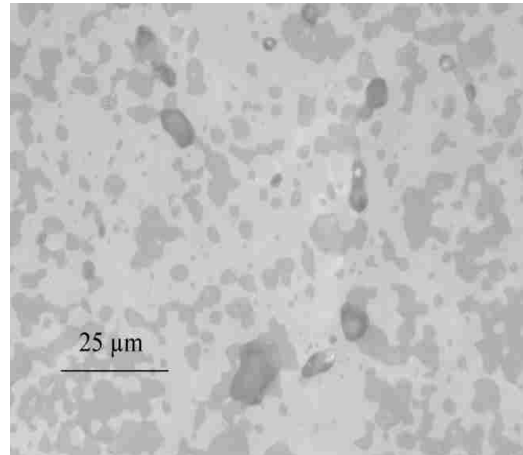
Figure 15: Optical microscope image of $Zr_{0.679}Mg_{0.232}Ce_{0.055}Er_{0.034}O_{1.75}$ x1000 magnification. Zirconia-based fuel phase (light grey), MgO phase (dark grey) and pore space (darkest grey).

3.4.3 Electron probe microanalysis of cerium oxide containing ceramics

Electron probe microanalysis was used to scan a 4 mm$^2$ area and to map the relative concentrations of the elements within the sample. The elemental zirconium, cerium, and erbium maps are identical indicating that cerium and erbium are evenly distributed within the zirconia phase. The magnesium map shows a faint outline of the zirconium map suggesting that a small amount of Mg is contained within the zirconia phase. However, in samples containing a secondary MgO phase there are also high concentrations of magnesium in areas that have, besides oxygen, no other elements present [Figure 16]. This shows that the MgO phase is relatively pure, which is also consistent with the results of the MgO lattice parameter refinement from the XRD powder data (Section 3.4.1).
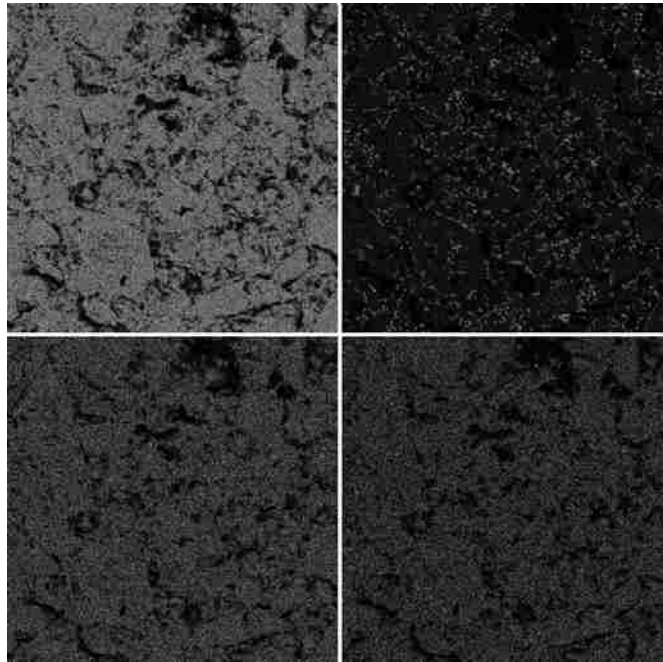


Figure 16: Elemental maps by electron probe microanalysis over 4 mm$^2$ of Zr Lα (top left) Mg Kα (top right) Ce Lα (bottom left) and Er Lα (bottom right) from sample $Zr_{0.468}Mg_{0.489}Ce_{0.027}Er_{0.015}O_{1.50}$

Microprobe analysis was also used to quantify the amount of each element present in small volumes. In this way the stoichiometry of each phase within a sample was examined [Table 6]. In the zirconia phase, there is an increase in MgO content as MgO in the sample is increased from 0 % to 11 % (wt/wt) in the total sample. At this point the cubic zirconia is saturated with respect to MgO. The zirconia phase contains up to 5 % (wt/wt) MgO at saturation, and any increase in MgO in the sample has no affect on the MgO content of the $ZrO_2$ phase. It can be stated that the solubility limit of Mg for cubic stabilized zirconia is 5 % (wt/wt) under these conditions. The amount of cerium and erbium oxide continues to increase as more cerium and erbium oxide are added to the ceramic. The maximum amount of cerium and erbium oxides were 14 % and 12 % (wt/wt) respectively for sample $Zr_{0.143}Mg_{0.813}Ce_{0.028}Er_{0.016}O_{1.18}$, in which a cerium erbium oxide phase began to precipitate [Figure 17].
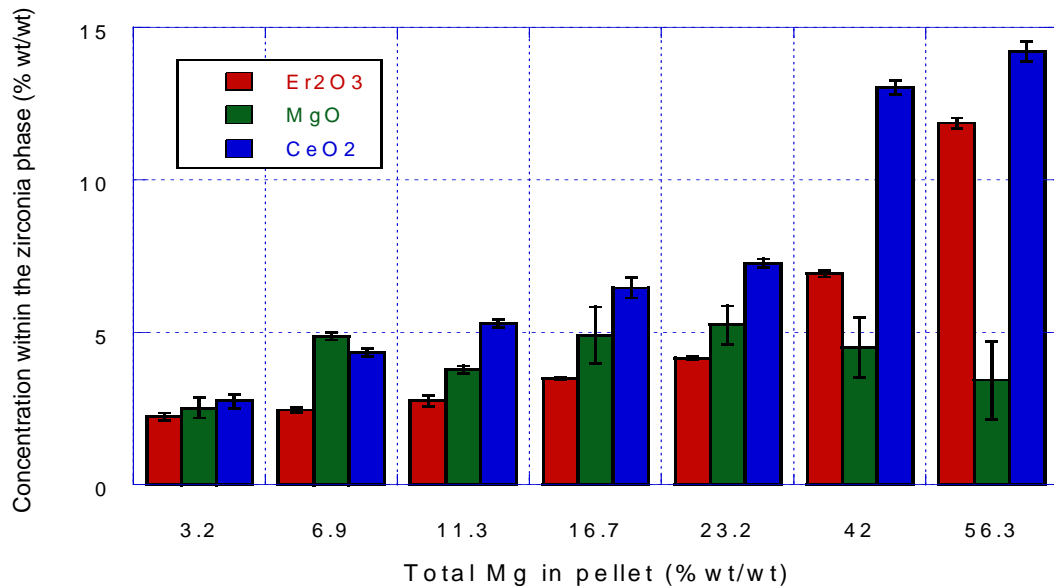


Figure 17: Stoichiometry of the zirconia phase by electronprobe microanalysis. (Error bars represent standard deviation in measurements)

It was difficult to probe the periclase phase in many samples due to the small area and intimate mixture of the phases. However, many measurements show less than 1 % (wt/wt) of any other species in the MgO phase, again supporting earlier data suggesting low affinity of cerium, erbium, and zirconium for isomorphic substitution or for occupying interstitials within this phase.

3.4.4 Transmission electron microscopy of cerium oxide containing ceramic

Transmission electron microscopy (TEM) was performed according to the procedure outlined in Section 2.14. By high resolution TEM it was possible to confirm lattice parameters that were previously determined by x-ray diffraction (Section 3.4.1).
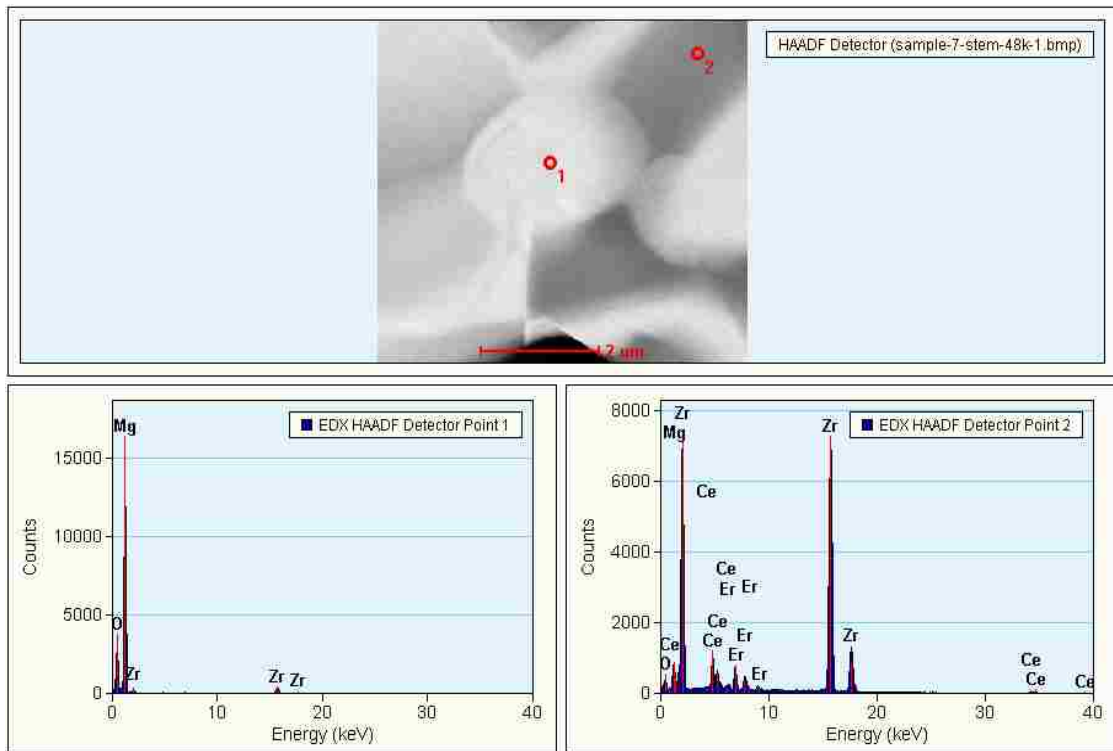


Figure 18: Transmission electron microscopy image with corresponding energy dispersive spectroscopy of a MgO grain (#1) and a zirconia grain (#2) within sample $Zr_{0.363}Mg_{0.594}Ce_{0.027}Er_{0.016}O_{1.40}$
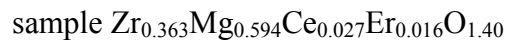
Using energy dispersive spectroscopy it was possible to further confirm the presence of all elements contained within the cubic zirconia phase and the existence of a pure MgO phase as seen in Figure 18. Because of the duplication in information obtained by TEM and the difficulty posed by sample preparation it was abandoned as a primary tool for studies with uranium and plutonium.

### 3.4.5 Conclusions from characterization of cerium oxide containing ceramic

The precipitation method used to synthesize zirconia magnesia inert matrix fuels has been used to produce dual phase material with intimate mixing between phases. Due to the higher degree of mixing, it has been shown to form a solid solution at less severe temperatures (510 $^{o}$C) and durations than the corresponding dry synthesis route as demonstrated by TGA/DSC. Forming a solid solution is essential for this fuels chemical performance. This could be beneficial for fissioning higher actinides with low sublimation temperatures, such as americium, which would not withstand the temperatures required to sinter the ceramic by a dry synthesis route. The $ZrO_2$ requires very little MgO in the presence of $CeO_2$ and $Er_2O_3$ to fully stabilize the cubic zirconia phase. This zirconia phase can accommodate up to 14 % (wt/wt) fissile material and up to 12 % (wt/wt) burnable poison. A consistent 5 % (wt/wt) MgO is contained in the zirconia phase allowing for a reliable estimate of the quantity of the periclase phase that will be present for a given composition. The relative amount of Mg is found to determine the phase composition of the resulting material. With no MgO, $ZrO_2$ is in both baddeleyite and tetragonal phases. As little as 3.2 % (wt/wt) and as much as 6.9 % (wt/wt) MgO resulted in a single cubic zirconia phase. A MgO (periclase) phase precipitated at MgO concentrations at and above 11.5 % (wt/wt) MgO. A third phase of

cubic Ce-Er oxide was found after exceeding the solubility limit of the zirconia. This was found at $ZrO_2$ concentration of 30 % (wt/wt) with Ce and Er concentrations of 8.3 % and 5.2 % (wt/wt) respectively. This phase is also present in the absence of zirconia. The periclase phase remains pure which will allow it to retain its thermophysical properties, most importantly thermal diffusivity and thermal conductivity, and to further improve the reactor-related qualities of the overall ceramic. This characterization study was performed to lay a foundation for dissolution studies of zirconia-magnesia inert matrix fuel under conditions relevant to an advanced fuel cycle with uranium and plutonium.

## 3.5 Characterization of uranium oxide containing ceramics

### 3.5.1 X-ray diffraction (XRD) of uranium oxide containing ceramics

X-ray diffraction was used to determine the crystalline phases present in the prepared samples. For these studies the zirconium oxide to magnesium oxide while holding uranium oxide and erbium oxide at 5% (wt/wt) and 2.5% (wt/wt) respectively with measurements collected according to the procedure in Section 2.4. Table 7 shows the phases present, quantity of phase, space group, and lattice parameters for cubic phases in the samples presented in this study. In the absence of magnesium oxide there exist a tetragonal partially stabilized zirconium oxide and a monoclinic zirconium oxide (baddelyite) as seen in Figure 19, which is consistent with findings from studies performed with cerium oxide (Section 3.4.1).

Table 7: Phases present and lattice parameters for uranium containing samples as determined by x-ray diffraction

| Sample # | Bulk Sample Composition | Phases Present (space group) | Lattice Parameter (nm) | Stoichiometry of Phase | Quantity of Phase (wt. %) |
|---|---|---|---|---|---|
| 1 | $Zr_{0.959}U_{0.024}Er_{0.017}O_{1.99}$ | $ZrO_2(P121/c1)$ | Not Determined | Not Determined | Not Determined |
|  |  | $ZrO_2(P42/nmcS)$ | Not Determined | Not Determined | Not Determined |
| 2 | $Zr_{0.820}Mg_{0.143}U_{0.021}Er_{0.015}O_{1.85}$ | $ZrO_2(Fm-3m)$ | 0.50950(8) | $Zr_{0.816}Mg_{0.142}U_{0.029}Er_{0.012}O_{1.85}$ | 100.0 |
| 3 | $Zr_{0.705}Mg_{0.261}U_{0.020}Er_{0.014}O_{1.73}$ | $ZrO_2(Fm-3m)$ | 0.509527(7) | $Zr_{0.812}Mg_{0.143}U_{0.030}Er_{0.015}O_{1.85}$ | 96.1 |
|  |  | $MgO(Fm-3m)$ | 0.42145(3) | MgO | 3.9 |
| 4 | $Zr_{0.609}Mg_{0.360}U_{0.018}Er_{0.013}O_{1.63}$ | $ZrO_2(Fm-3m)$ | 0.50954(5) | $Zr_{0.800}Mg_{0.155}U_{0.031}Er_{0.013}O_{1.84}$ | 92.6 |
|  |  | $MgO(Fm-3m)$ | 0.42138(0) | MgO | 7.4 |
| 5 | $Zr_{0.527}Mg_{0.445}U_{0.017}Er_{0.012}O_{1.55}$ | $ZrO_2(Fm-3m)$ | 0.50964(6) | $Zr_{0.789}Mg_{0.159}U_{0.035}Er_{0.017}O_{1.83}$ | 79.1 |
|  |  | $MgO(Fm-3m)$ | 0.42136(7) | MgO | 20.9 |
| 6 | $Zr_{0.395}Mg_{0.580}U_{0.014}Er_{0.010}O_{1.41}$ | $ZrO_2(Fm-3m)$ | 0.50996(4) | $Zr_{0.791}Mg_{0.151}U_{0.038}Er_{0.020}O_{1.84}$ | 64.6 |
|  |  | $MgO(Fm-3m)$ | 0.42134(2) | MgO | 35.4 |
| 7 | $Zr_{0.251}Mg_{0.728}U_{0.012}Er_{0.009}O_{1.27}$ | $ZrO_2(Fm-3m)$ | 0.51053(2) | $Zr_{0.788}Mg_{0.136}U_{0.050}Er_{0.027}O_{1.85}$ | 44.1 |
|  |  | $MgO(Fm-3m)$ | 0.42124(7) | MgO | 55.9 |
| 8 | $Zr_{0.148}Mg_{0.834}U_{0.010}Er_{0.007}O_{1.16}$ | $ZrO_2(Fm-3m)$ | 0.51173(3) | $Zr_{0.763}Mg_{0.131}U_{0.071}Er_{0.035}O_{1.85}$ | 26.2 |
|  |  | $MgO(Fm-3m)$ | 0.42123(0) | MgO | 73.8 |
| 9 | $Zr_{0.070}Mg_{0.914}U_{0.009}Er_{0.006}O_{1.08}$ | $ZrO_2(Fm-3m)$ | 0.51487(5) | Not Determined | 16.7 |
|  |  | $MgO(Fm-3m)$ | 0.42120(4) | MgO | 83.3 |
| 10 | $Mg_{0.986}U_{0.008}Er_{0.006}O_{1.01}$ | $MgO(Fm-3m)$ | 0.42129(8) | MgO | Not Determined |
|  |  | $U_xEr_yO_{2x+1.5y}(Fm-3m)$ | 0.54421(7) | Not Determined | Not Determined |
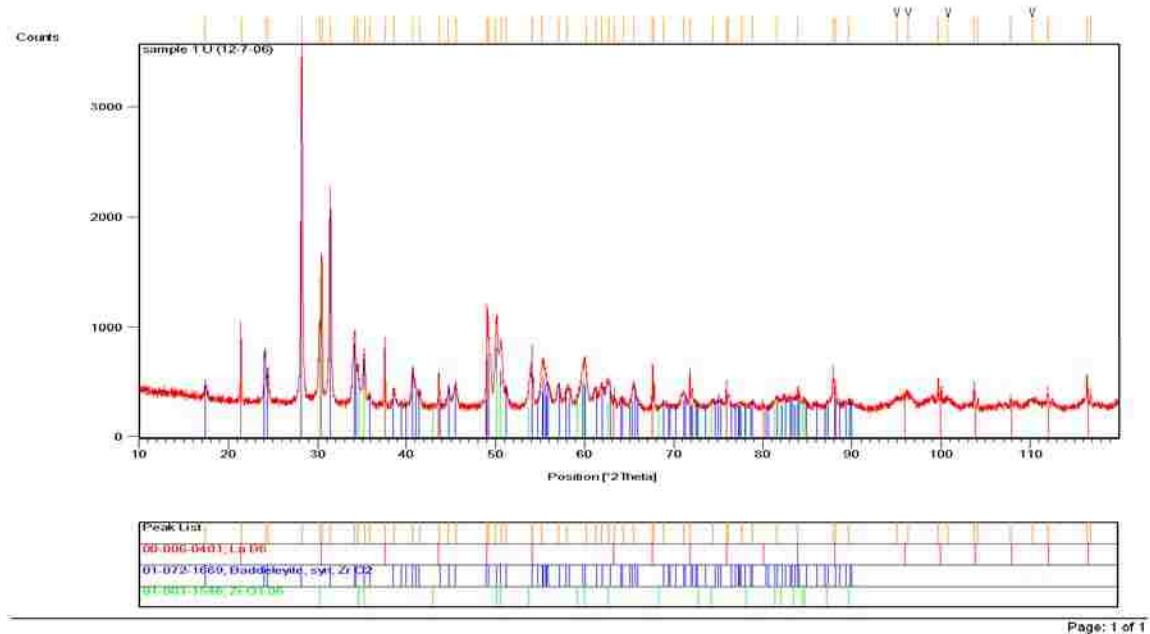
Figure 19: X-ray diffraction pattern of $Zr_{0.959}U_{0.024}Er_{0.017}O_{1.99}$ identifying baddeleyite and partially stabilized tetragonal zirconium oxide

Also consistent with previous studies of cerium containing ceramics (Section 3.4.1), as little as 5 % (wt/wt) MgO fully stabilized the zirconia resulting in a single cubic zirconia phase [Figure 20]. The solubility limit of Mg within the zirconia phase was exceeded at 10 % (wt/wt) resulting in the precipitation of an MgO (periclase) phase that represented 3.9 % (wt/wt) of the sample by Reitveld and least square analysis [Figure 21]. This shows the limit of the isomorphic substitution of Mg within zirconia to be 6-7 wt. % under these conditions. This is consistent with previous studies with cerium that showed the range of single phase zirconium to be between 3.2 and 6.9 wt. % (Section 3.4.1).
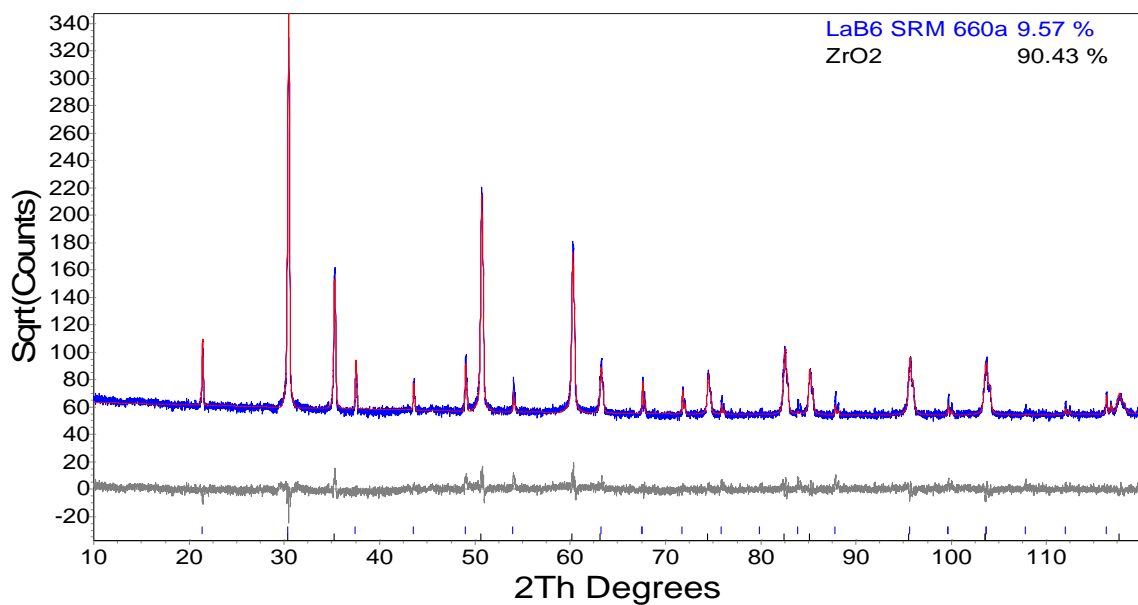
Figure 20: X-ray diffraction pattern of $Zr_{0.820}Mg_{0.143}U_{0.021}Er_{0.015}O_{1.85}$ (red) with fit (blue) and difference curve (grey).
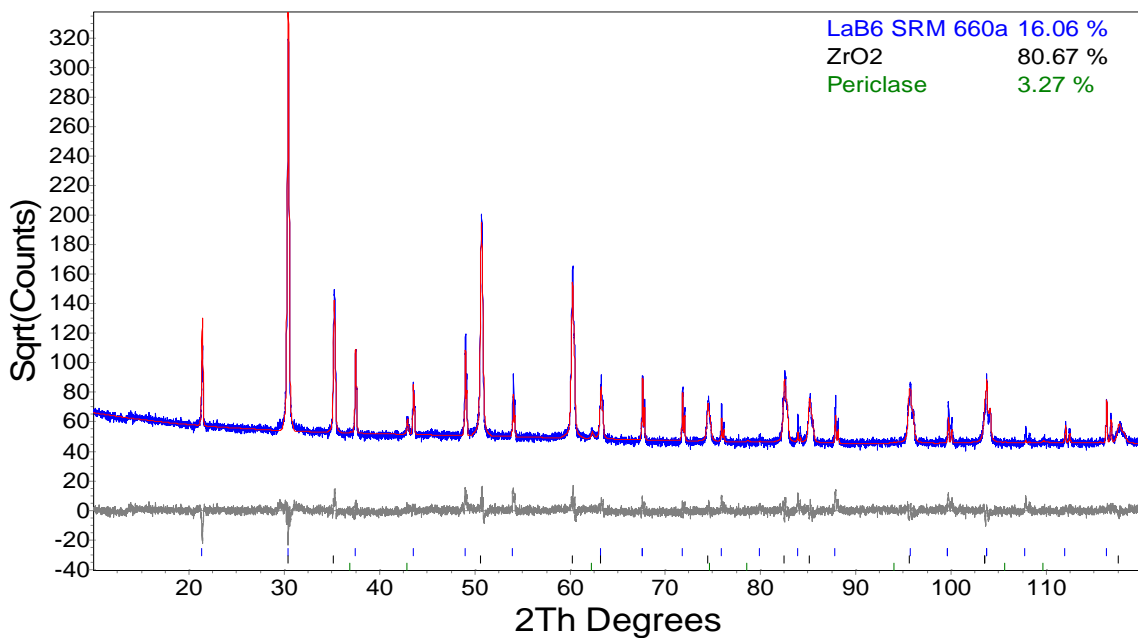


Figure 21: X-ray diffraction pattern of $Zr_{0.705}Mg_{0.261}U_{0.020}Er_{0.014}O_{1.73}$ (red) with fit (blue) and difference curve (grey).

This two phase mixture persists from 10 % to 75 % (wt/wt) MgO. The lattice parameter

of the periclase phase agrees with published data and remains unchanged for all samples,

which indicates it is a pure phase with low affinity for any of the larger cations within the

fuel [Table 7]. The appearance of this periclase phase enables one to specifically design

thermophysical fuel properties in regard to thermal diffusivity and thermal conductivity

to further control centerline temperature of the inert matrix fuel pellet under reactor

conditions. With as little as 17.5 wt. % $ZrO_2$, there is still no evidence that the solubility

limits of uranium and erbium in zirconia have been exceeded and a third phase consisting

of uranium and erbium oxide was not observed [Figure 22]. This would indicate uranium

oxide solubility in zirconia that exceeds that of cerium oxide. This significant difference

between the behavior of plutonium homologs is further discussed in Section 3.5.3.



Figure 22: X-ray diffraction pattern of $Zr_{0.070}Mg_{0.914}U_{0.009}Er_{0.006}O_{1.08}$ (red) with fit (blue)

and difference curve (grey).

The continued expansion of the lattice parameter suggests that both cations are incorporated into the zirconia lattice by isomorphic substitution as seen in Table 7. This suggests that the limit of isomorphic substitution for uranium oxide in zirconia is higher than that of cerium oxide (Section 3.4.5) and is further discussed below in electron probe microanalysis studies. In the absence of zirconium oxide, uranium and erbium oxide form a cubic solid solution similar to that of cerium oxide (Section 3.4.1) as seen in Figure 23.
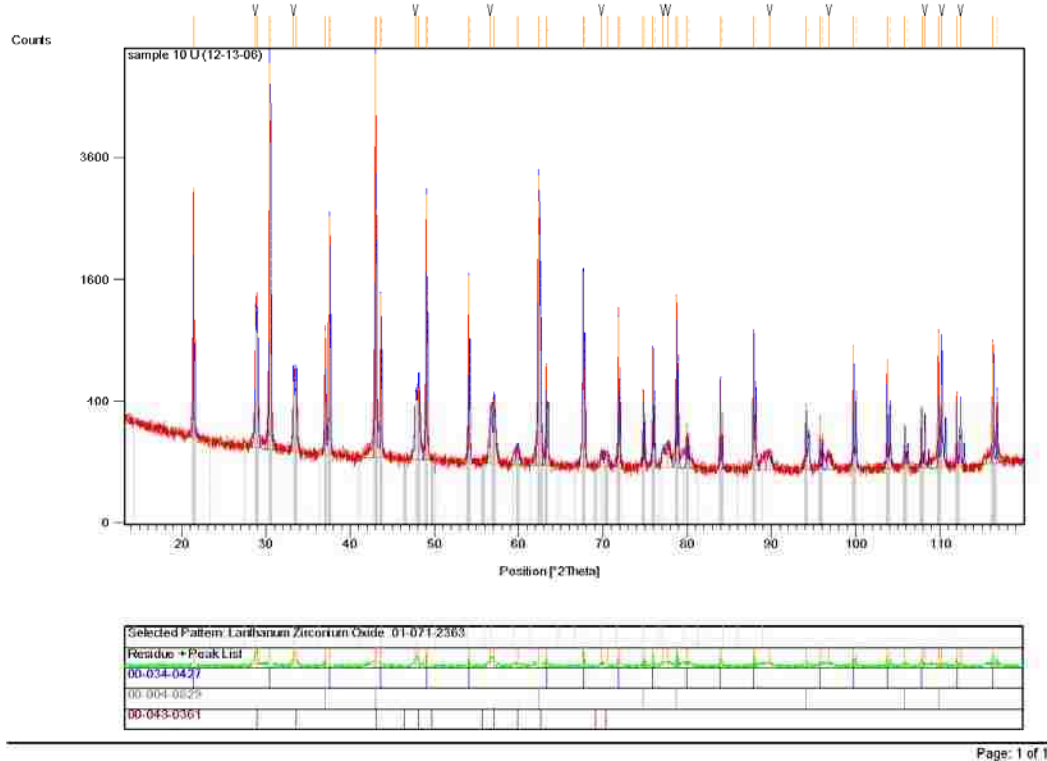


Figure 23: X-ray diffraction pattern of $Mg_{0.986}U_{0.008}Er_{0.006}O_{1.01}$ identifying periclase, cubic zirconia and cubic uranium-erbium oxide solid solution

3.5.2 Optical microscopy of uranium oxide containing ceramic

Optical microscopy proved to be a useful tool to visualize phase mixing and pore space. The ceramics consist of a periclase phase (dark gray) and a zirconia solid solution phase (light gray). The two phases are intimately mixed throughout all compositions [Figure 24] showing similar behavior to previous studies with cerium (Section 3.4.2). This allows a pathway for internal heat to be transferred to the peripheral of the pellet through the interconnected periclase phase.
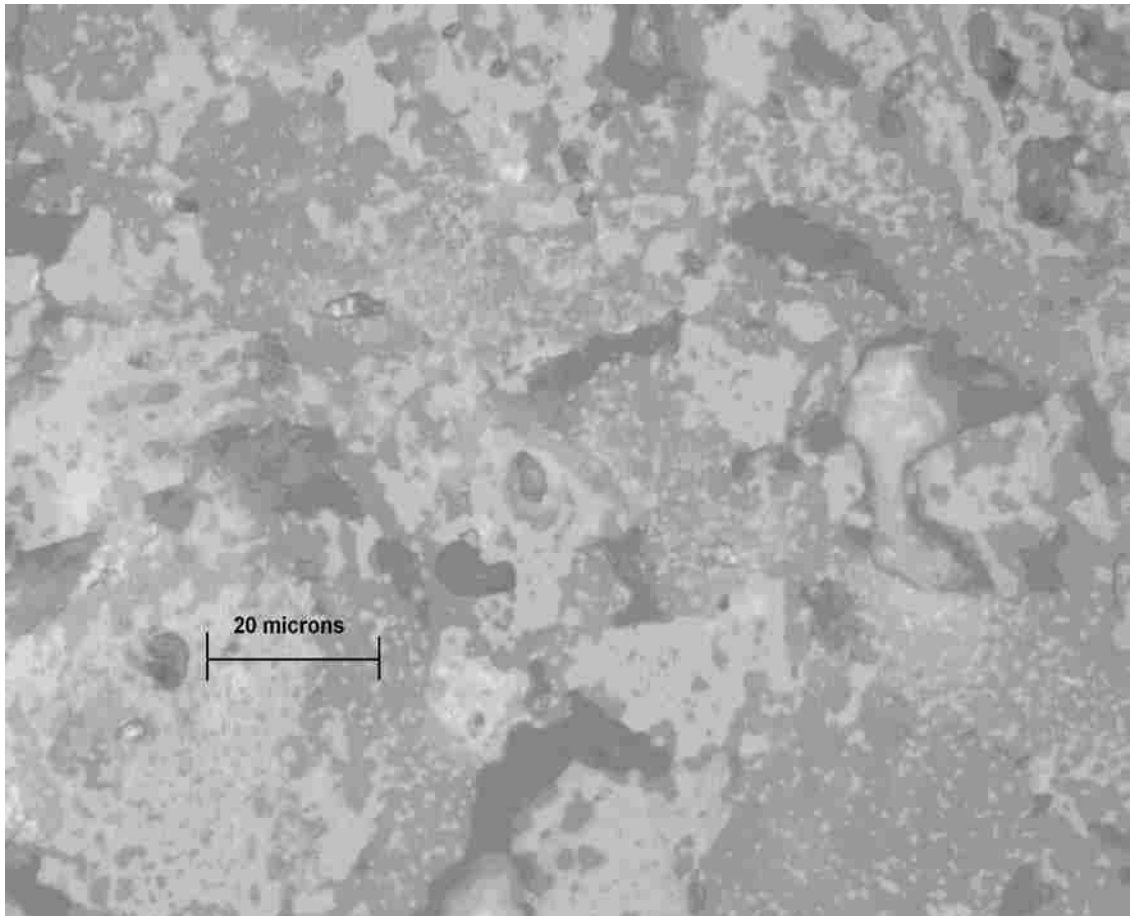


Figure 24: Optical microscopy of $Zr_{0.251}Mg_{0.728}U_{0.012}Er_{0.009}O_{1.27}$ at 1000x magnification.

The light grey is zirconia phase, dark grey is magnesia,

and the darkest areas are pore space.

### 3.5.3 Electron probe microanalysis of uranium oxide containing ceramic

Electron probe microanalysis was used to determine elemental distributions over wide spatial areas (9 $mm^2$). The zirconium, erbium, and uranium maps are identical showing an even distribution of all three elements throughout the zirconia phase [Figure 25]. There is a faint outline of the zirconia phase within the magnesium map showing that a small amount of magnesium is also evenly distributed within the zirconia phase. The magnesium map also contains bright features in samples that have a periclase phase.
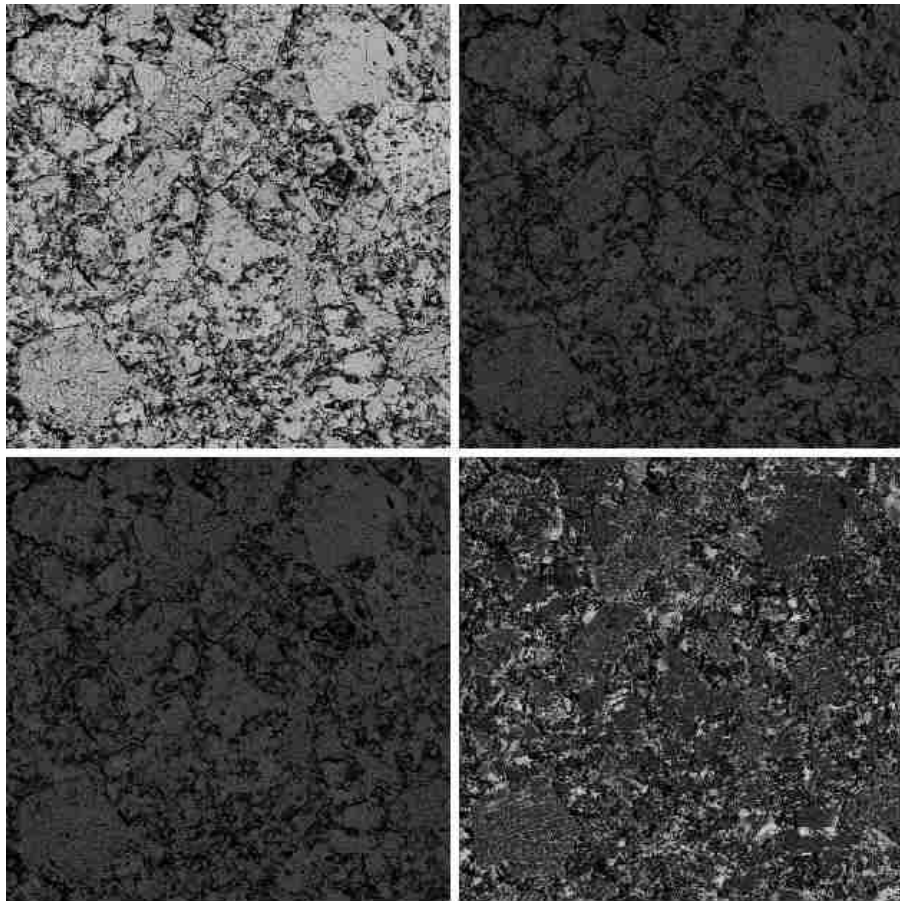


Figure 25: Elemental maps by electron probe microanalysis over 9 $mm^2$ of Zr Lα (top left), U Mα (top right), Er Lα (bottom left), and Mg Kα (bottom right) in sample $Zr_{0.527}Mg_{0.445}U_{0.017}Er_{0.012}O_{1.55}$

These bright spots are areas with high concentrations of magnesium, which correspond to locations that do not have evidence of containing any other element, with the exception of oxygen. This is further indication that the periclase phase is pure and has a low affinity for the other elements used in the fuel.

Electron probe microanalysis was also used to determine the concentrations of each element in a small beam interaction volume of 1-9 $\mu m^3$. In this way it was possible to determine the stoichiometry of each phase. Areas that were probed without any overlap from neighboring phases were used. It was determined that the magnesium oxide phase contained less than 1 wt.-percent of all elements other than magnesium and oxygen. This confirms that the periclase phase is pure MgO as was suggested by the constant lattice parameter determined by XRD. The zirconia phase was determined to have a constant amount of Mg. The Mg content in the zirconia phase was 5 % $\pm$ 1 % (wt/wt) for all compositions as it was in previous studies with cerium (Section 3.4.3). However, since the total zirconium content is decreasing and the $UO_2$ and $Er_2O_3$ are held constant within the entire pellet, the relative amount of uranium and erbium in the zirconia phase increases. The concentrations of uranium and erbium start at 5 % and 2.5 % (wt/wt) respectively as expected for a pellet that is exclusively cubic zirconia. As the zirconium concentration is decreased the uranium and erbium content is measured to be as high as 15.2(4) and 5.41(5) wt. % respectively in the zirconia phase. It was not possible to probe the sample with the lowest zirconium content by microprobe due to spot size and interference from the dominant periclase phase. However, since there is no additional phases present by XRD, it can be assumed that the uranium and erbium content in zirconia under these conditions is as high as 20 % and 10 % (wt/wt) respectively. This is

slightly higher than the maximum solubility of cerium, which was found to be 16 wt. %

at 12% (wt/wt) erbium under similar conditions (Section 3.4.3) a noted difference in the

structural behavior between a tetravalent lanthanide and actinide. This could be due to

the added 2 wt.-percent of the erbium oxide in cerium containing samples and not due to

any differences between cerium and uranium. Without a detailed systematic study it is

difficult to determine the cause of such differences. A graph of composition within the

zirconia as a function of increasing magnesium content in the total ceramic is shown in

Figure 26. The magnesium content within the zirconia phase, shown in green, does not

increase with increasing magnesium content of the pellet, while uranium and erbium,

shown in blue and red respectively, increase as the total amount of zirconia is decreased

thereby increasing the uranium and erbium content within it.
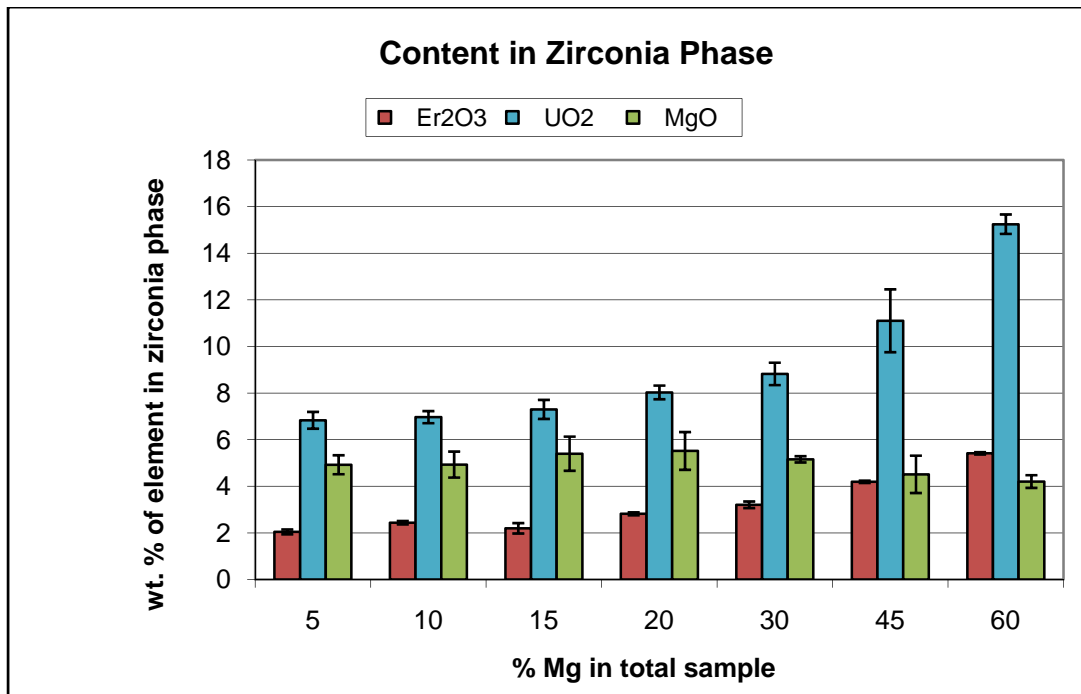


Figure 26: Stoichiometry of the zirconia phase as determined by electron probe

microanalysis (error bars represent standard deviation within a sample)

3.5.4 X -ray absorption fine structure for uranium containing ceramic

X-ray absorption fine structure (XAFS) was performed at the Advanced Photon
Source, BESSERC-CAT 12, in an effort to describe local distortions in the zirconia
lattice due to the incorporation of uranium. It was found that although the average lattice
parameter changed over the compositional range due to the incorporation of uranium and
erbium within the lattice as shown by XRD, the local structure around both zirconium
and uranium was consistent from sample to sample within the limits of the measurement
(0.002 nm) as shown in Table 8.

Table 8: Local bond distances for uranium and zirconium within zirconia as determined
by x-ray absorption fine structure (error on the measurements is 0.002 nm)

| Sample | Zr-O (nm) | U-O (nm) | Zr-Zr (nm) | U-Zr (nm) |
|---|---|---|---|---|
| $Zr_{0.820}Mg_{0.143}U_{0.021}Er_{0.015}O_{1.85}$ | 0.215 | 0.229 | 0.355 | 0.364 |
| $Zr_{0.609}Mg_{0.360}U_{0.018}Er_{0.013}O_{1.63}$ | 0.213 | 0.232 | 0.353 | 0.362 |
| $Zr_{0.527}Mg_{0.445}U_{0.017}Er_{0.012}O_{1.55}$ | 0.214 | 0.232 | 0.358 | 0.364 |
| $Zr_{0.395}Mg_{0.580}U_{0.014}Er_{0.010}O_{1.41}$ | 0.215 | 0.232 | 0.354 | 0.363 |
| $Zr_{0.251}Mg_{0.728}U_{0.012}Er_{0.009}O_{1.27}$ | 0.214 | 0.232 | 0.354 | 0.364 |
| $Zr_{0.148}Mg_{0.834}U_{0.010}Er_{0.007}O_{1.16}$ | 0.216 | 0.231 | 0.355 | 0.363 |
| $Zr_{0.070}Mg_{0.914}U_{0.009}Er_{0.006}O_{1.08}$ | 0.216 | 0.231 | 0.356 | 0.365 |
| average | 0.215 | 0.231 | 0.355 | 0.364 |
| difference due to U | 0.016 | | 0.009 | |

The zirconium to first shell oxygen distance was shown to be 0.215(2) nm, while the
uranium to first shell oxygen distance is 0.231(2) nm resulting in a deformation of 0.016
nm in the first shell oxygen distance due to uranium incorporation into the lattice. The
zirconium to second shell zirconium distance was determined to be 0.355(2) nm and the

uranium to second shell zirconium distance was determined to be 0.364(2) nm resulting in a deformation in the metal to metal distance of 0.009 nm. In this way it was possible to quantify the bond deformation in zirconia due to the incorporation of uranium into the lattice. A typical spectrum with fit is shown in Figure 27.
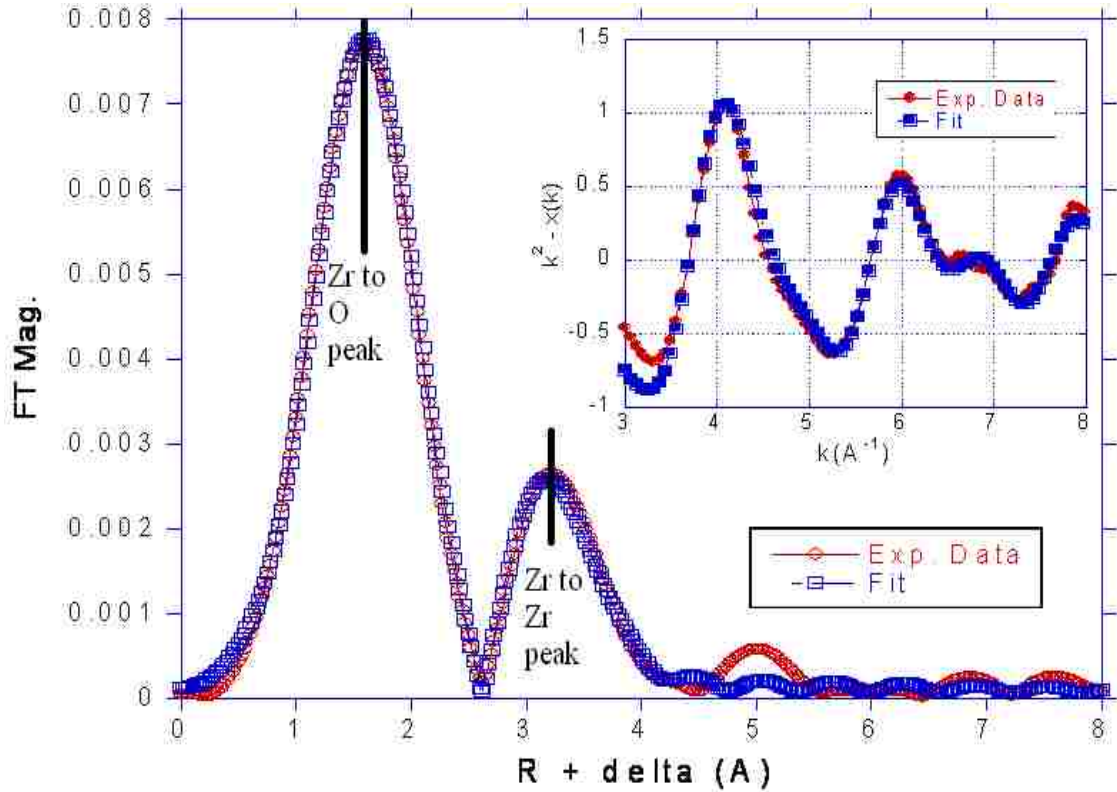


Figure 27: Fourier transform with fit of X-ray absorption fine structure spectra for $Zr_{0.251}Mg_{0.728}U_{0.012}Er_{0.009}O_{1.27}$ (inset is spectra with fit in k space)
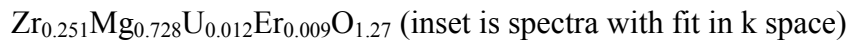
3.5.5 Conclusions from characterization of uranium oxide containing ceramic

Uranium containing inert matrix fuel was successfully synthesized in a two phase ceramic consisting of cubic zirconia and periclase. The periclase phase remains pure showing a low affinity for all other cations in the ceramic, which will allow it to retain its

thermophysical properties, most importantly thermal conductivity and thermal diffusivity. Magnesium, uranium, and erbium are able to substitute in the zirconia lattice at different levels to create a solid solution.  Magnesium concentrations within the zirconia phase remains constant at 5 wt. %.  Uranium and erbium concentrations within the zirconia were as high as 20 and 10 % (wt/wt) respectively.  These findings are confirmed by x-ray diffraction and electron microprobe analysis and further agree with previous studies performed with cerium as a plutonium homolog although the solubility limit for uranium was found to be higher than that of cerium within the zirconia under these conditions.  It is unclear if this is a difference in behavior between the lanthanide and actinide or if it is due to different levels of substituting erbium oxide within the zirconia.  The bond deformation due to the incorporation of uranium into the zirconia lattice was determined in the first two atomic shells by XAFS and found to be 0.016 nm in the first shell oxygen and 0.009 nm in the second shell cations.

### 3.6 Characterization of plutonium oxide containing ceramic

### 3.6.1 X-ray diffraction of plutonium oxide containing ceramic

X-ray diffraction was used to identify and quantify crystalline phases present in the plutonium containing ceramic.  It was found in the sample with the lowest MgO concentration (3 wt. % MgO) that there was only a cubic zirconia phase, indicating that all other species were dissolved in the zirconia lattice [Figure 28].  Once the MgO concentration is raised to 11 wt. % it exceeds the solubility limit for isomorphic substitution and precipitates as cubic MgO (periclase) [Figure 29].  This is expected as the solubility limit for MgO in zirconia under similar conditions was determined in

previous studies to be 3.2 – 6.9 % (wt/wt) (Section 3.4.1).  This two phase mixture of

zirconia and periclase was found in all samples with more than 7 wt. % MgO.
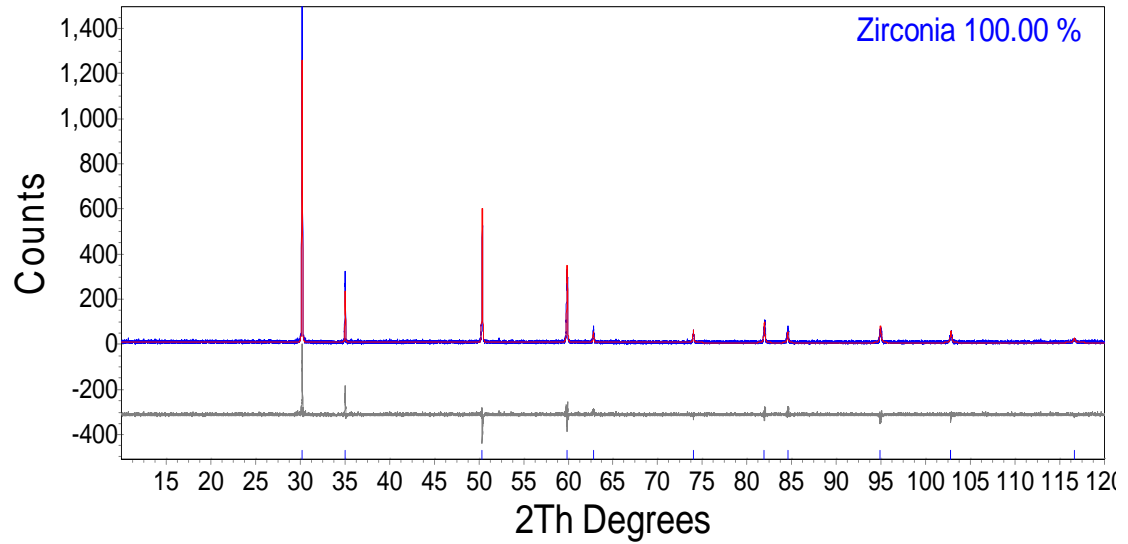


Figure 28: X-ray diffraction pattern of $Zr_{0.76}Mg_{0.10}Pu_{0.078}Er_{0.062}O_{1.9}$ (blue) with fit (red)

and difference curve (grey).
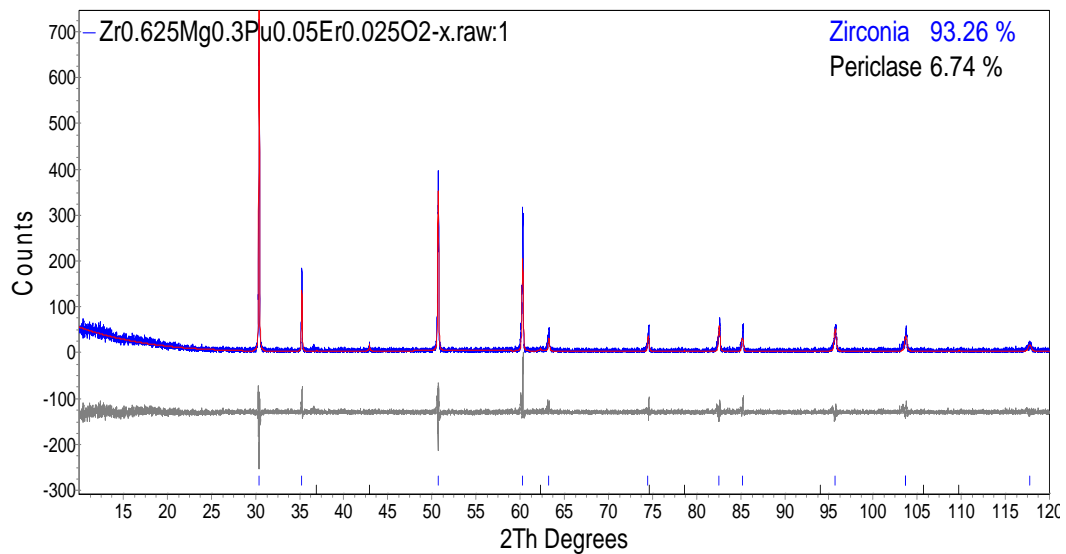


Figure 29: X-ray diffraction pattern of $Zr_{0.64}Mg_{0.29}Pu_{0.029}Er_{0.041}O_{1.7}$ (blue) with fit (red)

and difference curve (grey).

The lattice parameter for the periclase phase remains consistent and is independent of the concentration of other elements suggesting that it is pure MgO and no other elements are incorporated into the lattice [Table 9]. The lattice parameter for the zirconia increases with increasing plutonium content indicating that plutonium is isomorphically substituted into the zirconia lattice as shown in Table 9. This is further evidence that a third plutonium or erbium rich phase is not present, even as an amorphous material. The zirconium oxide concentration of the total pellet was decreased to 16 wt. % with no evidence of third phase formation [Figure 30]. This indicates the solubility limit for plutonium and erbium within the zirconia phase is high enough to accommodate a wide range of zirconia to magnesia ratios. The solubility limit of plutonium and erbium in zirconia is further discussed below in the electron microprobe section [Section 3.6.3].
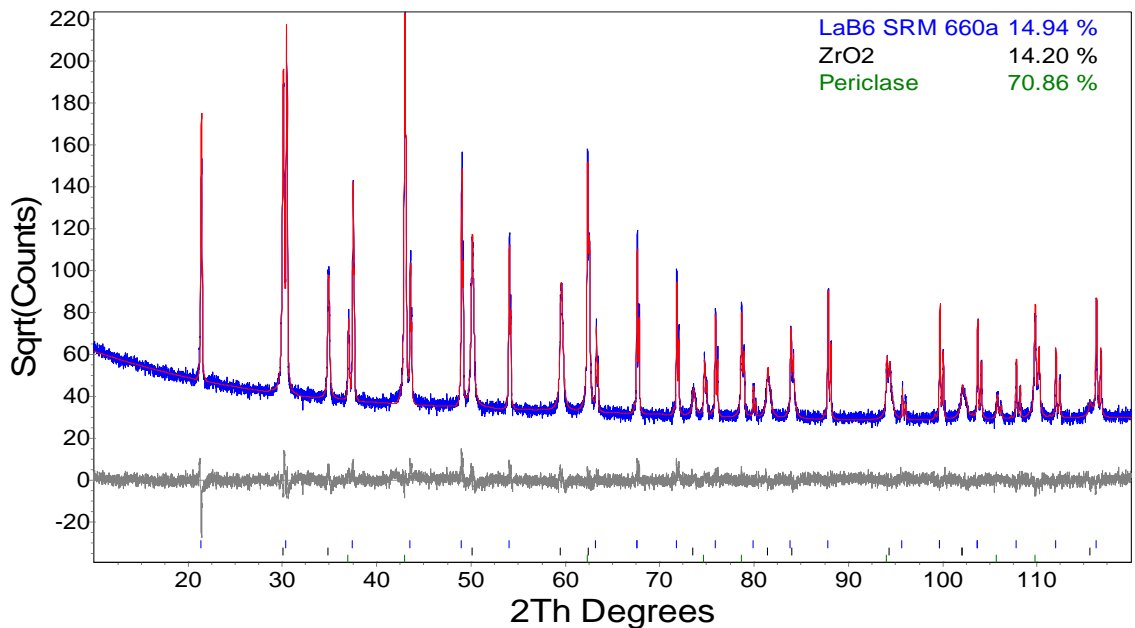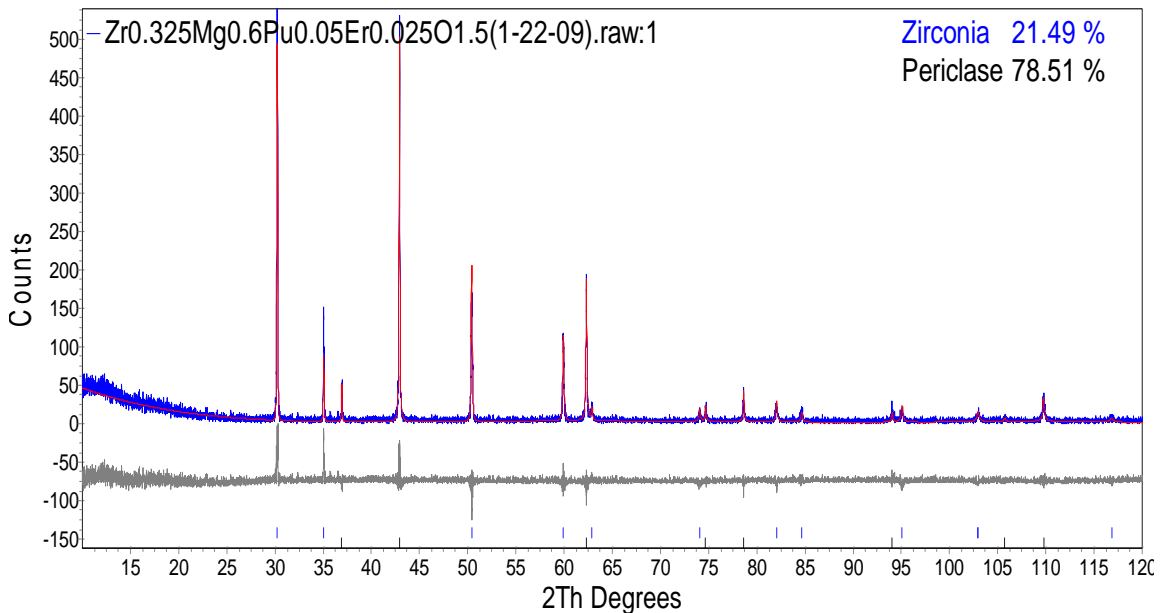


Figure 30: X-ray diffraction pattern of $Zr_{0.061}Mg_{0.93}Pu_{0.0059}Er_{0.0045}O_{1.1}$ (blue) with fit (red) and difference curve (grey).

### 3.6.2 Optical microscopy of plutonium oxide containing ceramic

Optical microscopy proved to be a useful tool in visualizing phase mixing and pore space. By optical microscopy it was easy to distinguish the zirconia (light gray), magnesia (dark gray) and pore space (black). It was observed that even at MgO phase concentrations as low as 6.7 wt. % the phase is still evenly distributed throughout the sample with an intimate phase mixing [Figure 31]. This intimate mixing is evident through all samples and shows an interconnected MgO phase at 51.8 wt. % periclase [Figure 32]. This interconnected periclase phase will allow thermal diffusivity from the center of the pellet to the peripheral because of its superior heat transfer properties, thereby lowering the centerline temperature of the fuel.
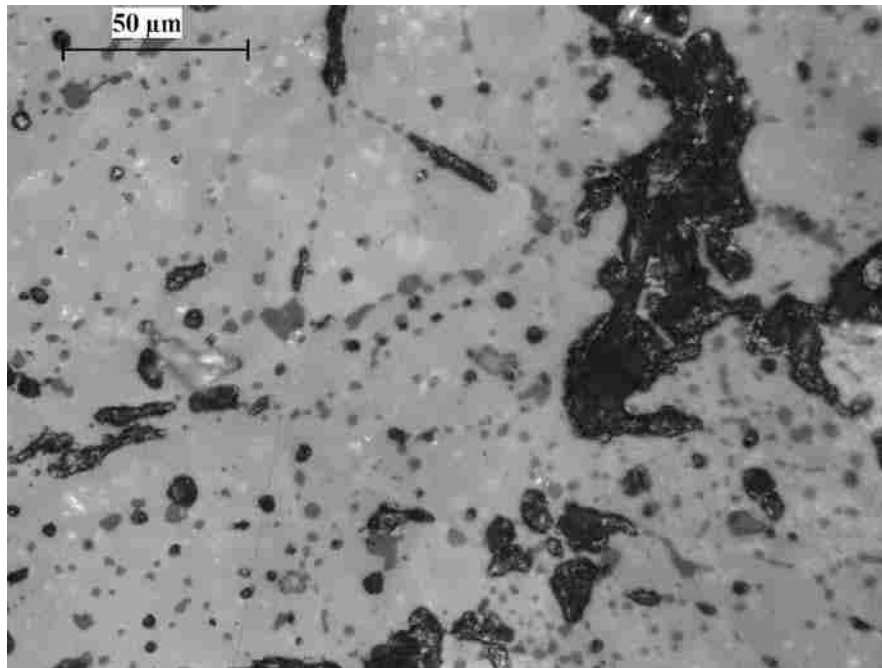


Figure 31: Optical microscopy image at 500x magnification of

$Zr_{0.64}Mg_{0.29}Pu_{0.029}Er_{0.041}O_{1.7}$
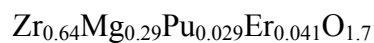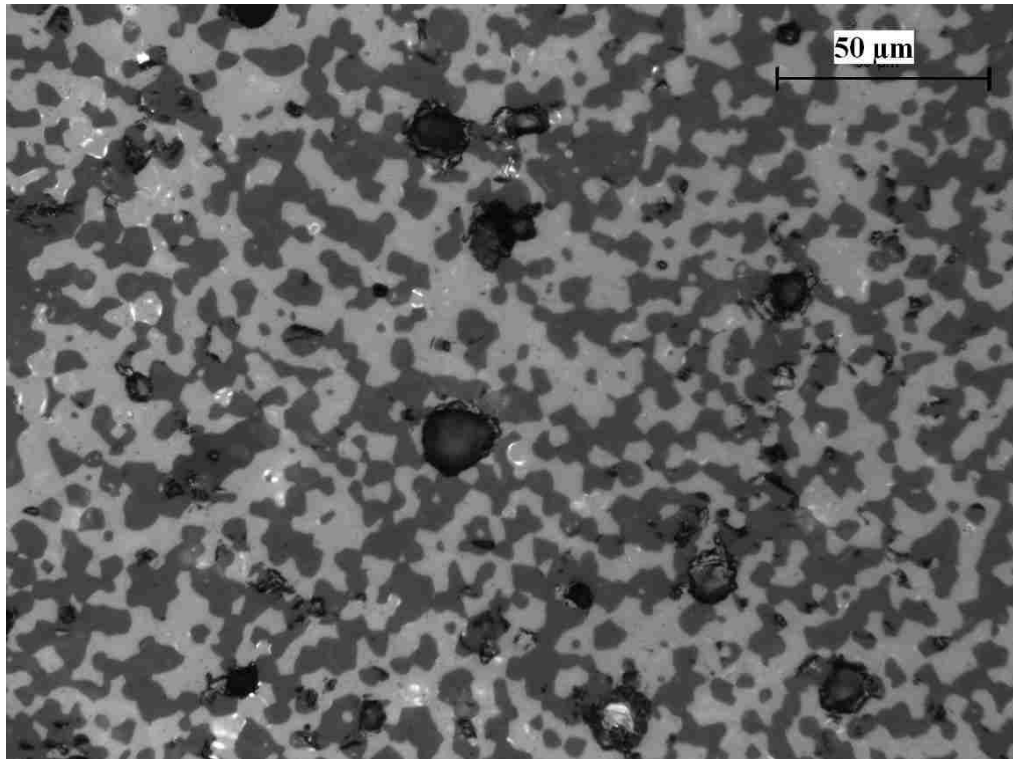
Figure 32: Optical microscopy image at 500x magnification of

$Zr_{0.21}Mg_{0.77}Pu_{0.011}Er_{0.0078}O_{1.2}$
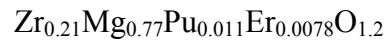
3.6.3 Electron probe microanalysis of plutonium oxide containing ceramic

Electron probe microanalysis was used to scan over an area of the polished surface to map relative concentrations of zirconium, magnesium, plutonium, erbium, and oxygen. In this way it is possible to identify elements that have affinity for the same phase and those that are exclusive to a phase as previously identified by x-ray diffraction. All pellets examined exhibited the same characteristics. The periclase phase was shown to have no affinity for any elements other than magnesium and oxygen as previously suggested by the constant lattice parameter of the x-ray diffraction pattern [Figure 33].
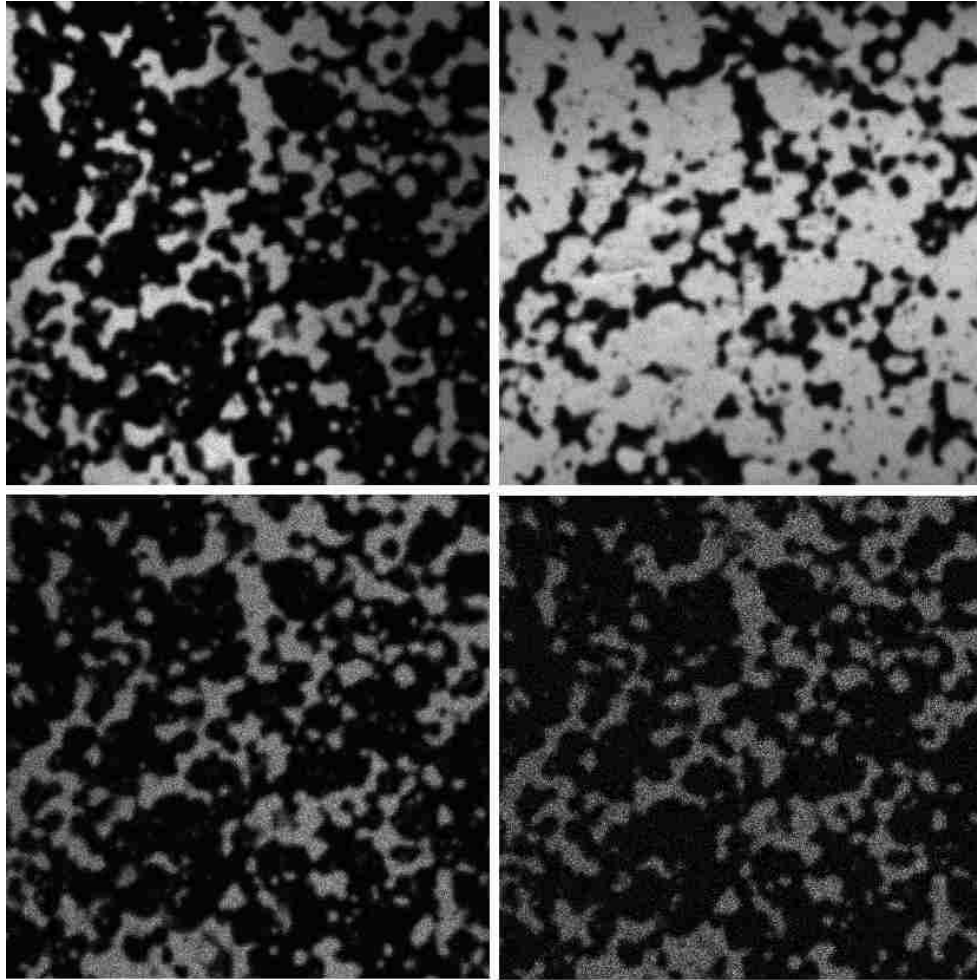
Figure 33: Elemental maps by electron probe microanalysis over 120 μm x 120 μm of Zr Lα (top left), Mg Kα (top right), Pu Mα (bottom left), and Er Lα (bottom right) from sample $Zr_{0.093}Mg_{0.89}Pu_{0.0065}Er_{0.0052}O_{1.1}$

The zirconia phase incorporates a small amount of magnesium into the lattice as indicated by a faint trace of the zirconia phase in a magnesium map. All of the plutonium, erbium, and zirconia are evenly distributed throughout the zirconia phase [Figure 33]. This will simplify modeling of the material as only two phases need to be considered and is an improvement over previous attempts at synthesizing a plutonium containing zirconia-magnesia inert matrix fuel which resulted in a three phase material

(55).  This method also verified that both phases have a high degree of homogeneity in each phase.

### 3.6.4 Secondary electron microscopy and energy dispersion spectroscopy

A secondary electron microscope equipped with an energy dispersive spectrometer was used to take semiquantitative measurements in small areas (~2-5 microns) in an effort to quantify the elements present in each phase [Figure 34].  In this way it was
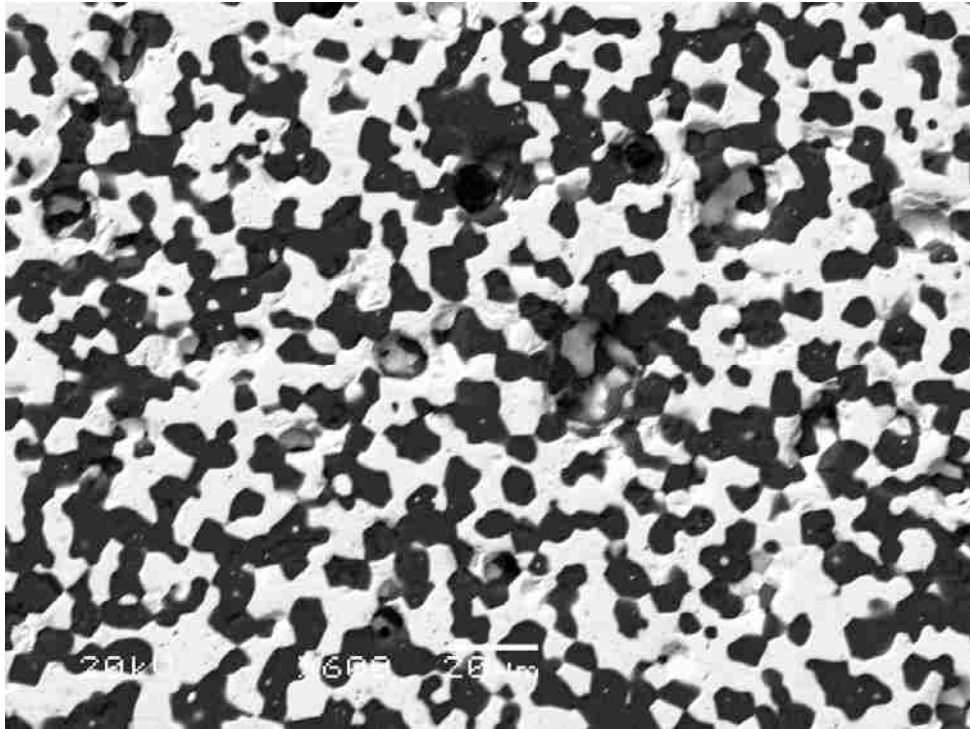


Figure 34: Secondary electron image of $Zr_{0.21}Mg_{0.77}Pu_{0.011}Er_{0.0078}O_{1.2}$ (zirconia appears as white, periclase as dark grey, and pore space as black)

confirmed that the periclase phase is pure MgO.  The zirconia phase is more complicated, because it incorporates all cations involved by isomorphic substitution.  Magnesium was found in the zirconia phase at a constant 3-4 wt. % over all samples which defines the

limit of isomorphic substitution of magnesium in the zirconia phase. This is within the range of 3-7 wt. % established by similar studies (Sections 3.4.3 and 3.5.3). There was no limit found for plutonium or erbium within the range of samples synthesized in this study. Plutonium content within the zirconia phase was as high as 16 wt. % and erbium content reached as high as 12 wt. % within the zirconia phase. This erbium content is more comparable to the composition of the cerium containing ceramic and the plutonium is 2 wt. % higher without reaching a solubility limit for the plutonium as was the case for cerium. This would suggest that there may be a difference in the solubility limit in the zirconia between actinides and lanthanides as was suggested by the solubility limit of uranium. Due to the semi-quantitative nature of the plutonium measurement and the lack of establishing a solubility limit, it is not possible to conclusively determine a difference. It is noted here as an observation for further study. This allows for loading the needed fissile material even at low concentrations of zirconium oxide resulting in high concentration of plutonium and erbium within the zirconia phase. A summary of quantitative results for the content of the zirconia phase by energy dispersive spectroscopy is shown in the stoichiometry column in Table 9.

3.6.5 Conclusions from characterizing plutonium oxide containing ceramic

A zirconia-magnesia inert matrix fuel containing plutonium oxide as the fissile material and erbium oxide as a burnable poison was successfully synthesized as a dual phase ceramic using a precipitation method over a range of compositions. This material was characterized by x-ray diffraction in an effort to identify and quantify crystalline phases present. It was shown in most samples that the material consisted of cubic zirconia and cubic MgO (periclase). Optical microscopy was used to visualize phase

mixing, microstructure, and pore space. Electron probe microanalysis was used to map elemental concentrations over wide areas. This demonstrated the homogeneity of each phase and confirmed that plutonium and erbium are incorporated into the zirconia phase resulting in a solid solution. This is the first time this inert matrix has been synthesized as a dual phase material with plutonium oxide and a burnable poison. The homogeneity of the zirconia solid solution will aid in modeling the chemical behavior of the material. Secondary electron microscopy equipped with energy dispersive spectroscopy was used to determine the stoichiometry of each phase. It was found that the periclase phase was pure MgO. This will allow it to retain its heat transfer properties, specifically thermal diffusivity and thermal conductivity. Analysis of the zirconia phase shows a presence of all cations involved to different concentrations. Magnesium is incorporated into the zirconia at 3-4 wt. % which defines the limit of isomorphic substitution for magnesium in zirconia. The solubility limits of plutonium and erbium in zirconia were not reached, however the highest concentration of plutonium and erbium found in the zirconia were 16 and 12 wt. % respectively. This high solubility limit will allow fissile material to be loaded into the fuel even at low concentrations of zirconium oxide. This also suggests a possible difference between the solubility limit of tetravalent actinides and lanthanides in zirconia. A table summarizing the quantitative data obtained in the study of plutonium oxide containing inert matrix fuel is found below. These studies are aimed at understanding the material for dissolution studies in conditions of interest to an advanced fuel cycle.

Table 9: Phases present, quantity, and lattice parameters determined by x-ray diffraction as well as phase stoichiometry determined by SEM/EDS.

| Composition of Sample | Phases Present | Lattice Parameter (Å) | Phase Stoichiometry | Quantity of Phase (wt/wt) |
|---|---|---|---|---|
| $Zr_{0.76}Mg_{0.10}Pu_{0.078}Er_{0.062}O_{1.9}$ | $ZrO_2$ (cubic zirconia) | 5.1215(15) | $Zr_{0.71}Mg_{0.03}Pu_{0.16}Er_{0.09}O_{1.9}$ | 100 |
| $Zr_{0.64}Mg_{0.29}Pu_{0.029}Er_{0.041}O_{1.7}$ | $ZrO_2$ (cubic zirconia) | 5.0905(19) | $Zr_{0.81}Mg_{0.04}Pu_{0.08}Er_{0.08}O_{1.94}$ | 93.3 |
|  | MgO (periclase) | 4.2126(17) | MgO | 6.7 |
| $Zr_{0.56}Mg_{0.36}Pu_{0.037}Er_{0.044}O_{1.6}$ | $ZrO_2$ (cubic zirconia) | 5.0973(16) | $Zr_{0.76}Mg_{0.031}Pu_{0.11}Er_{0.092}O_{1.91}$ | 88.7 |
|  | MgO (periclase) | 4.2133(13) | MgO | 11.3 |
| $Zr_{0.44}Mg_{0.47}Pu_{0.042}Er_{0.048}O_{1.5}$ | $ZrO_2$ (cubic zirconia) | 5.1086(13) | $Zr_{0.7}Mg_{0.03}Pu_{0.15}Er_{0.12}O_{1.91}$ | 82.2 |
|  | MgO (periclase) | 4.2129(11) | MgO | 17.8 |
| $Zr_{0.21}Mg_{0.77}Pu_{0.011}Er_{0.0078}O_{1.2}$ | $ZrO_2$ (cubic zirconia) | 5.0984(15) | $Zr_{0.82}Mg_{0.036}Pu_{0.092}Er_{0.046}O_{1.93}$ | 48.2 |
|  | MgO (periclase) | 4.2110(12) | MgO | 51.84 |
| $Zr_{0.093}Mg_{0.89}Pu_{0.0065}Er_{0.0052}O_{1.1}$ | $ZrO_2$ (cubic zirconia) | 5.1042(21) | $Zr_{0.78}Mg_{0.031}Pu_{0.12}Er_{0.069}O_{1.93}$ | 29.2 |
|  | MgO (periclase) | 4.2169(17) | MgO | 70.8 |
| $Zr_{0.061}Mg_{0.93}Pu_{0.0059}Er_{0.0045}O_{1.1}$ | $ZrO_2$ (cubic zirconia) | 5.1160(20) | $Zr_{0.73}Mg_{0.031}Pu_{0.16}Er_{0.085}O_{1.93}$ | 21.5 |
|  | MgO (periclase) | 4.2117(16) | MgO | 78.5 |

CHAPTER 4

AQUEOUS DISSOLUTION STUDIES

4.1 Aqueous dissolution studies with cerium containing ceramic

Aqueous dissolution studies on cerium containing ceramic were performed to establish procedures for assessing the material in reactor and repository conditions. This section describes the results of dissolution studies performed in high temperature high pressure water to simulated reactor conditions in the event of a cladding failure and a Soxhlet corrosion study to establish its resistance to corrosion by water over long periods of time as in environmental conditions.

4.1.1 Soxhlet corrosion study with cerium containing ceramic

Compositions used in aqueous dissolution of cerium containing samples are listed in Table 10. The progress of corrosion was investigated using a Soxhlet apparatus [Figure 35] and samples analyzed by mass loss. Samples gained mass for the first several hours



Figure 35: Soxhlet apparatus for corrosion experiments. Cellulose thimbles seen in chamber to suspend sample above water volume.

due to water absorption into pore space. The mass gained differed for each pellet due to variations in accessible pore space and density, but was consistent for a single pellet over the course of the study. This was proven by drying the sample in an oven at $90^{\circ}C$ periodically during the study. The samples consistently returned to the same "wet" mass as was established before drying within 48 hours. Because of this, samples were not dried before determining mass, but blotted dry with a kimwipe and the "wet" mass was used to determine corrosion progress. This decreased handling and reduced the amount of time the samples were out of the Soxhlet for measuring.

Table 10: Oxide concentrations in samples used for aqueous dissolution study (wt. %)

| sample # | % $ZrO_2$ | % MgO | % $CeO_2$ | % $ErO_{1.5}$ |
|----------|-----------|-------|-----------|---------------|
| 1 | 94.3 | 0.0 | 3.5 | 2.2 |
| 2 | 86.5 | 6.9 | 4.1 | 2.5 |
| 3 | 58.6 | 31.4 | 6.2 | 3.9 |
| 4 | 30.3 | 56.3 | 8.3 | 5.2 |

The mass loss of samples over the course of the experiment follows linear kinetics due to the solution never approaching equilibrium. Samples that have low amounts of magnesium oxide content (0 and 6.9 wt. % MgO) show little to no corrosion for the 2,000 hours that the experiment was carried out [Figure 36]. This is due to the absence of a magnesium oxide phase. The zirconia phase shows no measurable corrosion in this study.
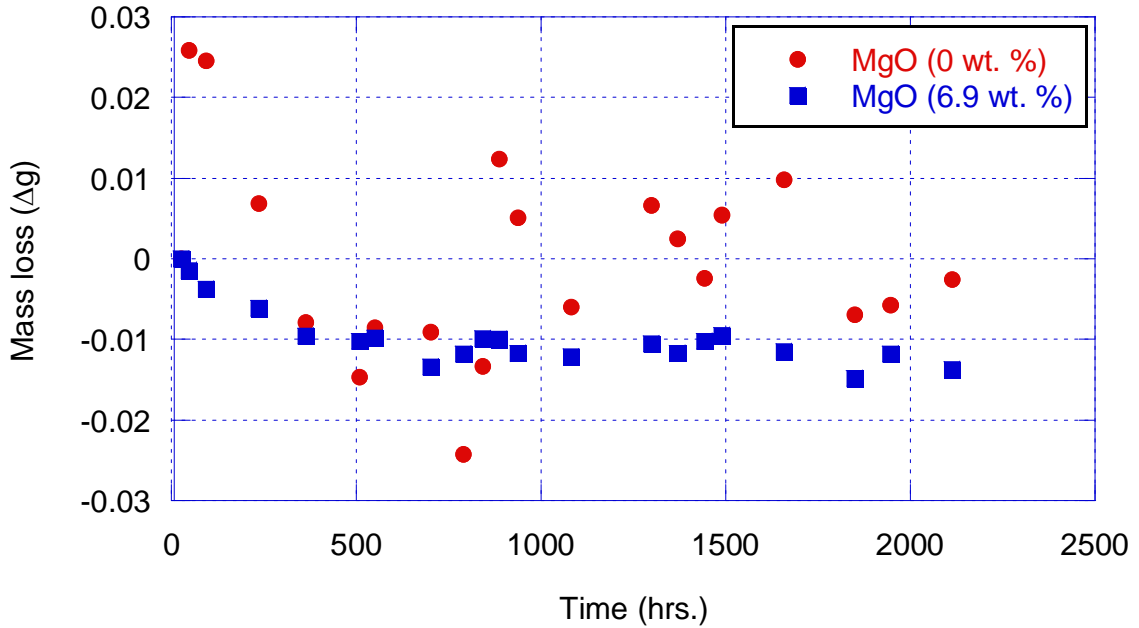
Figure 36: Corrosion via Soxhlet apparatus of cerium containing ceramics with low MgO concentrations

When the magnesium oxide content is increased it forms a periclase phase, which has the potential to undergo hydration to magnesium hydroxide and subsequent dissolution. Samples were assessed by mass loss so that initial weight was not a factor. This was determined by simply subtracting the initial mass by the mass at time (t) as seen in the equation below.

$$2) \; \text{Mass (initial)} - \text{Mass (t)} = \text{Mass loss } (\Delta g)$$

Because of this there is a measureable corrosion rate when the sample contains a magnesium oxide phase as seen in Figure 37. This sample contains 31 wt. % MgO and has a mass loss of 0.0297±0.0017 mg/h.
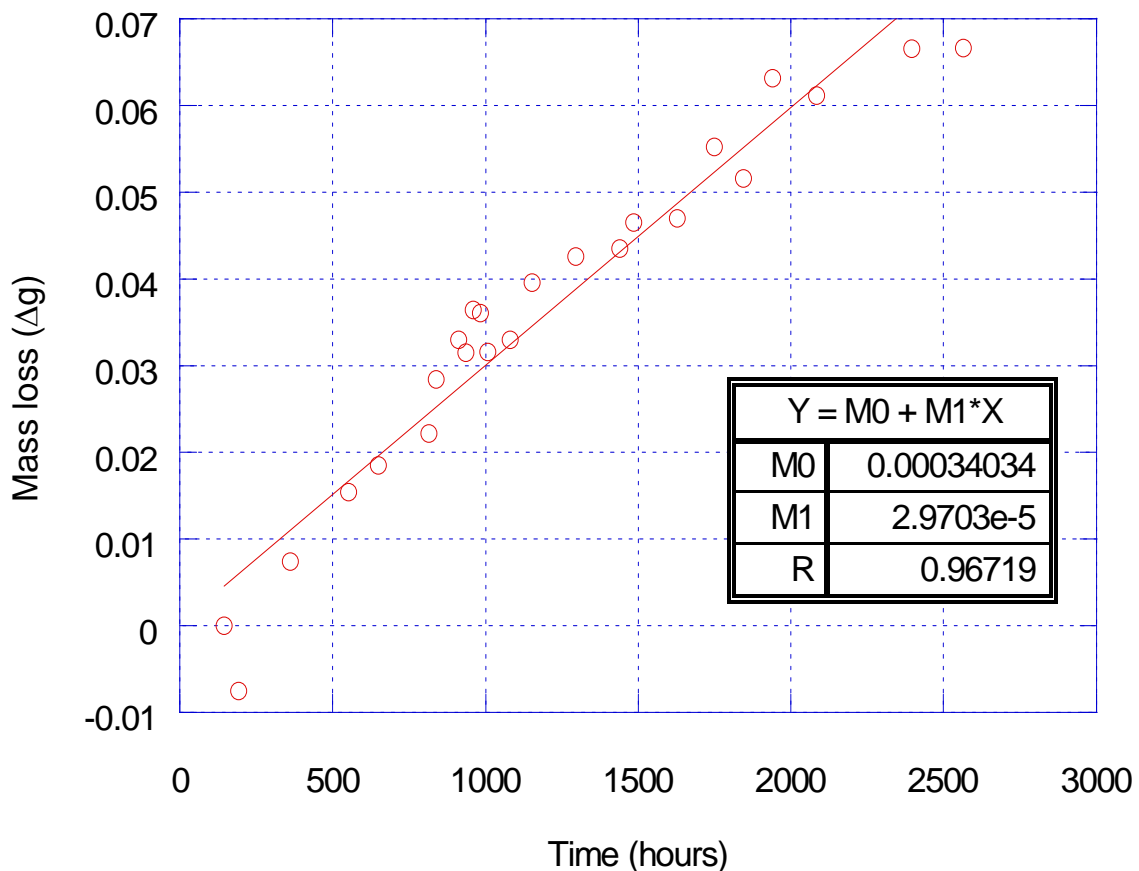
Figure 37: Mass loss via Soxhlet for cerium containing sample with 31 wt. % MgO

As the MgO content is further increased the corrosion rate also increases. This can be seen in a sample containing 56 wt. % MgO. In this sample the magnesium oxide content is nearly double that of the previous sample at 31 wt. % MgO. The resulting corrosion rate is nearly an order of magnitude higher at 0.107±0.005 mg/h as seen in Figure 38. These studies were performed to lay a foundation for further studies with the actinides. It was found that there was no measureable corrosion of the zirconia phase and therefore corrosion was due exclusively to the amount of magnesium oxide present in the sample. The magnesium oxide was hydrolyzed to magnesium hydroxide (identified by

microscopy) that was then dissolved.  The rate of corrosion increased nearly tenfold for an increase in magnesium oxide content from 31 to 56 wt. %.
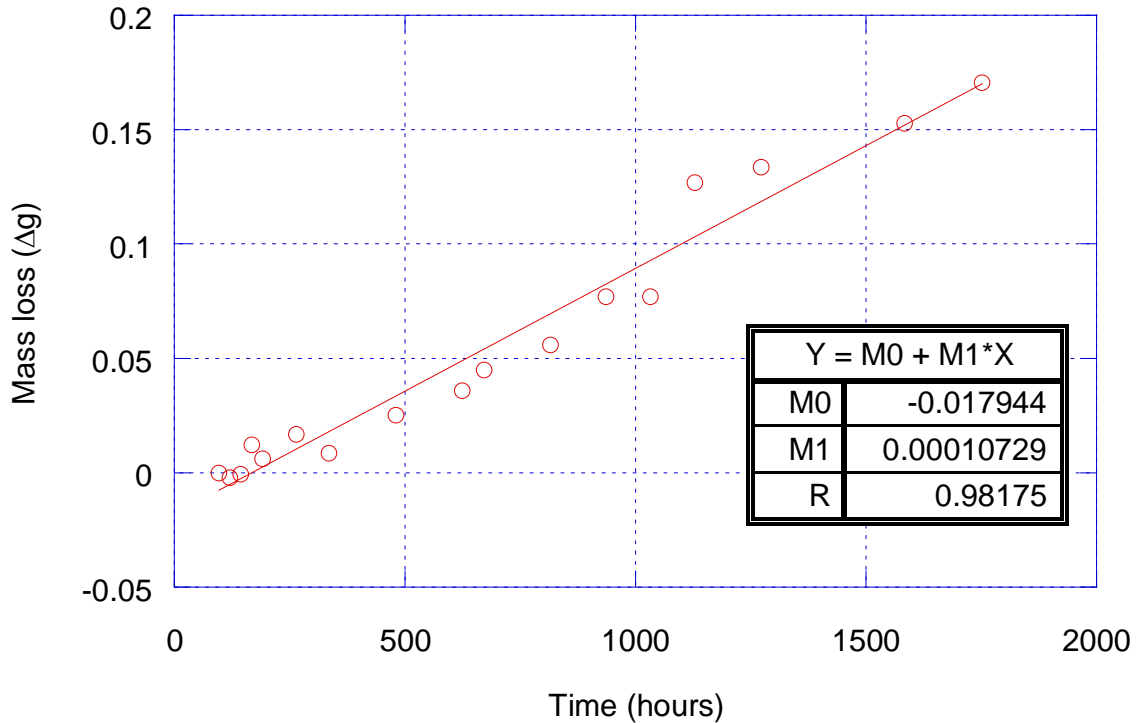


Figure 38: Corrosion via Soxhlet for cerium containing sample with 56 wt. % MgO

4.1.2 Pressure vessel dissolution study with cerium containing ceramic

To test the corrosion of the inert matrix fuel in conditions relevant to a reactor a pressure vessel was used to perform dissolution studies at high temperature and pressure. The pressure vessel was operated for 500 hours for each sample.  Samples were place in a sample cup within the pressure vessel filled with deionized water.  The sample cup was located in the middle of the vessel volume.  The vessel was also equipped with a swage lock port for *in situ* sampling and a stirring mechanism [Figure 39].  Samples were heated to 300°C which resulted pressures of 10.3 MPa.
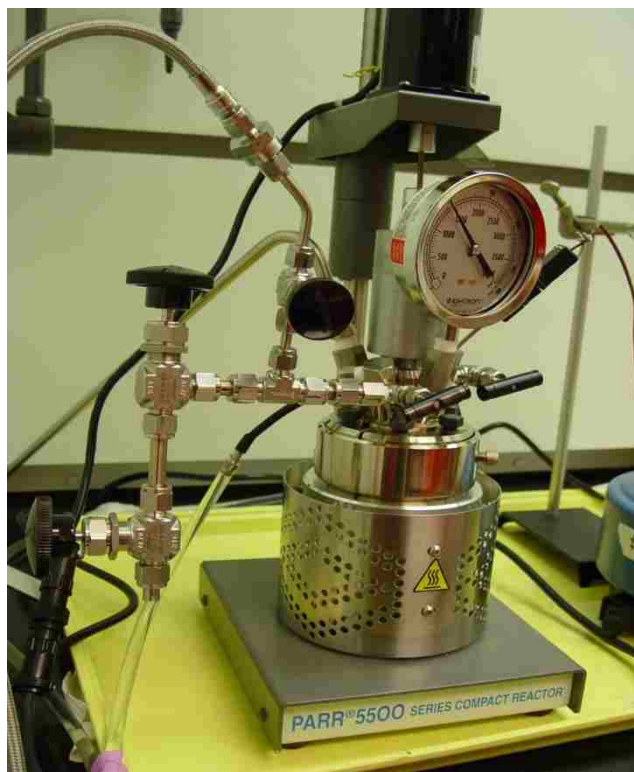
Figure 39: Pressure vessel equipped with stirring mechanism

and swage lock for *in situ* sampling.

The corrosion properties of two compositions ($Zr_{0.771}Mg_{0.188}Ce_{0.026}Er_{0.014}O_{1.80}$ and $Zr_{0.571}Mg_{0.387}Ce_{0.027}Er_{0.015}O_{1.61}$) were tested via the pressure vessel to simulate reactor conditions in the event of a cladding failure. It was found that within 48 hours the pellets were physically destroyed and reduce to a powder, mainly consisting of zirconia. The zirconia appeared to remain intact and there was no measureable level of zirconium, cerium, or erbium as determined by ICP-AES in the solution. The magnesium oxide phase was almost completely dissolved through the mechanical destruction of the pellet by turbid water and subsequent dissolution of MgO to $Mg(OH)_2$ by hydrolysis. The maximum time for these experiments was 250 hours. They were performed as a basis for experiments with actinides.

### 4.1.3 Conclusions from aqueous dissolution of cerium containing ceramics

Aqueous dissolution studies were performed with cerium oxide containing ceramic in order to establish protocols and validate procedures with non-radioactive material. These studies have also been used to assess the effectiveness of cerium as a plutonium homolog both structurally and chemically. These studies have found that zirconia is a highly resilient material that does not dissolve or release material incorporated into its matrix in aqueous media as tested in these experiments. The corrosion of the material is dictated by its magnesium oxide content. Once this magnesium oxide concentration is greater than 30 wt. % there is a measurable corrosion rate. This corrosion rate increases by almost an order of magnitude when the magnesium oxide concentration is nearly doubled to 56 wt. %. Experiments were performed to simulate dissolution under reactor conditions in the event of a cladding failure. These experiments performed with turbid water at $300^{o}C$ found that the fuel pellet was physically destroyed within 48 hours, but there was no evidence of dissolution of the zirconia phase or any of its components for up to 250 hours. These studies have been effective in establishing parameters and procedures to be used with actinide containing inert matrix fuel.

### 4.2 Aqueous dissolution studies with uranium containing ceramic

Uranium dissolution studies in aqueous media were performed in an effort to find a more suitable chemical homolog for plutonium. Studies were performed in a pressure vessel to simulate reactor conditions in the event of a cladding failure. Studies were also performed to assess the durability of the material as a waste form in environmental

conditions should it be used in a "once through" fuel cycle and go to a long term geological repository.

### 4.2.1 Soxhlet corrosion study with uranium containing ceramic

Samples behaved similar to those that contained cerium and were therefore treated with the same procedure (Section 4.1.1). Compositions used in aqueous dissolution of uranium containing samples are listed in Table 11.

Table 11: Composition of uranium containing ceramics in aqueous dissolution (wt. %)

| Sample # | $ZrO_2$ % | MgO % | $UO_2$ % | $ErO_{1.5}$ % |
|:---:|:---:|:---:|:---:|:---:|
| 1 | 72.5 | 20 | 5 | 2.5 |
| 2 | 62.5 | 30 | 5 | 2.5 |
| 3 | 47.5 | 45 | 5 | 2.5 |
| 4 | 32.5 | 60 | 5 | 2.5 |
| 5 | 0 | 92.5 | 5 | 2.5 |

Samples achieved their maximum mass after two hundred hours. This maximum mass was used to determine the mass loss over the course of the experiment and only masses taken after the maximum was achieved are plotted. In this way all samples can be assessed independently of their uptake of water, which is dependent on accessible pore space not chemical composition. Mass losses were normalized to geometric surface area to account for differences in size from one sample to the next.

The dissolution kinetics of the samples roughly followed a linear rate as expected, since the solution is never allowed to approach equilibrium. The two samples with the

highest zirconium oxide concentration ($Zr_{0.527}Mg_{0.445}U_{0.017}Er_{0.012}O_{1.55}$ and $Zr_{0.395}Mg_{0.580}U_{0.014}Er_{0.010}O_{1.41}$) show very little corrosion over the 2,000 hours of the experiment. A linear fit was used to establish a rate of mass loss of $0.012\pm0.002$ $g/m^2h$. The samples with little and no zirconium concentration ($Zr_{0.148}Mg_{0.834}U_{0.010}Er_{0.007}O_{1.16}$ and $Mg_{0.986}U_{0.008}Er_{0.006}O_{1.01}$) showed similar corrosion kinetics to each other at a mass loss of $0.102\pm0.006$ and $0.092\pm0.003$ $g/m^2h$, which is nearly an order of magnitude higher than samples with high levels of zirconium oxide. A sample with zirconium oxide concentrations in between these two groups ($Zr_{0.251}Mg_{0.728}U_{0.012}Er_{0.009}O_{1.27}$) of samples showed a moderate corrosion rate of $0.039\pm0.005$ $g/m^2h$. This gradient of corrosion rates based on zirconium oxide content can be seen in Figure 40.
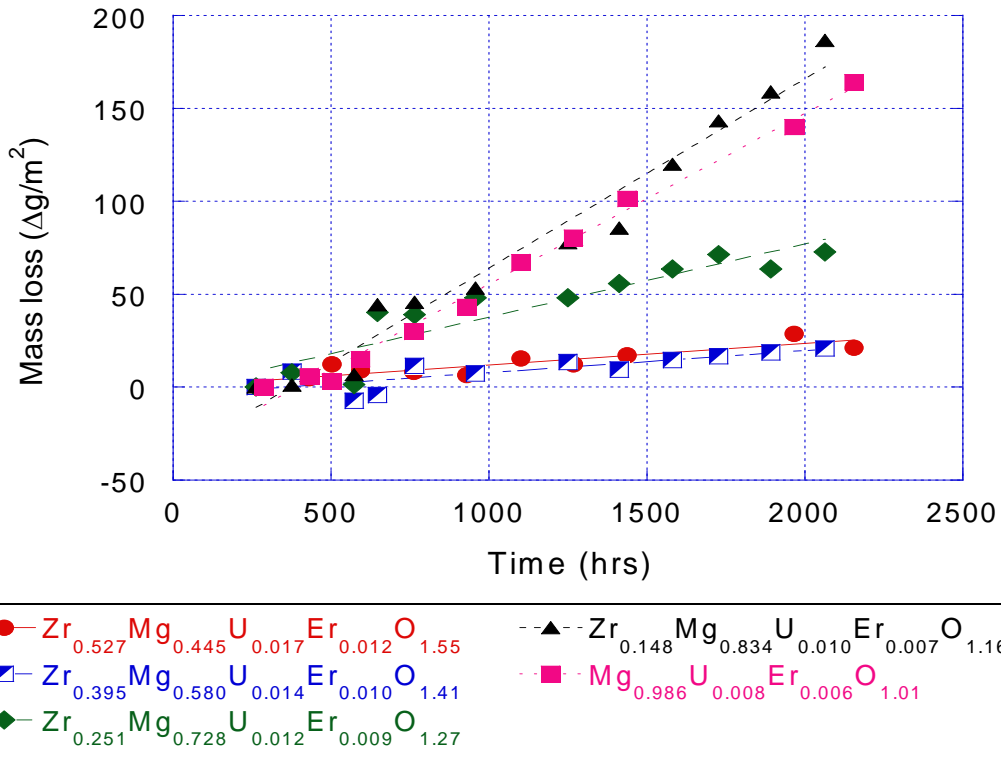


Figure 40: Normalized mass loss of uranium containing zirconia-magnesia inert matrix fuel over time with linear fit from corrosion in a Soxhlet apparatus

The pellets were analyzed by secondary electron microscopy after being exposed to water via the Soxhlet apparatus. It was found that there was increased cracking and irregularity on the surface with increasing magnesium oxide content. This can be seen in three samples examined at low magnification (500x) to view a representative surface of the pellet in Figure 41. At low magnesium oxide content the surface appears relatively unchanged [Figure 41a]. As the magnesium oxide content is increased large cracks appear at the surface [Figure 41b]. When the magnesium oxide content is increased further an irregular surface is formed in addition to the cracks [Figure 41c]. Upon examination at higher magnification, large plate-like morphologies were identified that were not present in the samples before being exposed to water. These plate-like structures increased in size and number with increasing magnesium oxide content of the sample after the corrosion study [Figure 42]. They seem to be concentrated in pore space [Figure 43] and cracks [Figure 44], which could be due to preferential nucleation in these areas or added protection from dissolution after formation due to location. These plate structures were determined to contain magnesium and oxygen by energy dispersive spectroscopy. X-ray diffraction identified a brucite ($Mg(OH)_2$) phase in samples after being exposed to water by the Soxhlet apparatus and this was therefore determined to be the phase of the plates observed within the samples. The hexagonal nature of the microstructure further suggests that this new phase is brucite.

a)



b)



c)
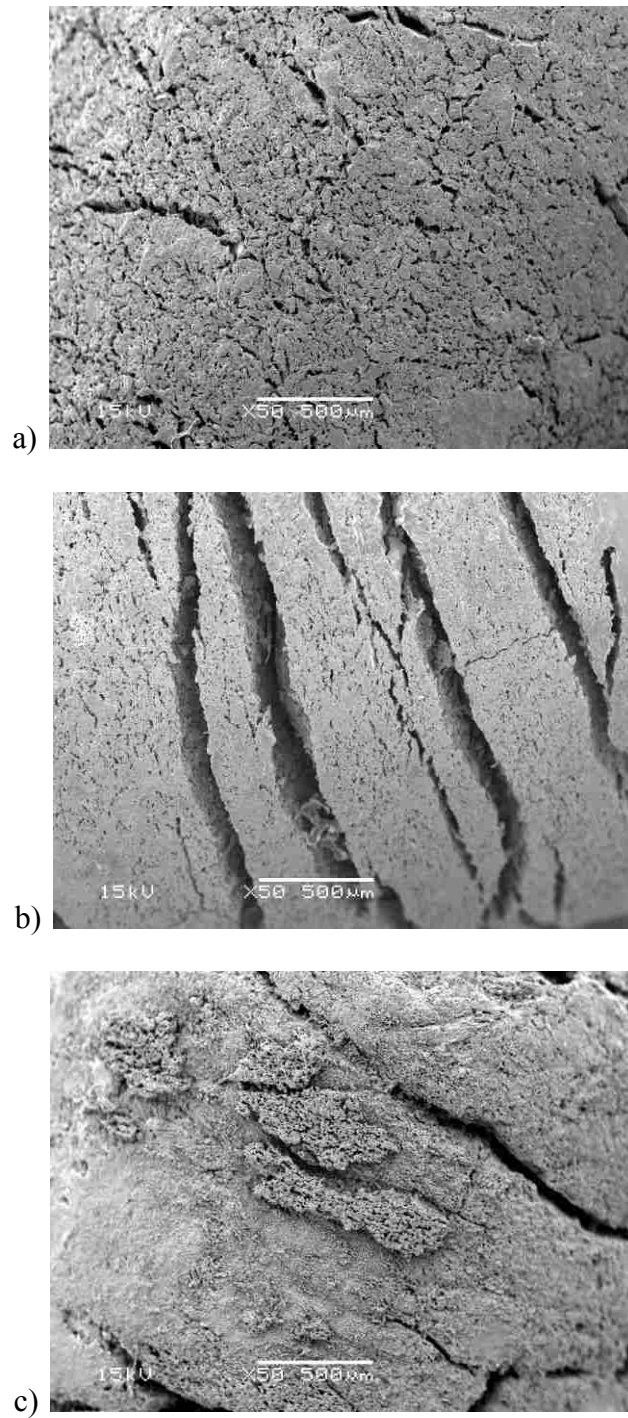
Figure 41: SEM images of surface corrosion over increasing magnesium oxide content after corrosion test with Soxhlet apparatus.  a) $Zr_{0.395}Mg_{0.580}U_{0.014}Er_{0.010}O_{1.41}$  b) $Zr_{0.251}Mg_{0.728}U_{0.012}Er_{0.009}O_{1.27}$  c) $Zr_{0.148}Mg_{0.834}U_{0.010}Er_{0.007}O_{1.16}$

a)                                                        b)
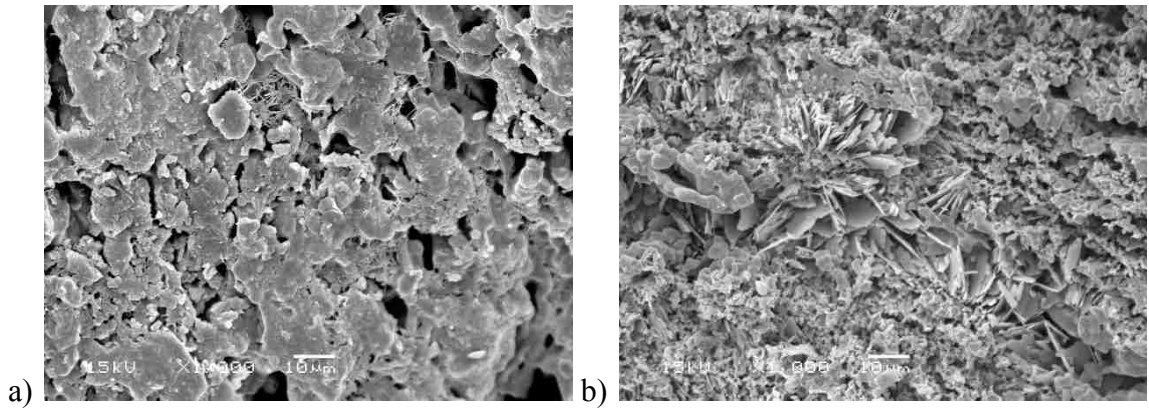
Figure 42: SEM images at 1,000x of $Mg(OH)_2$ plate microstructure formation

with increasing magnesium oxide content after Soxhlet corrosion study.

a) $Zr_{0.251}Mg_{0.728}U_{0.012}Er_{0.009}O_{1.27}$   b) $Zr_{0.148}Mg_{0.834}U_{0.010}Er_{0.007}O_{1.16}$
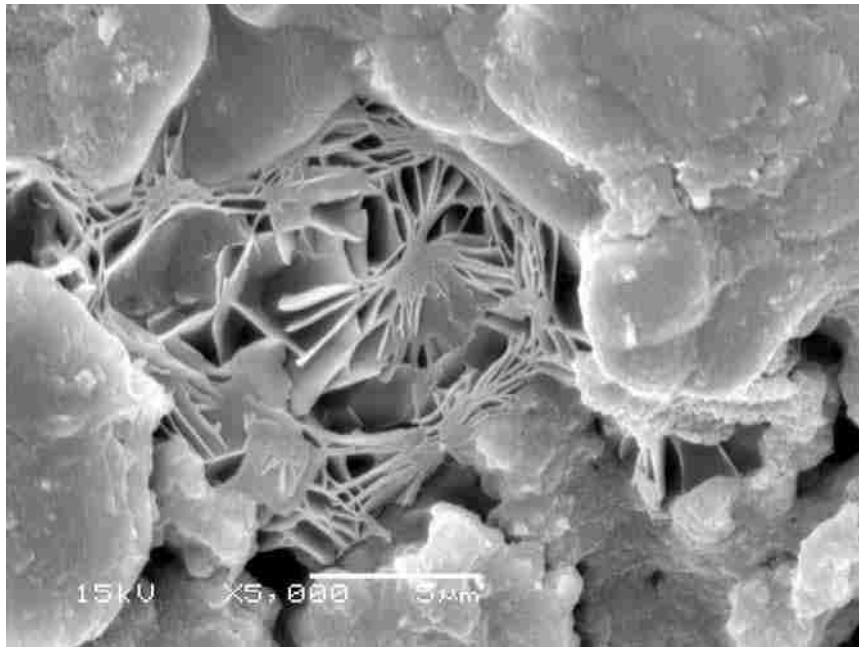


Figure 43: SEM image at 5,000x of $Mg(OH)_2$ plate microstructure formation in pore

space of $Zr_{0.251}Mg_{0.728}U_{0.012}Er_{0.009}O_{1.27}$ after being exposed to deionized

water over 2,000 hours via a Soxhlet apparatus.
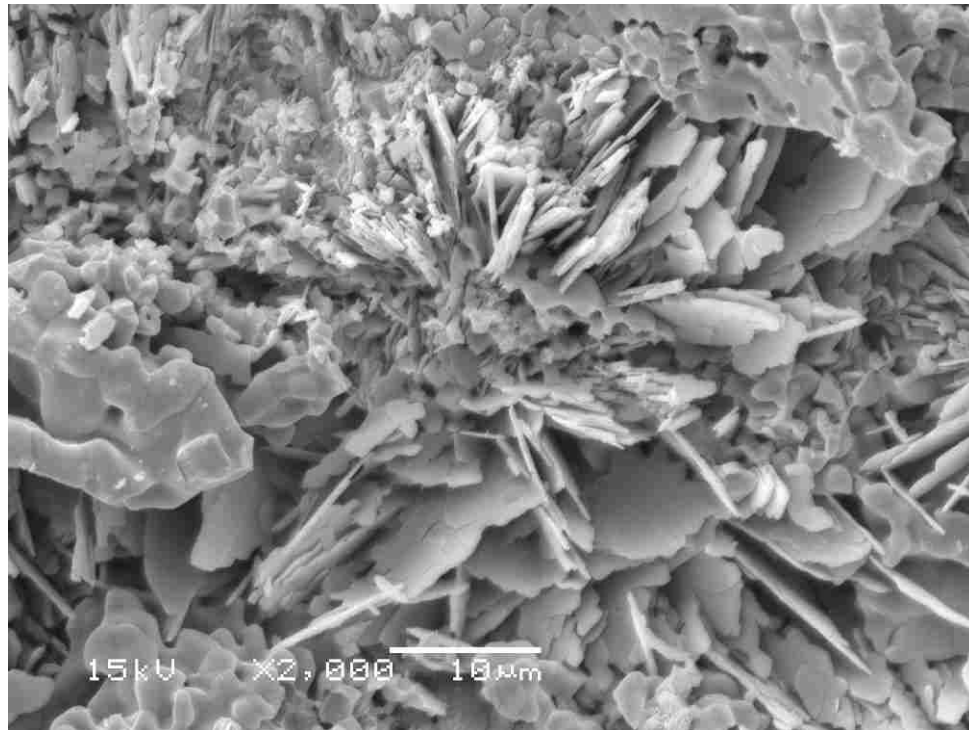
Figure 44: SEM image at 2,000x of $Mg(OH)_2$ plate microstructure formation in cracks of

$Zr_{0.148}Mg_{0.834}U_{0.010}Er_{0.007}O_{1.16}$ after being exposed to deionized water

over 2,000 hours via a Soxhlet apparatus.

The findings of the Soxhlet apparatus study support a preferential dissolution of the magnesium oxide phase (periclase) through hydrolysis to $Mg(OH)_2$ (brucite). Samples with zirconium oxide concentrations above 40 mol. % show corrosion rates of $0.012\pm0.002$ $g/m^2h$. This suggests that the zirconium oxide has a significant stabilizing affect and the corrosion of the magnesium oxide phase is propagated inward from the surface. Samples with zirconium oxide concentrations below 15 mol. % have corrosion rates as high as $0.102\pm0.006$ $g/m^2h$, exhibiting no stabilizing effect. The corrosion of the magnesium oxide is proliferated along grain boundaries, thereby swelling and cracking entire grains out of the matrix. This mechanism was proposed by Medvedev et. al. (53).

Soxhlet corrosion experiments with uranium containing samples were successful in identifying the range of compositions that were dominated by surface corrosion and those compositions that are dominated by the swelling and cracking of material along grain boundaries leading to accelerated corrosion.

4.2.2 Environmental pulse flow dissolution with uranium containing ceramics

An environmental pulse flow dissolution experiment was performed by submerging uranium containing ceramics in deionized water, silicate-bicarbonate solution or brine solution and taking samples periodically to quantify dissolved material. Material from the pulse flow dissolution study was first evaluated visually to determine physical destruction of sample pellets. It was found that higher magnesium oxide concentration leads to more complete destruction of the physical pellet as predicted by the Soxhlet corrosion experiments. This can be best visualized by examining the corrosion of three different compositions that were exposed to the silicate-bicarbonate solution [Figure 45]. Figure 45a has the least amount of magnesium oxide in the sample and shows the least amount of physical damage as can be seen by the pellets remaining whole. Figure 45b has an intermediate magnesium oxide concentration and displays moderate damage in that one pellet is relatively intact while others have been reduced to large pieces. Figure 45c has the highest amount of magnesium oxide in the sample and therefore has the highest physical damage as the pellets have been reduced to pieces ranging in size from powder to cross sections of the pellet.
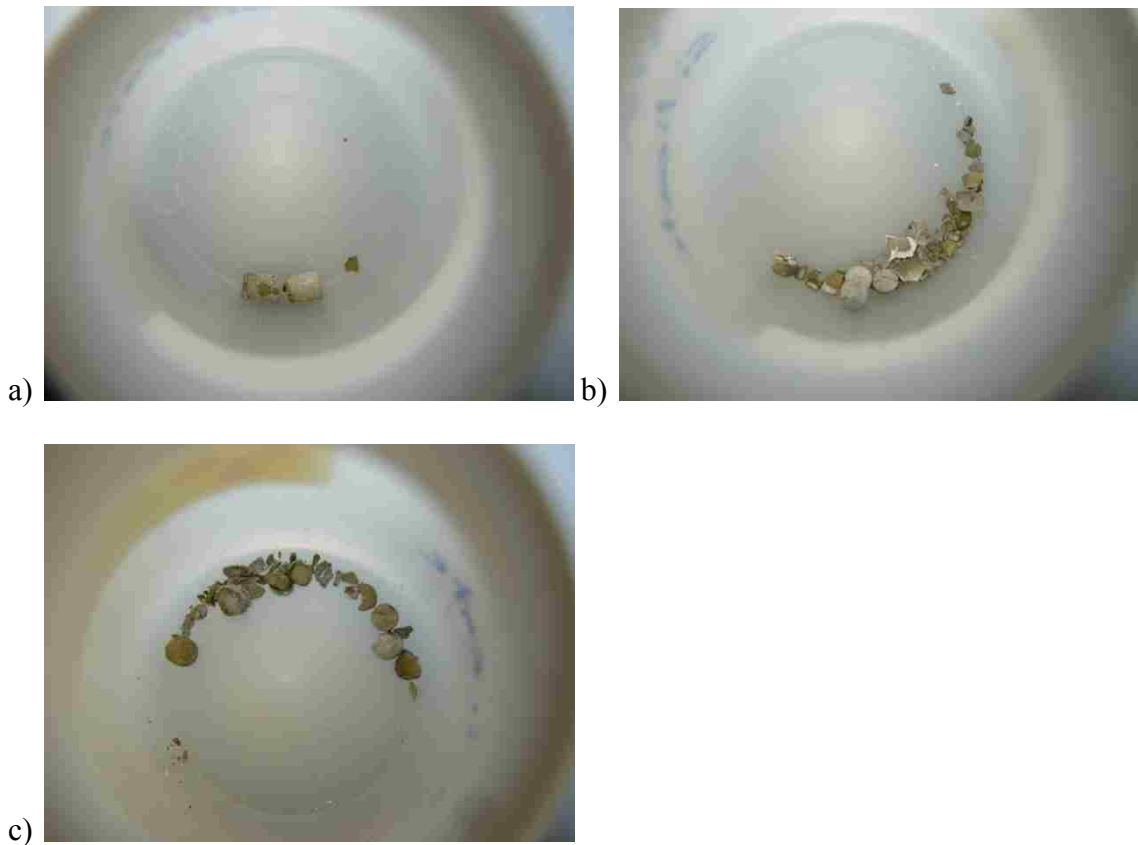
Figure 45: Pictures of zirconia-magnesia inert matrix fuel after pulse flow dissolution study showing increasing damage with increasing magnesium oxide

a) $Zr_{0.395}Mg_{0.580}U_{0.014}Er_{0.010}O_{1.41}$  b) $Zr_{0.251}Mg_{0.728}U_{0.012}Er_{0.009}O_{1.27}$

c) $Zr_{0.148}Mg_{0.834}U_{0.010}Er_{0.007}O_{1.16}$
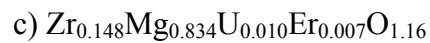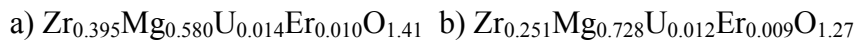
Visual inspection also revealed that brine was the most corrosive solution, followed by deionized water, and lastly silicate-bicarbonate solution. This can be seen in Figure 46, which shows the corrosion of three samples with the same composition in the different solutions. The sample that was immersed in silicate-bicarbonate solution shows little corrosion and a white coating on the surface of the pellet (Figure 46a). Water was corrosive enough to reduce the sample to pieces as seen in Figure 46b. The sample that was in brine (Figure 46c) was reduced to a fine powder.
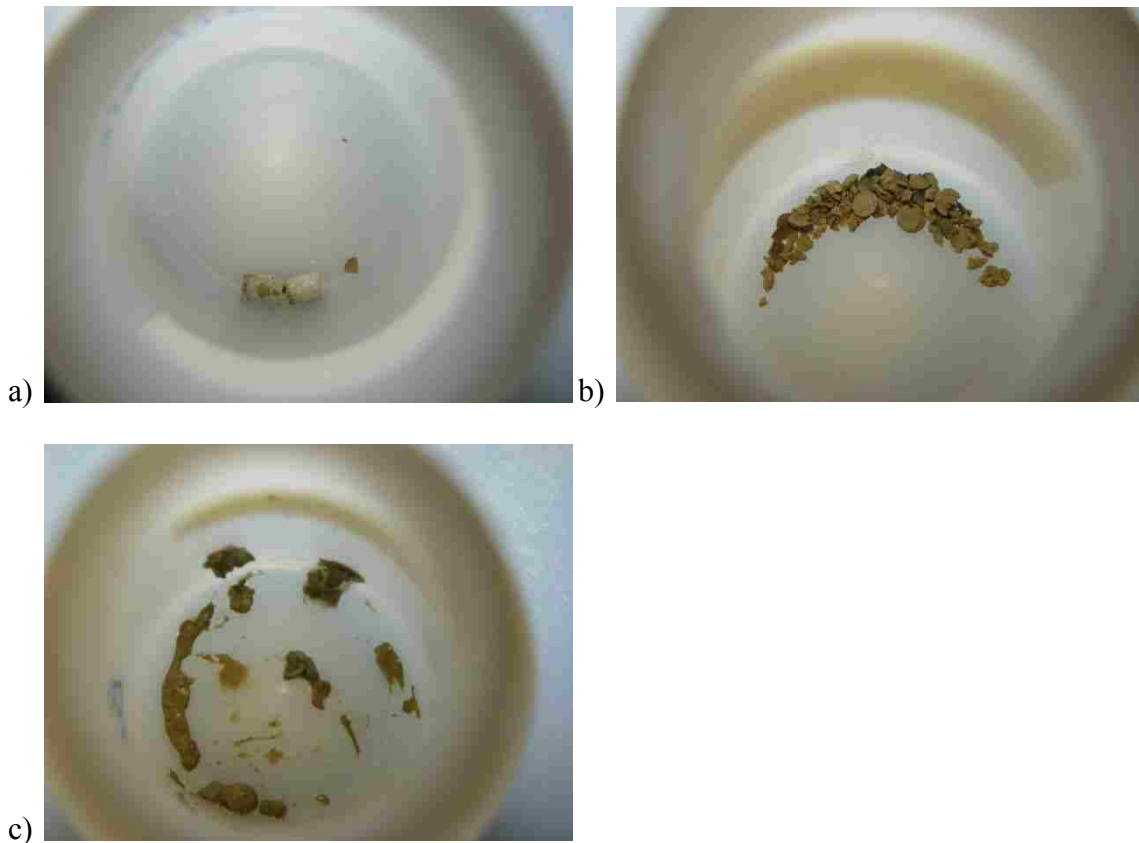
Figure 46: Pictures of $Zr_{0.395}Mg_{0.580}U_{0.014}Er_{0.010}O_{1.41}$ after immersion in three different

solutions at 90 $^o$C for 154 days.  a) silicate-bicarbonate solution

b) deionized water  c) brine

To assess the differences in corrosion products the samples were examined by secondary electron microscopy and x-ray diffraction.  It was evident that corrosion rate and extent was determined by magnesium oxide content and that the hydrolysis of magnesium oxide to magnesium hydroxide was the precursor to dissolution.  In samples with low magnesium oxide concentration in deionized water there was very little evidence of corrosion and the parent cubic phases dominated the surface morphology [Figure 47].  In samples that were immersed in deionized water it was possible to follow
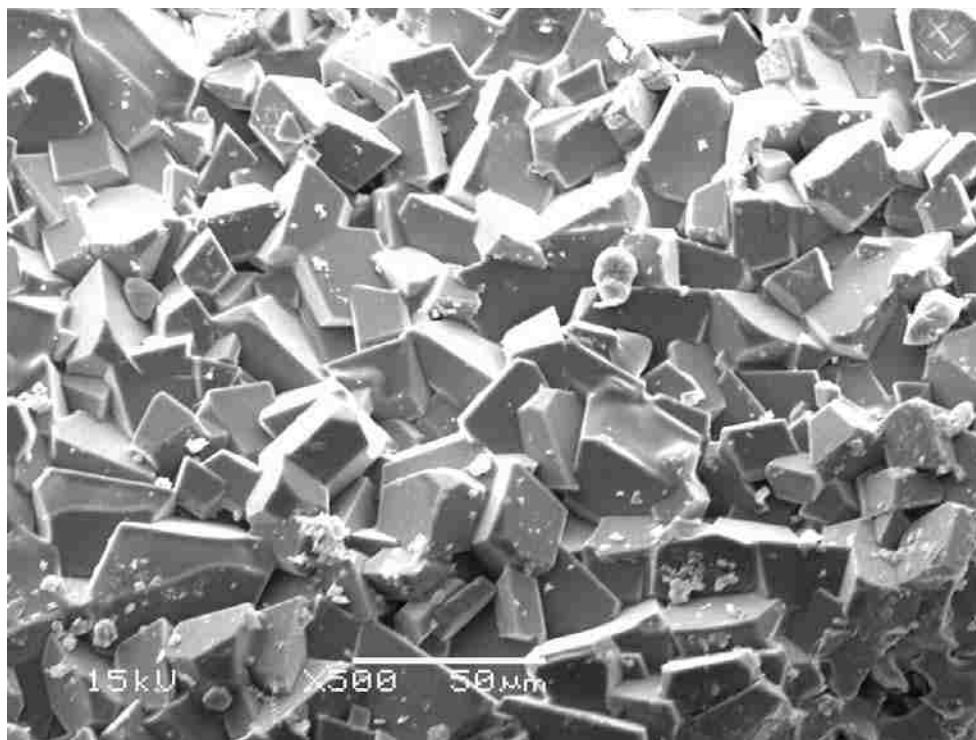
Figure 47: SEM image at 500x magnification of $Zr_{0.395}Mg_{0.580}U_{0.014}Er_{0.010}O_{1.41}$ after

immersion in water at 90 $^o$C for 154 days.  Surface still comprised of parent

cubic phases (zirconia and/or periclase).

the progress of $Mg(OH)_2$ formation over samples with varying magnesium oxide content

[Figure 48].  In a sample with little MgO there are $Mg(OH)_2$ sites starting to nucleate as

shown in Figure 48a.  In Figure 48b it is evident that the higher MgO content has led to a

plate microstructure formation of $Mg(OH)_2$ similar to that observed in the Soxhlet

experiments; however, it is shown here to be on crystal faces and not localized to cracks

and pore space indicating no preference to nucleation sites.  The sample shown in Figure

48c has the highest concentration of MgO and the $Mg(OH)_2$ phase has grown stepwise

[Figure 48d] so that the original plate microstructure has thickened into crystals that

dominate the surface.
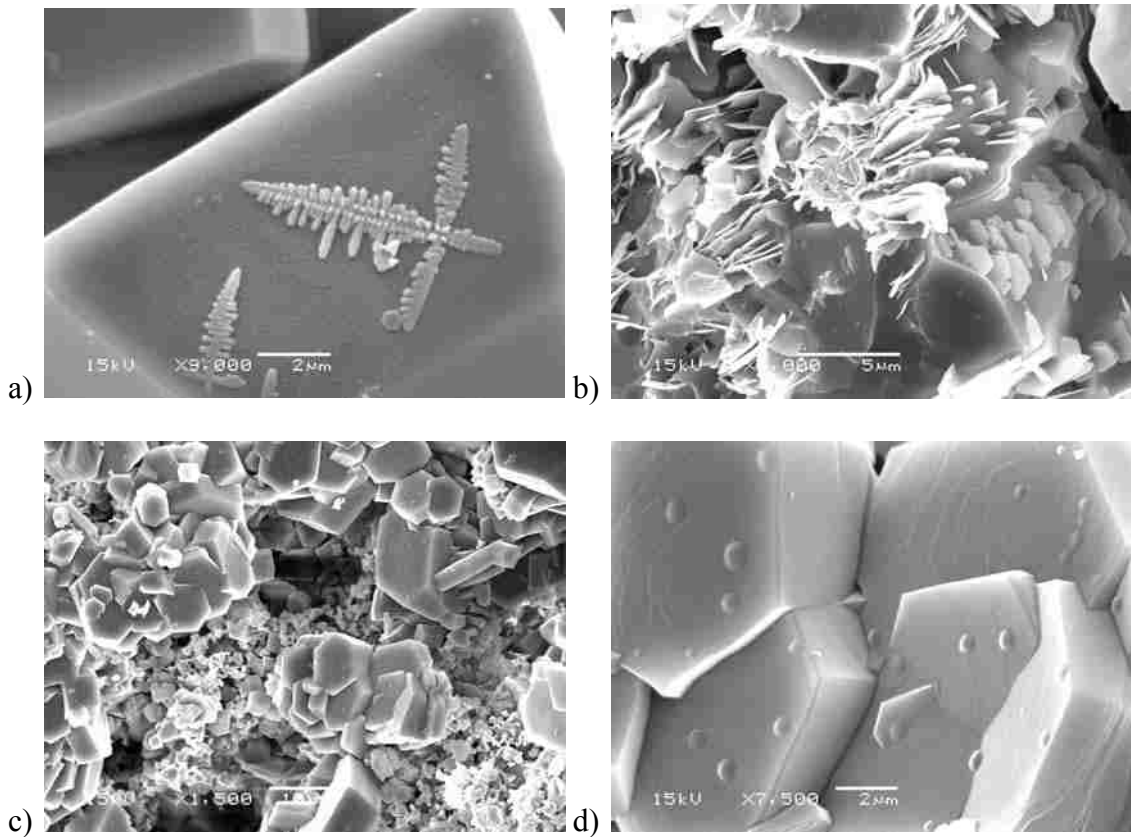
Figure 48: SEM images of samples after pulse flow study in water

a) $Zr_{0.395}Mg_{0.580}U_{0.014}Er_{0.010}O_{1.41}$ with $Mg(OH)_2$ nucleation

b) $Zr_{0.251}Mg_{0.728}U_{0.012}Er_{0.009}O_{1.27}$ with $Mg(OH)_2$ plate microstructure

c) $Zr_{0.148}Mg_{0.834}U_{0.010}Er_{0.007}O_{1.16}$ with $Mg(OH)_2$ crystals

d) $Zr_{0.148}Mg_{0.834}U_{0.010}Er_{0.007}O_{1.16}$ at 7,500x magnification

Brine proved to be the most corrosive of the solutions tested. This was also evident by SEM as the surface was highly irregular and showed a great deal of "pitting" [Figure 49], which is consistent with the corrosion of samples with high concentration of MgO along grain boundaries as proposed by Medvedev et. al.(53). The silicate-bicarbonate solution showed the least amount of corrosion over the samples tested. SEM images demonstrated that a coating was formed on the surface of the pellet that inhibited further

corrosion [Figure 50]. This coating was a product of the silicate in solution reacting with the MgO on the surface to form $H(Mg_2(SO_4))_8$ (olivine), which was identified by x-ray diffraction [Figure 51]. The silicate was not successful in completely prohibiting corrosion at high concentrations of magnesium oxide (> 45 wt. %). At these concentrations $Mg(OH)_2$ was evident on the surface by SEM [Figure 52] and there was little evidence of the olivine on the surface by XRD [Figure 53].
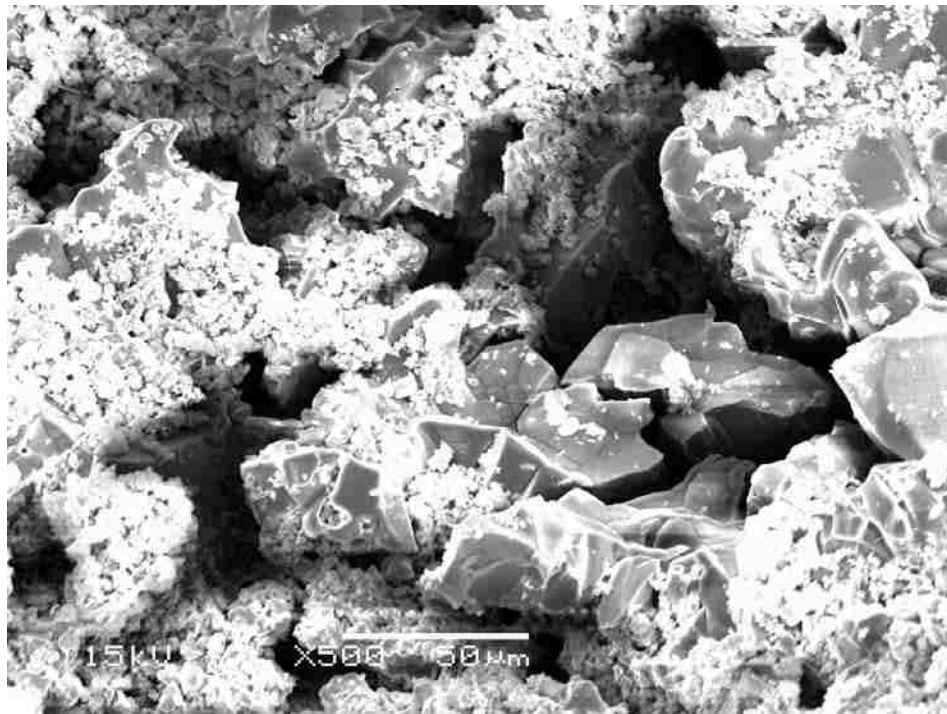


Figure 49: SEM image at 500x magnification of $Zr_{0.148}Mg_{0.834}U_{0.010}Er_{0.007}O_{1.16}$ showing significant corrosion damage and "pitting" after being immersed in brine solution at 90 $^o$C for 154 days.
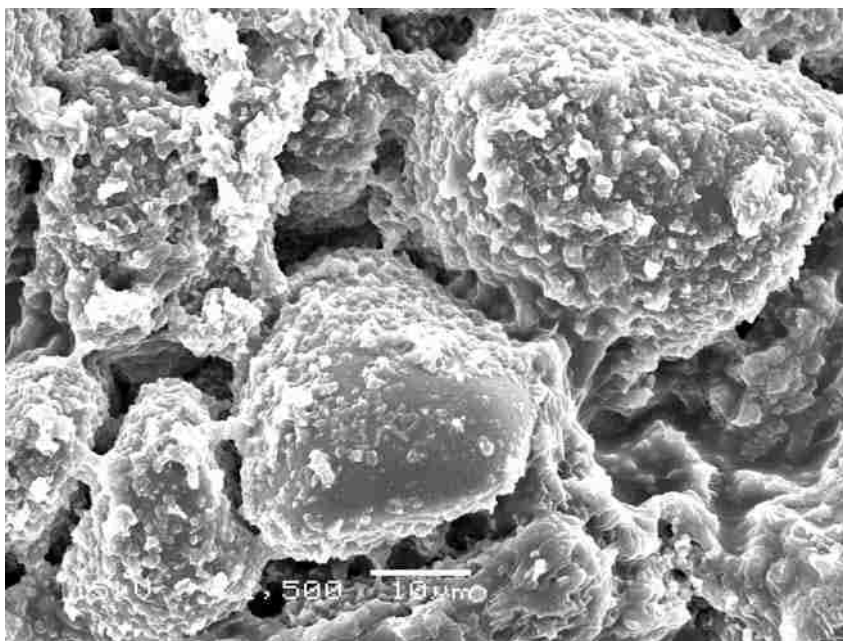
Figure 50: SEM image at 1,500x magnification of $Zr_{0.395}Mg_{0.580}U_{0.014}Er_{0.010}O_{1.41}$ with

coating on surface after being immersed in silicate-bicarbonate solution

at 90 $^o$C for 154 days.
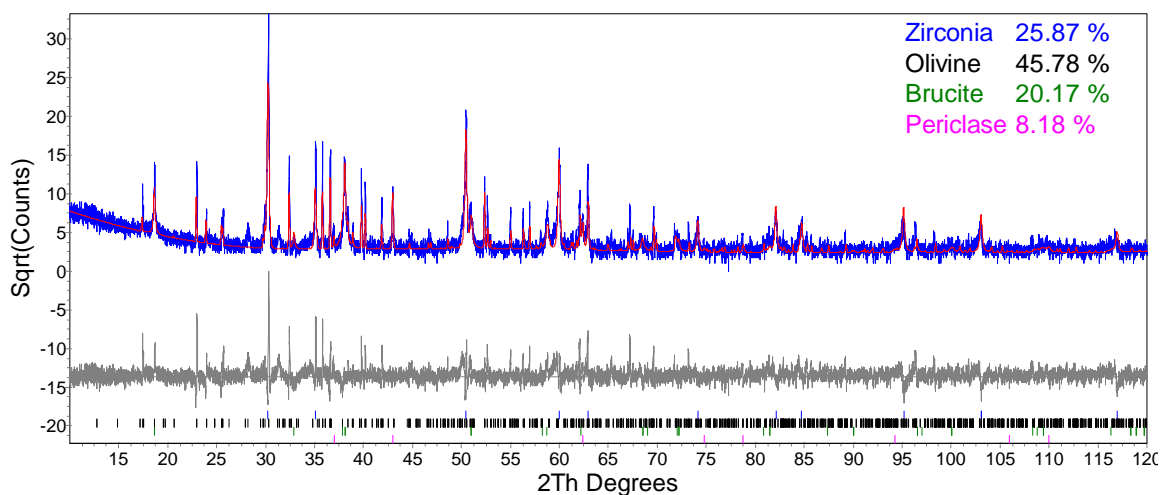


Figure 51: XRD pattern of $Zr_{0.251}Mg_{0.728}U_{0.012}Er_{0.009}O_{1.27}$ (blue) with Rietveld analysis

and least square fit (red) and difference curve (grey) identifying

the dominant surface layer as olivine $(H(Mg_2(SO_4))_8)$.

91
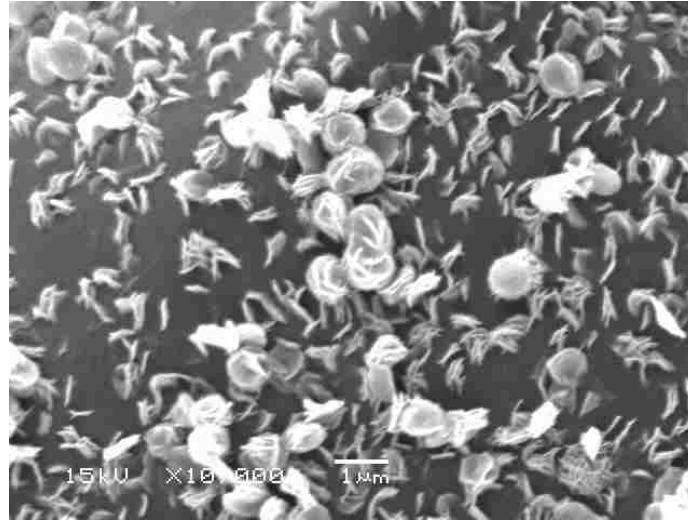
Figure 52: SEM image at 10,000x magnification of $Zr_{0.148}Mg_{0.834}U_{0.010}Er_{0.007}O_{1.16}$ with

$Mg(OH)_2$ growth after being immersed in silicate-bicarbonate solution

at $90^oC$ for 154 days.
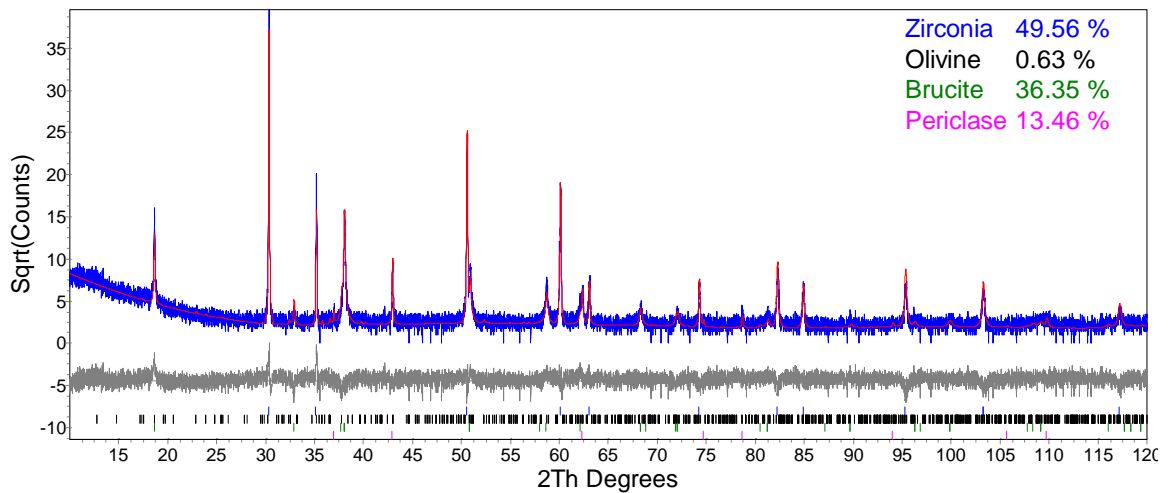


Figure 53: XRD pattern of $Zr_{0.148}Mg_{0.834}U_{0.010}Er_{0.007}O_{1.16}$ (blue) with Rietveld analysis

and least square fit (red) and difference curve (grey) identifying the olivine

$(H(Mg_2(SO_4))_8)$ as a minor phase while brucite $(Mg(OH)_2)$

dominates the magnesium phases.

The solutions used in this experiment were evaluated by inductively coupled plasma – atomic emission spectroscopy. In all samples there was no evidence of any zirconium, uranium, or erbium in solution. The detection limit for these elements was approximately 0.1 mmol/L. This further proves the immobilization of elements within the zirconia and illustrates the corrosion resistance of the this phase. Magnesium was detected in all samples, but kinetics were unreliable due to fluctuations between samples. It was impossible to evaluate in brine due to the high background amount of magnesium in solution.

### 4.2.3 Pressure vessel dissolution of uranium containing ceramic

To test the corrosion of the inert matrix fuel in conditions relevant to a reactor a pressure vessel was used to perform dissolution studies at high temperature and pressure. The pressure vessel was operated for 500 hours for each sample. Samples were placed in a sample cup within the pressure vessel with deionized water. The sample cup was located in the middle of the vessel volume. The vessel was also equipped with a swage lock port for *in situ* sampling and a stirring mechanism. Samples were heated to $300^{o}$C which resulted in pressures of 10.3 MPa. Two samples ($Zr_{0.070}Mg_{0.914}U_{0.009}Er_{0.006}O_{1.08}$ and $Zr_{0.527}Mg_{0.445}U_{0.017}Er_{0.012}O_{1.55}$) were tested over five experiments with similar results. The solution contained a constant level of magnesium after one hour, which was the shortest time before a sample was taken. This amount of magnesium depended on the sample size and volume of water placed in the vessel. It was determined that the magnesium oxide was quickly dissolved to completion due to mechanical corrosion by turbid water. The mechanical destruction of the pellet by turbid water followed by dissolution through the hydrolysis of magnesium oxide proved much faster (< 1 hour)

than suggested previously by studies done in static water at 300$^{o}$C (53). There was no evidence by ICP-AES of zirconium, uranium, or erbium in solution. After the experiment was concluded the vessel was opened and examined. A powder residue was found at the bottom of the vessel that was found to be cubic zirconia by x-ray diffraction. This indicates that although the magnesium oxide phase is destroyed, the zirconia remains unchanged and does not release the fissile material or burnable poison into the simulated coolant. The fuel pellet is however physically destroyed.

4.2.4 Conclusions of aqueous dissolution with uranium containing ceramic

In this study zirconia-magnesia ceramic containing uranium oxide as a fissile component and plutonium oxide homolog and erbium oxide as a burnable poison was examined for corrosion resistance should the fuel be adopted for a "once through" fuel cycle scheme. A Soxhlet corrosion study was performed to quantify the mass loss of the material with different magnesia to zirconia ratios over long periods of time (>2,000 hours). It was found that samples with magnesium oxide content up to 30 wt. % showed minimum corrosion rates due to the stabilizing effect of zirconia. Samples with magnesium oxide content of 60 wt. % or more showed no stabilizing effect from zirconia and had corrosion rates similar to that of samples with an inert matrix of pure magnesium oxide. A moderate magnesium oxide concentration of 45 wt. % displayed an intermediate corrosion rate. It is proposed that the corrosion of samples containing high zirconium oxide concentration is dominated by corrosion along the surface. Higher magnesium oxide concentrations lead to Mg(OH)$_2$ formation along grain boundaries dislodging entire grains leading to accelerated corrosion rates.

A pulse flow dissolution study was conducted with three sample compositions of varying magnesium oxide to zirconium oxide ratios in three solutions (deionized water, silicate-bicarbonate solution, and brine). The samples compositions were chosen based on results from the Soxhlet corrosion study. A sample that exhibited significant corrosion ($Zr_{0.148}Mg_{0.834}U_{0.010}Er_{0.007}O_{1.16}$), moderate corrosion ($Zr_{0.251}Mg_{0.728}U_{0.012}Er_{0.009}O_{1.27}$) and very little corrosion ($Zr_{0.395}Mg_{0.580}U_{0.014}Er_{0.010}O_{1.41}$) via the Soxhlet were selected for the pulse flow dissolution study. There was no evidence of zirconium, uranium, or erbium in solution for any sample by ICP-AES indicating that the cubic zirconia phase remained intact and no cations were leached from the phase. This will immobilize the material even in the event that the pellet is physically destroyed through the corrosion of the magnesia phase. The pellets were physically destroyed to different degrees due to the dissolution of the magnesium oxide phase. Rate and degree of corrosion was found to be proportional to magnesium oxide content, which is consistent with the Soxhlet study. Magnesium oxide hydration and dissolution was monitored by SEM imaging and XRD analysis. Brine was found to be the most corrosive solution followed by deionized water. Silicate-bicarbonate solution was found to be the least corrosive due to the formation of a magnesium silicate on the surface that prohibits further corrosion. This protective layer does not fully prohibit corrosion at magnesium oxide concentrations greater than 45 wt. %. This study confirms the corrosion mechanism proposed by previous studies and expands that knowledge to solutions relevant to environmental conditions. It further quantifies the limits at which zirconia is significantly stabilizing the magnesium oxide to corrosion by water. It was found that the ceramic begins to have significant levels of corrosion above ~60 mol. % MgO.

Pressure vessel dissolution studies have shown that the pellet is physically destroyed through the mechanical destruction and dissolution of the magnesium oxide phase by turbid water at 300$^\mathrm{o}$C and pressures of 10.3 MPa.  This is a significant difference from those studies performed in static water at 300$^\mathrm{o}$C (53).  The zirconia phase remains unchanged and there is no evidence of the release of any uranium or erbium by ICP-AES.

### 4.3 Aqueous dissolution with plutonium containing ceramic

Aqueous studies were performed with plutonium containing samples to evaluate how actual fissile material behaves within the inert matrix.  Because the inert matrix has been well characterized by previous studies using uranium and cerium, studies with plutonium only quantified the amount of plutonium in solution to evaluate its behavior.  The environmental pulse flow dissolution study was performed to evaluate the material as a waste form in a "once through" fuel cycle.  The material was also tested under reactor coolant conditions (high temperature, high pressure water) with the aid of a pressure vessel.

### 4.3.1 Environmental pulse flow study with plutonium containing ceramic

The environmental pulse flow dissolution study was carried out with plutonium containing inert matrix fuel over 1,000 hours in deionized water at 90$^\mathrm{o}$C.  Three compositions were tested including $Zr_{0.64}Mg_{0.29}Pu_{0.029}Er_{0.041}O_{1.7}$, $Zr_{0.56}Mg_{0.36}Pu_{0.037}Er_{0.044}O_{1.6}$, and $Zr_{0.44}Mg_{0.47}Pu_{0.042}Er_{0.048}O_{1.5}$.  Samples were taken from the water and analyzed by liquid scintillation counting.  The samples did not contain any activity above background (0.1 Bq).  Assuming a detection limit of twice the background, the amount of plutonium released was less than 0.01 wt. % of the plutonium for each

sample. This confirms that there is no corrosion of the zirconia phase and that no fissile material is released under these conditions.

Upon physical inspection there was no difference in the samples from their original condition. To assess any changes in microstructure the samples were also analyzed by secondary electron microscopy. It was found that there was virtually no change in the appearance of the microstructure in the samples. The sample with the least amount of magnesium oxide ($Zr_{0.44}Mg_{0.47}Pu_{0.042}Er_{0.048}O_{1.5}$) was polished for electronprobe microanalysis in a previous study. It is still evident that there is no corrosion damage at the surface [Figure 54] even on areas of magnesium oxide [Figure 55]. A sample with slightly higher magnesium oxide ($Zr_{0.56}Mg_{0.36}Pu_{0.037}Er_{0.044}O_{1.6}$) that did not have a polished surface also shows no change in microstructure on the surface of the pellet after exposure to 90 $^{o}$C water over 1,000 hours as seen in Figure 56.



a)   b)
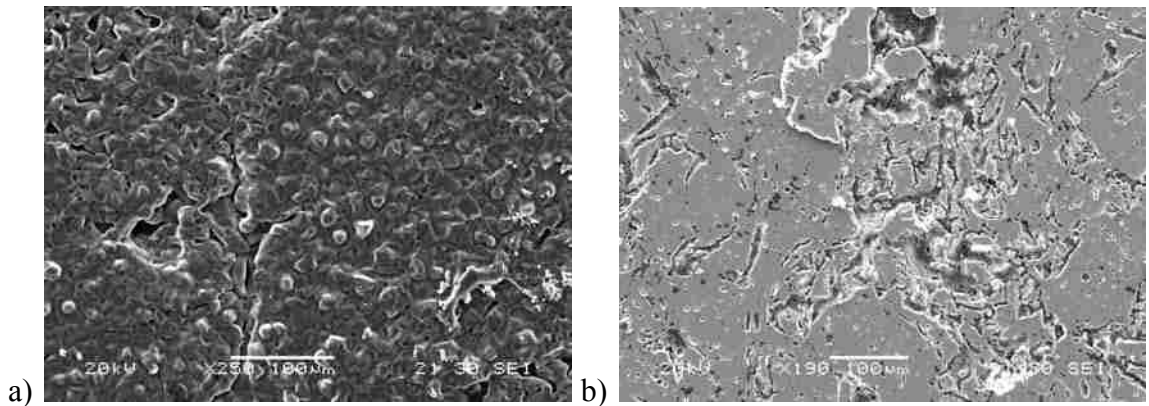
Figure 54: SEM image of $Zr_{0.44}Mg_{0.47}Pu_{0.042}Er_{0.048}O_{1.5}$ a) without exposure to water

b) after pulse flow dissolution study.
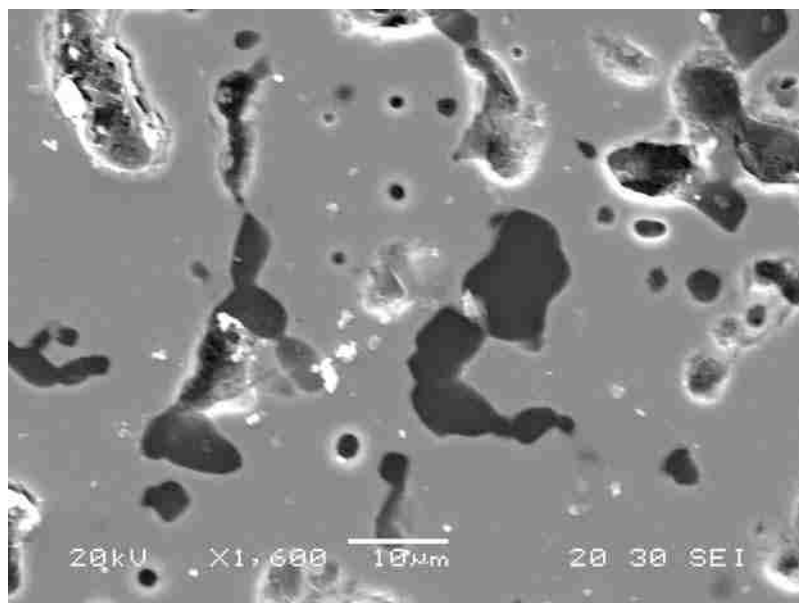
Figure 55: SEM image of $Zr_{0.44}Mg_{0.47}Pu_{0.042}Er_{0.048}O_{1.5}$ at 600x with magnesium oxide

phase (dark) and zirconia (light) after dissolution study.



a)                                             b)
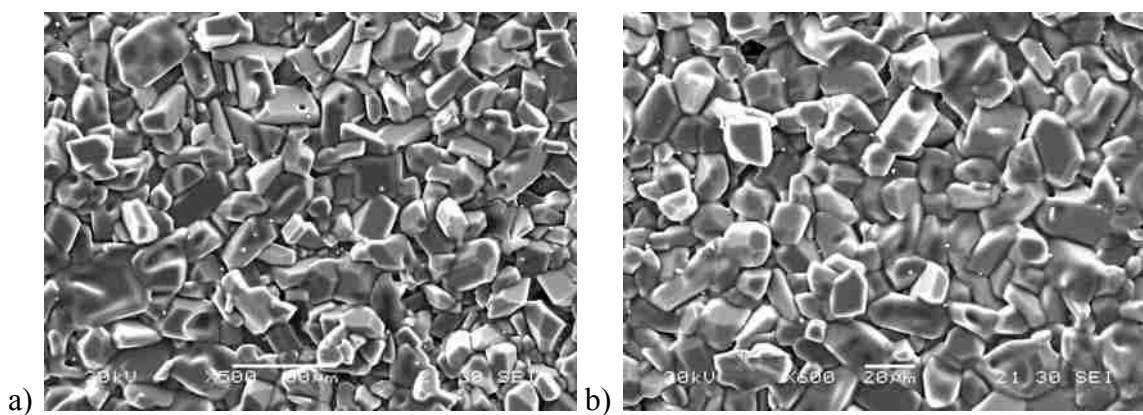
Figure 56: SEM image of $Zr_{0.56}Mg_{0.36}Pu_{0.037}Er_{0.044}O_{1.6}$ a) without exposure to water

b) after pulse flow experiment

The sample with the highest amount of magnesium oxide ($Zr_{0.44}Mg_{0.47}Pu_{0.042}Er_{0.048}O_{1.5}$)

shows similar behavior even though it is now obvious that there is a dominant amount of

magnesium oxide.  The sample unexposed to water is identical to that sample that was in

the pulse flow dissolution study [Figure 57].   Even at high magnification there is no

discernable difference between the samples [Figure 58].
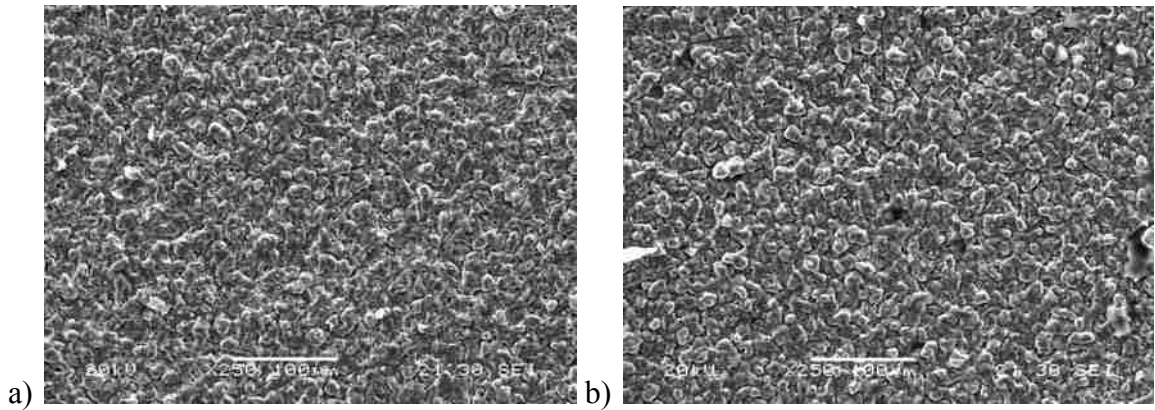


Figure 57: SEM image of $Zr_{0.44}Mg_{0.47}Pu_{0.042}Er_{0.048}O_{1.5}$ a) without exposure to water

b) after pulse flow dissolution study at 250x magnification
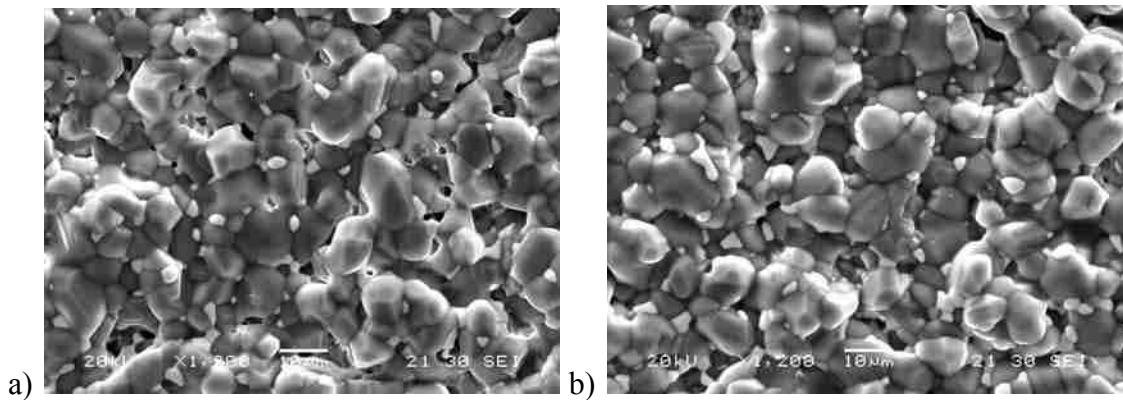


Figure 58: SEM image of $Zr_{0.44}Mg_{0.47}Pu_{0.042}Er_{0.048}O_{1.5}$ a) without exposure to water

b) after pulse flow dissolution study at 1,200x magnification

After SEM imaging, the sample $Zr_{0.44}Mg_{0.47}Pu_{0.042}Er_{0.048}O_{1.5}$ was evaluated by x-ray

diffraction to assess any changes in the phases.   This sample was chosen because it had

the highest magnesium oxide content and was therefore the most likely to undergo

corrosion damage and phase changes. It was shown that the x-ray diffraction pattern was almost identical to the one taken before the dissolution study [Figure 59]. There was a minor decrease in periclase (MgO phase) from 17.8 to 13.6 wt. % which could be due to partial dissolution. It could also be due to inhomogeneity within the sample as only 5 mg samples are used for x-ray diffraction analysis.
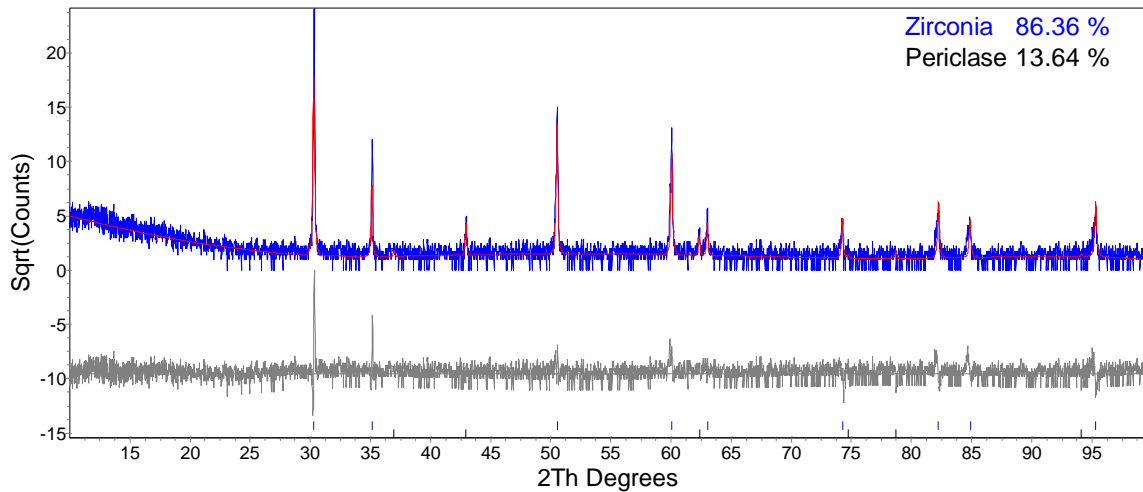


Figure 59: X-ray diffraction pattern of $Zr_{0.44}Mg_{0.47}Pu_{0.042}Er_{0.048}O_{1.5}$ (blue) with fit (red) and difference curve (grey) after dissolution study.

### 4.3.2 Pressure vessel dissolution of plutonium containing ceramic

A pressure vessel containing a sample with the composition $Zr_{0.76}Mg_{0.10}Pu_{0.078}Er_{0.062}O_{1.9}$ was filled with deionized water and heated to 300$^{o}$C to simulate corrosion conditions by coolant water in the event of a cladding failure. This study differed from the previous pressure vessel studies in that there was no stirring or *in situ* sampling. Without the mechanical corrosion of turbid water the pellet remained intact. There was no visual evidence of corrosion. The water was analyzed by

scintillation counting at 150 hours and at 300 hours and was found both times to contain

less than 0.8 wt. % of the total plutonium within the pellet. This indicates that there was

very little release of plutonium from the matrix. Some of the plutonium at the surface

was leached into the solution, because the activity was non-zero, but this small quantity

of activity was released and did not increase after it was detected. The pellet was

analyzed for changes in microstructure by secondary electron microscopy and was found

to have very little damage on the surface [Figure 60]. The surface was polished before

the sample was exposed to the dissolution experiment. There is no evidence of any

corrosion even at high magnification [Figure 61]. This experiment confirms previous

studies under static reactor conditions by Medvedev et. al. (53).
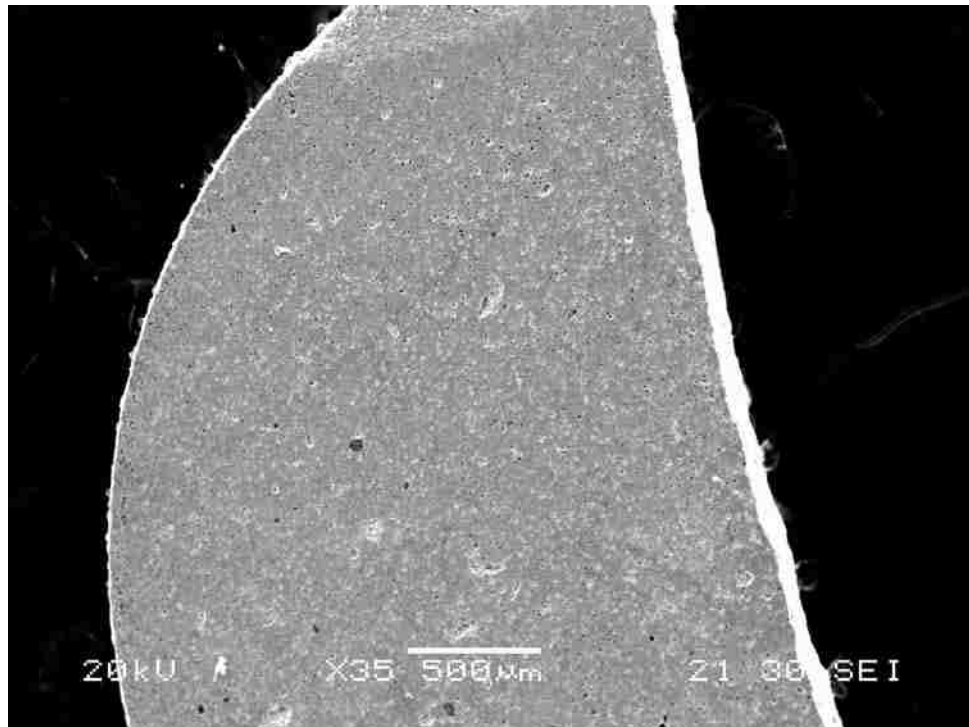


Figure 60: SEM image of $Zr_{0.76}Mg_{0.10}Pu_{0.078}Er_{0.062}O_{1.9}$ after pressure vessel disolution

experiment at 35x magnification
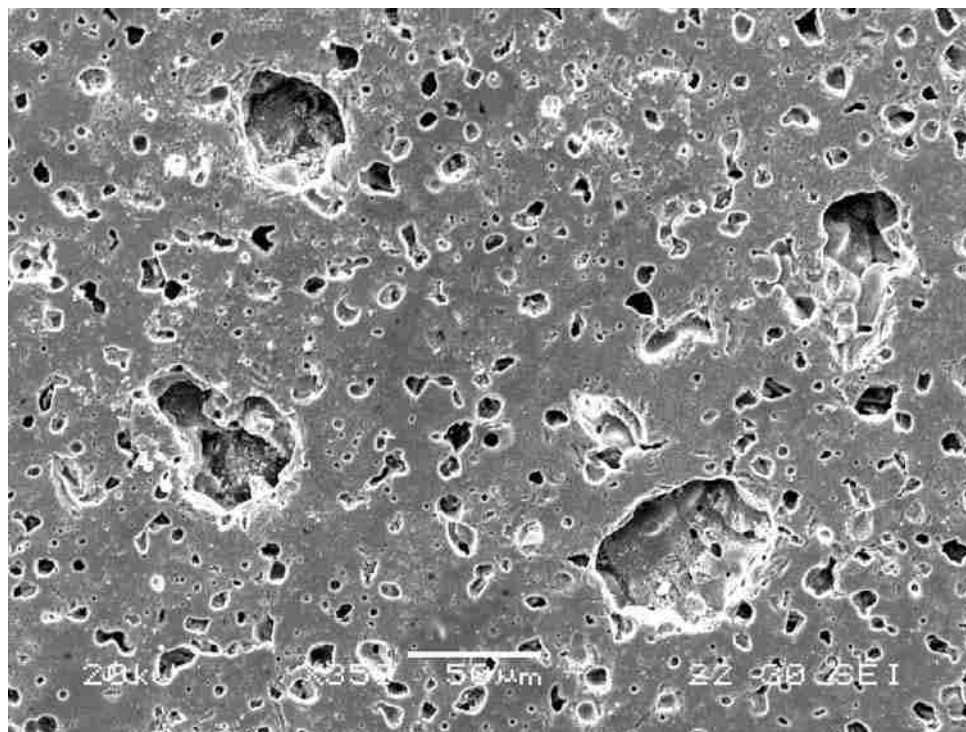
Figure 61: SEM image of $Zr_{0.76}Mg_{0.10}Pu_{0.078}Er_{0.062}O_{1.9}$ after pressure vessel dissolution experiment at 350x magnification

4.3.3 Conclusions of aqueous dissolution with plutonium containing inert matrix fuels

The goal of the aqueous dissolution studies with plutonium was to evaluate inert matrix fuel containing actual fissile material and burnable poison in reactor and repository conditions. The inert matrix dissolution was well characterized by dissolution studies with uranium. The advantage of plutonium is its relatively high specific activity that can be used to significantly lower the detection limit of the material by liquid scintillation counting when compared to ICP-AES. Even with this lower detection limit it was found that less than 0.8 wt. % of the plutonium is released in static $300^{o}C$ water. This study also confirmed previous studies on pellet integrity under these conditions and validates the differences found between static and turbid water corrosion properties. As

a waste form zirconia does not appear to have any corrosion at all within the scope of this study.  The release of plutonium in waste form dissolution studies was found to be less than 0.01 wt. %, which is the detection limit under these experimental conditions.  This material performs extremely well under aqueous dissolution and proves to be a robust material under both reactor and repository conditions.

## 4.4 Conclusions of aqueous dissolution studies

Aqueous dissolution studies were performed with cerium oxide containing inert matrix ceramic in order to establish protocols and validate procedures with non-radioactive material.  These studies have also been used to assess the effectiveness of cerium as a plutonium homolog both structurally and chemically.  Soxhlet corrosion studies with cerium and uranium have found that zirconia is a highly resilient material that does not dissolve or release material incorporated into its matrix in aqueous media as tested in these experiments.  Samples with magnesium oxide content of 60 wt. % or more showed no stabilizing effect from zirconia and had corrosion rates similar to that of samples with an inert matrix of pure magnesium oxide.  A moderate magnesium oxide concentration of 45 wt. % displayed an intermediate corrosion rate.  It is proposed that the corrosion of samples containing high zirconium oxide concentration is dominated by corrosion along the surface.  Higher magnesium oxide concentrations lead to $Mg(OH)_2$ formation along grain boundaries dislodging entire grains leading to accelerated corrosion rates.

A pulse flow dissolution study was conducted with three sample compositions of varying magnesium oxide to zirconium oxide ratios in three solutions (deionized water,

silicate-bicarbonate solution, and brine).  There was no evidence of zirconium, uranium, plutonium or erbium in solution for any sample by ICP-AES indicating that the cubic zirconia phase remained intact and no cations were leached from the phase.  This will immobilize the material even in the event that the pellet is physically destroyed through the corrosion of the magnesia phase.  The pellets were physically destroyed to different degrees due to the dissolution of the magnesium oxide phase.  Rate and degree of corrosion was found to be proportional to magnesium oxide content, which is consistent with the Soxhlet study.  Magnesium oxide hydration and dissolution was followed by SEM imaging and XRD analysis.  Brine was found to be the most corrosive solution followed by deionized water.  Silicate-bicarbonate solution was found to be the least corrosive due to the formation of a magnesium silicate on the surface that prohibits further corrosion.  This protective layer does not fully prohibit corrosion at magnesium oxide concentrations greater than 45 wt. %.  This study confirms the corrosion mechanism proposed by previous studies and expands that knowledge to solutions relevant to environmental conditions.  It further quantifies the limits at which zirconia is significantly stabilizing the magnesium oxide to corrosion by water.

Experiments were performed to simulate dissolution under reactor conditions in the event of a cladding failure.  These experiments performed with turbid water at $300^{o}C$ found that the fuel pellet was physically destroyed within 48 hours, but there was no evidence of dissolution of the zirconia phase or any of its components for up to 250 hours.  Due to a far lower detection limit, plutonium was found at less than 0.8 wt. % released in static $300^{o}C$ water.  This small amount of plutonium, probably at the surface, was initially released and no further dissolution was evident.  Studies performed in static

conditions also confirmed previous studies on pellet integrity under these conditions and

validates the differences found between static and turbid water corrosion properties.

CHAPTER 5


ACIDIC DISSOLUTION STUDIES

5.1 Acidic dissolution with cerium containing ceramic

5.1.1 Nitric acid dissolution with cerium containing ceramic

To determine the solubility of the ceramic in nitric acid, a round bottom flask containing 16 M $HNO_3$ with a reflux condenser was placed in a heating mantle and samples were introduced in the flask with a measured amount of acid and boiled. The first studies were done with cerium containing ceramics so that the method could be developed without the additional complication of radioactive material. These studies also assess the applicability of using cerium as a homolog for the actinides. Samples were analyzed by visual inspection and the concentration of material in solution was quantified by inert coupled plasma – atomic emission spectroscopy (ICP-AES).

A 200 mg sample of $Zr_{0.866}Mg_{0.093}Ce_{0.026}Er_{0.014}O_{1.90}$ was placed in 11.3 M nitric acid and boiled at ~125 $^{o}$C for three hours. No visible signs of dissolution were present on the pellet. It remained whole and displayed no change on the surface. Because of this, the pellet was ground to a powder, placed in concentrated (15.7 M) nitric acid and boiled at ~120 $^{o}$C for two additional hours. At this point the heat was removed and the powdered sample was allowed to sit in the nitric acid for four days. The solution was then heated and the sample boiled for an additional 8 hours. In total the sample was in nitric acid for 6 days, 13 hours of which it was boiling. There was no physical change in the powder. It should be noted that this sample did not contain a magnesia phase which is known to be soluble in nitric acid. This study was aimed at exploring the solubility of the zirconia

phase. A sample of the solution was diluted to 5 vol. % acid and analyzed by ICP-AES. It was determined that all species (zirconium, magnesium, cerium, and erbium) were below the detection limit which is nominally 10 ppm for the ICP-AES under these conditions. This study verified our experimental set up and method with non-radioactive material. It also proved that zirconia with this composition is insoluble in high concentrations of nitric acid within the time and detection limit of the current experiment.

### 5.1.2 Sulfuric acid dissolution with cerium containing ceramic

As an alternative to the nitric acid dissolution, sulfuric acid was also explored as a means of dissolving the ceramic. These studies were performed in the same way as the nitric acid dissolution studies with the exception of temperature. Sulfuric acid dissolution was performed at the boiling point of concentrated sulfuric acid, which is 290 $^{\circ}$C as compared to the much lower boiling point of nitric acid at 120 $^{\circ}$C. This study was to serve as the validation of method and yield information on the accuracy of cerium as a homolog for the actinides.

A pellet of $Zr_{0.771}Mg_{0.188}Ce_{0.026}Er_{0.014}O_{1.80}$ was ground to a powder and 1.8087 g of it was placed in a round bottom flask with 150 mL of concentrated sulfuric acid. The solution was brought to a boil and allowed to proceed for 48 hours. At that time there was some residue in the bottom of the flask that appeared to be slightly less than the starting material. A sample of the solution was taken periodically throughout the dissolution to assess the kinetics. The concentrations determined by ICP-AES were normalized by the surface area of the sample as determined by gas sorption.

It was determined that $Zr_{0.771}Mg_{0.188}Ce_{0.026}Er_{0.014}O_{1.80}$ is at least partially soluble in sulfuric acid. Concentrations of all four elements were found in solution to different

degrees. Zirconium was found at the highest concentrations, which is not surprising considering it is the major component in the sample. Cerium and erbium seem to follow first order kinetics as can be seen in Figure 62. It is unclear as to the kinetics of zirconium dissolution, because of its low solubility but it is compared to first order kinetics in Figure 63. Magnesium increases sporadically and is therefore not fit to any kinetics equation [Figure 63].



| $y = m1*(1-exp(-m2 * M0))$ | | |
| --- | --- | --- |
| | Value | Error |
| m1 | 3.9496 | 0.15445 |
| m2 | 0.1601 | 0.022276 |
| Chisq | 0.078683 | NA |
| R | 0.99356 | NA |

| $y = m1*(1-exp(-m2 * M0))$ | | |
| --- | --- | --- |
| | Value | Error |
| m1 | 5.6559 | 0.20973 |
| m2 | 0.19395 | 0.025277 |
| Chisq | 0.15915 | NA |
| R | 0.99256 | NA |
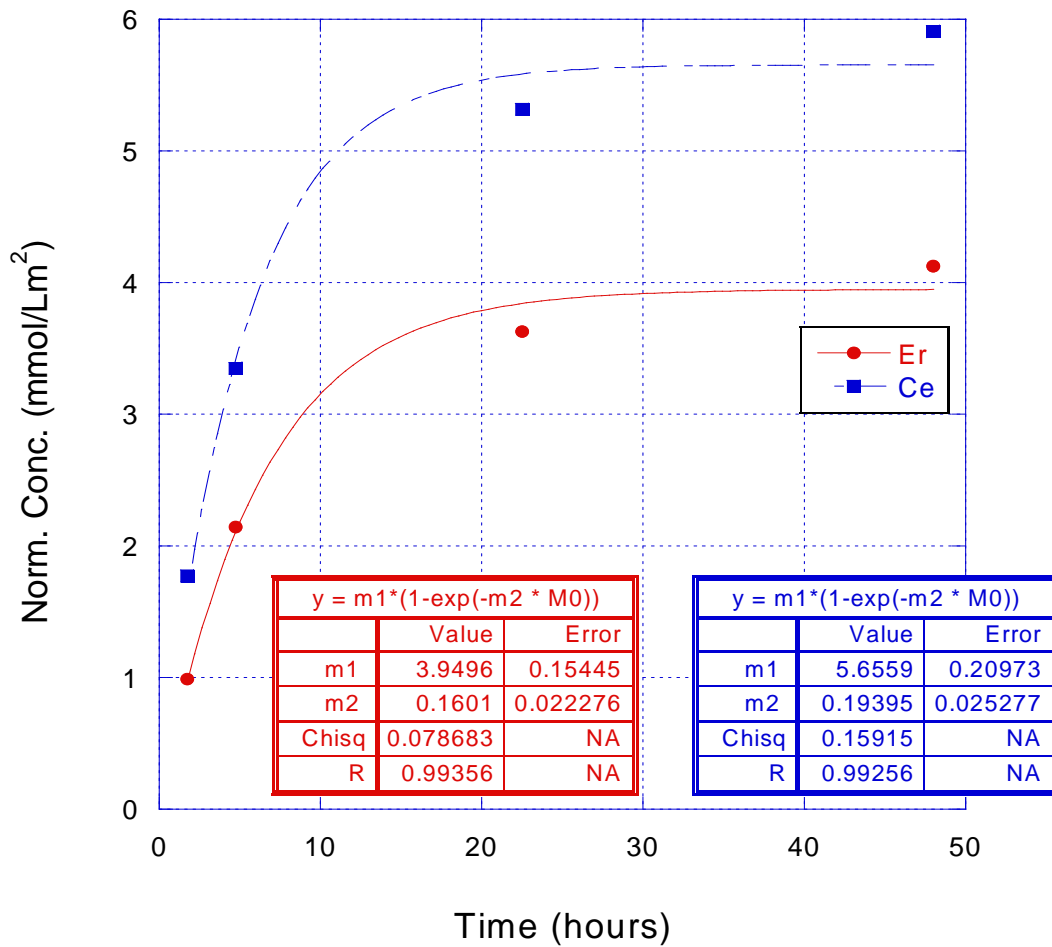
Figure 62: Cerium and erbium dissolution in sulfuric acid from $Zr_{0.771}Mg_{0.188}Ce_{0.026}Er_{0.014}O_{1.80}$ with first order kinetics fit.
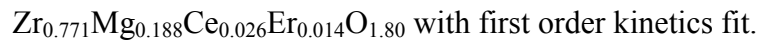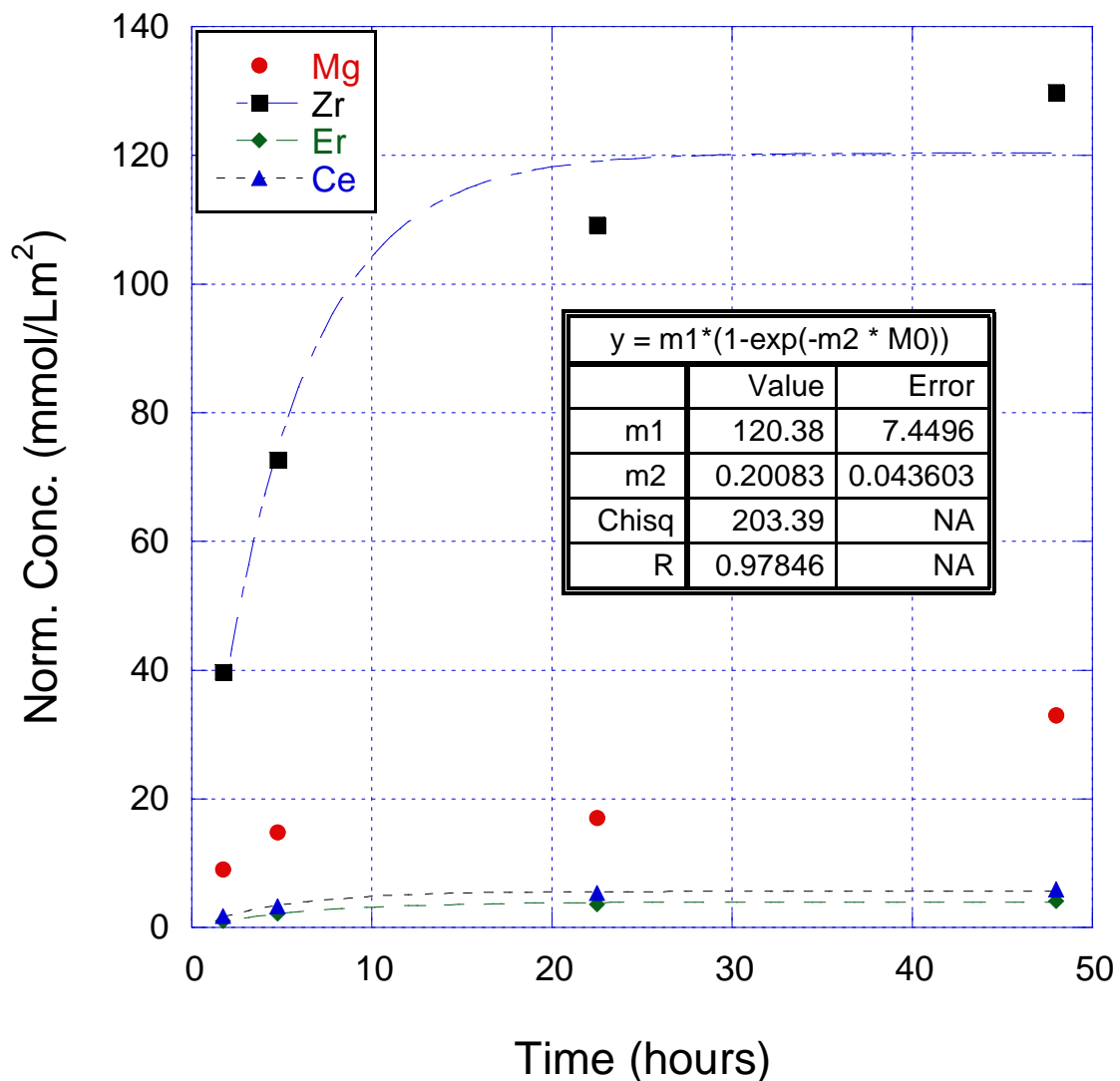
Figure 63: Dissolution in sulfuric acid of $Zr_{0.771}Mg_{0.188}Ce_{0.026}Er_{0.014}O_{1.80}$

with first order kinetics fit of zirconium.

The kinetics constants for zirconium and cerium are $0.20\pm0.044$ and $0.19\pm0.025$ $hrs^{-1}$ respectively, but erbium is $0.16\pm0.022$ $hrs^{-1}$ and magnesium does not seem to follow first order kinetics suggesting that this may be an incongruent dissolution. These experiments will be repeated with actinides to better establish the dissolution kinetics of the system. These experiments were successful in establishing the method for sulfuric acid

dissolution and suggest that it is possible to partially dissolve the zirconia phase in concentrated sulfuric acid. It was also suggested that cerium and erbium follow first order kinetics.

### 5.1.3 Conclusions of acidic dissolution with cerium containing inert matrix fuel

The main focus of dissolution studies with cerium was to use it as a non-radioactive homolog for actinides within the inert matrix fuel and to establish methods and protocols that would be applied to studies with actinides. This proved to be invaluable in establishing procedures. The second goal of these studies was to evaluate the effectiveness of cerium as a homolog for uranium and plutonium. It was established in this study that cerium containing zirconia is insoluble in high concentrations of nitric acid. It proved to be somewhat soluble in sulfuric acid. Cerium and erbium follow first order kinetics in sulfuric acid. The kinetics of zirconium and magnesium were not determined. Also, the ceramic was not completely dissolved and a large amount of solid residue remained after 48 hours in the sulfuric system. These studies are performed in greater detail with uranium to evaluate the solubility of the material in various acids.

### 5.2 Acidic dissolution with uranium containing ceramic

### 5.2.1 Nitric acid dissolution with uranium containing ceramic

Several sample compositions containing uranium were examined for nitric acid solubility. Samples were crushed to a coarse powder and the surface area of the powder was measured before being added to the flask. Concentrated nitric acid (16M) was used for all studies. All magnesium oxide was dissolved in less than one hour under current experimental conditions. Two of those sample compositions

($Zr_{0.148}Mg_{0.834}U_{0.010}Er_{0.007}O_{1.16}$ and $Zr_{0.070}Mg_{0.914}U_{0.009}Er_{0.006}O_{1.08}$) showed solubility of species other than magnesium. It was found that at these extremely high levels of magnesium oxide there are two advantages that allow for the dissolution of uranium. The first is that since the zirconia is the minor phase it has a large surface area to volume ratio after the magnesium oxide is dissolved, which will enhance the kinetics. The second advantage is that since all of the uranium is concentrated within this zirconia phase the less zirconium oxide in the sample the more concentrated the uranium within that phase. Because of this, it was observed that there is zirconium, uranium, and erbium in solution by ICP-AES. This is a substantial difference from those studies done in the absence of a fissile material or with cerium oxide as a fissile material homolog.

The sample with the highest amount of magnesium oxide, $Zr_{0.070}Mg_{0.914}U_{0.009}Er_{0.006}O_{1.08}$, shows the most material in solution. As can be seen in Figure 64, the amount of material going into solution over time follows linear kinetics without any indication of equilibrium. This same behavior can be seen in sample $Zr_{0.148}Mg_{0.834}U_{0.010}Er_{0.007}O_{1.16}$ although less material is being dissolved for the same period of time [Figure 65]. In both samples there seems to be a slower rate for the first 100 hours than there is afterward. This initial lag in kinetics could be due to a number of factors such as an initial leaching of magnesium from the zirconia, the formation of nitrous acid, kinetics of oxidation within the lattice, etc. For this reason kinetics were determined from concentrations taken after 100 hours. It was determined that the fastest rate of uranium dissolution, which was in sample $Zr_{0.070}Mg_{0.914}U_{0.009}Er_{0.006}O_{1.08}$, was $3.0 \pm 0.25$ µmol/L•$m^2$•h [Figure 66]. When the zirconium oxide content was increased from

Figure 64: Surface area normalized concentrations of $Zr_{0.070}Mg_{0.914}U_{0.009}Er_{0.006}O_{1.08}$ in concentrated nitric acid. Error bars represent standard deviation of three samples.



Figure 65: Surface area normalized concentrations of $Zr_{0.148}Mg_{0.834}U_{0.010}Er_{0.007}O_{1.16}$ in concentrated nitric acid. Error bars represent standard deviation of three samples.
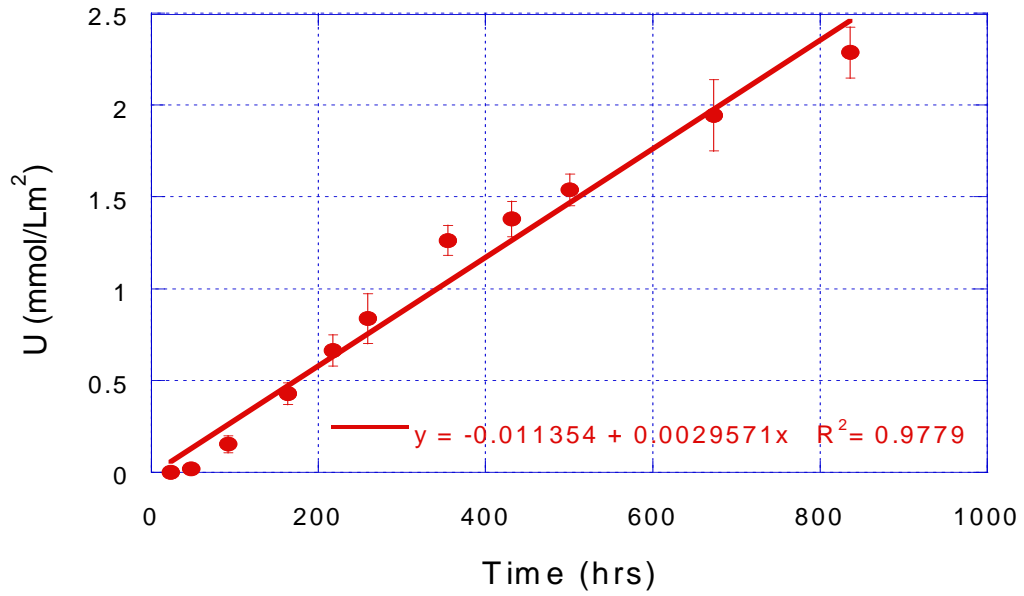
Figure 66: Uranium concentration with rate of $Zr_{0.070}Mg_{0.914}U_{0.009}Er_{0.006}O_{1.08}$ in concentrated nitric acid. Error bars represent standard deviation of three samples.
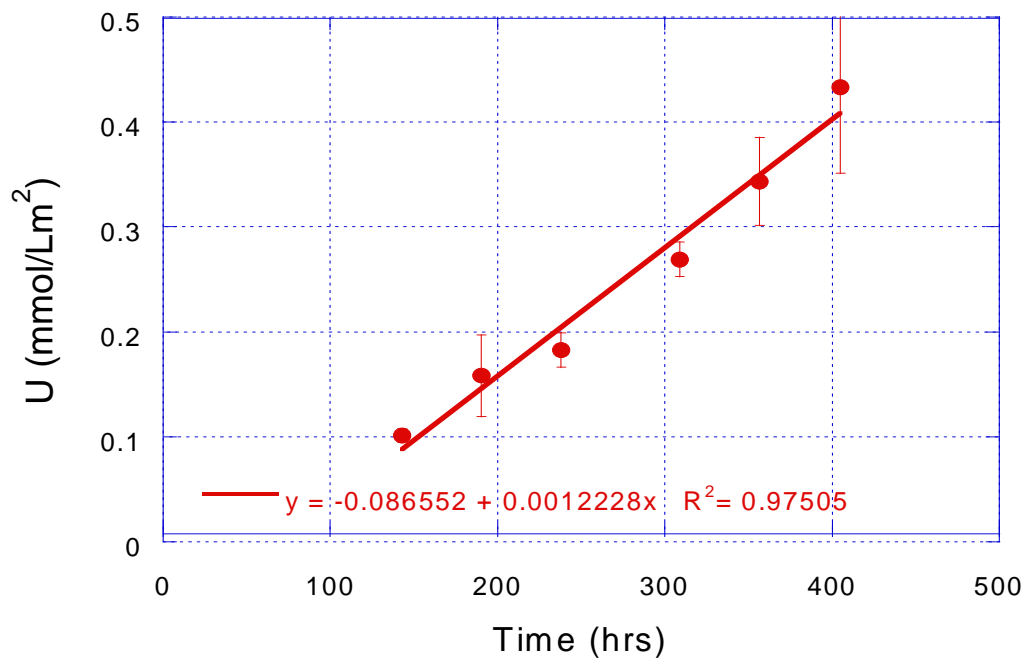


Figure 67: Uranium concentration with rate of $Zr_{0.148}Mg_{0.834}U_{0.010}Er_{0.007}O_{1.16}$ in concentrated nitric acid. Error bars represent standard deviation of three samples.

7.0 mol. % to 14.8 mol. % the rate of uranium dissolution fell to 1.2 μmol/L·m$^2$ [Figure 67]. Both samples display incongruent dissolution because of the preferential leaching of uranium and erbium from the lattice. This can be seen by examining the amount of material in solution compared to the total amount of material in the sample for each component. This is shown in Figure 68 and Figure 69 as the wt. % of the material in solution for zirconium, uranium, and erbium.
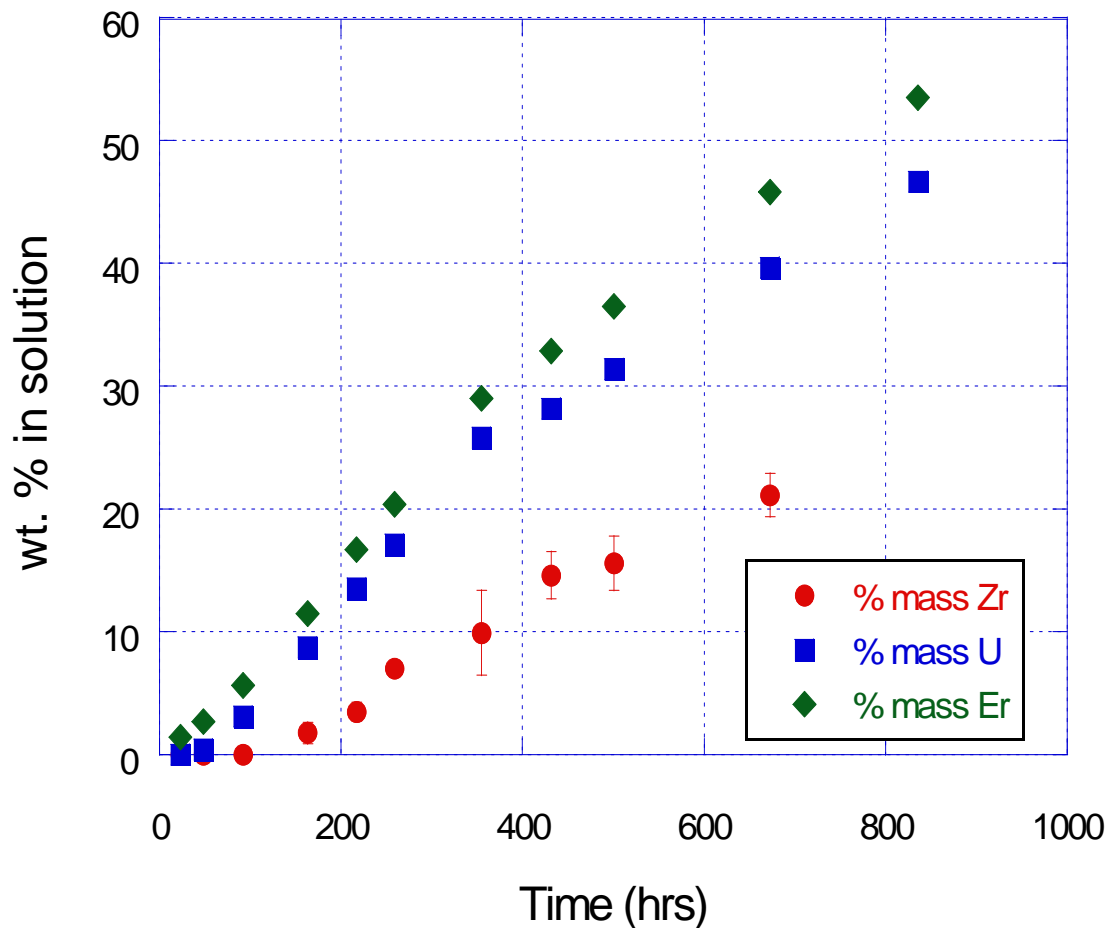


Figure 68: Weight percent of total sample $Zr_{0.070}Mg_{0.914}U_{0.009}Er_{0.006}O_{1.08}$ in concentrated nitric acid. Error bars represent standard deviation of three samples.
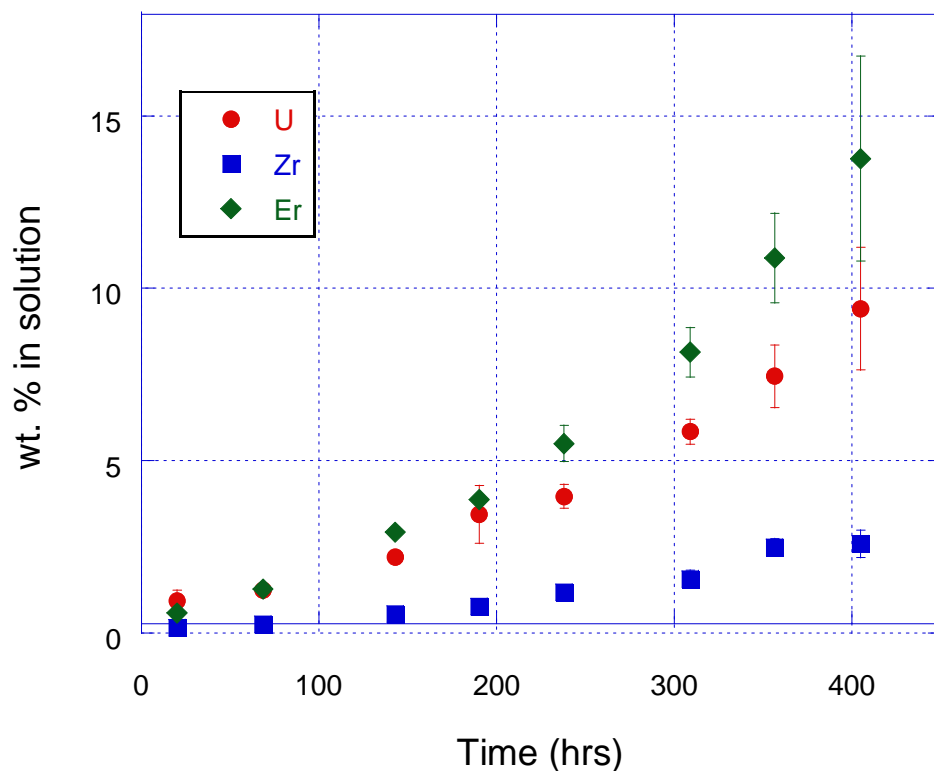
Figure 69: Weight percent of total sample $Zr_{0.148}Mg_{0.834}U_{0.010}Er_{0.007}O_{1.16}$ in concentrated nitric acid. Error bars represent standard deviation of three samples.

It is evident that there is a much higher percentage of uranium and erbium being dissolved than there is zirconium. The residue left at the bottom of the flask was examined by x-ray diffraction and was found to be pure cubic zirconia with a small amount of magnesium oxide (periclase) [Figure 70]. This further confirms that almost all of the magnesium oxide is dissolved. There are two zirconia phases with different lattice parameters after dissolution when there was only one in the beginning. This means that the chemical makeup of the zirconia has changed, which can be explained by the proposed incongruent dissolution which would strip the zirconia of the larger uranium and erbium cations that expand the lattice parameter.
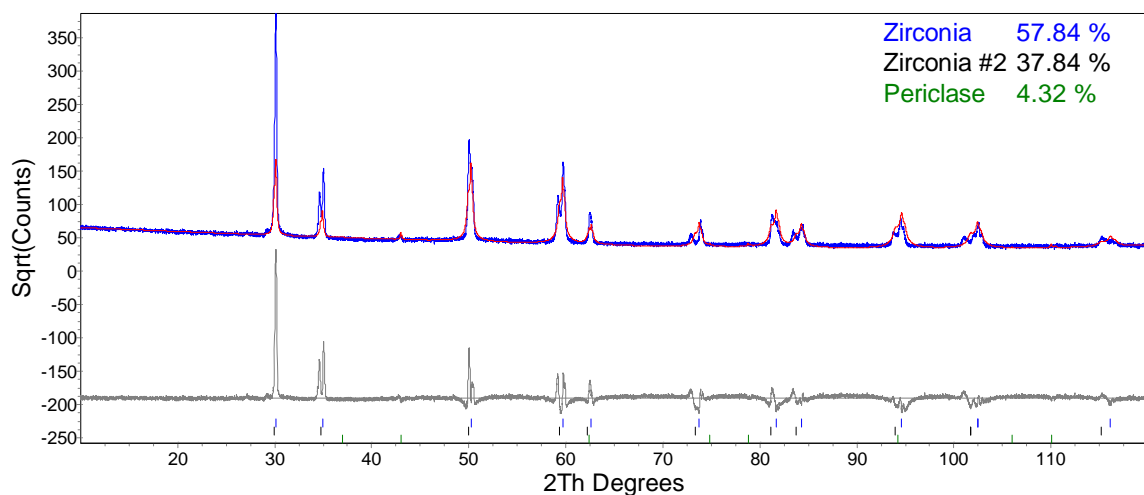
Figure 70: X-ray diffraction pattern (blue) with fit (red) and difference curve (grey) of the residue after nitric acid dissolution of $Zr_{0.148}Mg_{0.834}U_{0.010}Er_{0.007}O_{1.16}$.

This preferential leaching of uranium and erbium is only evident at extremely low concentrations of zirconium oxide. This leaching has been shown to reach as much as 50 wt. % over nearly 1,000 hours of the total uranium and erbium within the sample, which proves more uranium is being dissolved than that on the original surface. This can be explained by examining the composition of the zirconia phase. At the lowest concentration of zirconium oxide the uranium and erbium content within the zirconia is 20 and 10 wt. % respectively. Together with an additional 5 wt. % of magnesium dissolved into the zirconia, leachable material accounts for 35 wt. % of the cations on the lattice. Because other cations can make up 30 at. % of the lattice, leaching this amount of material is believed to destabilize the zirconia, causing it to fall apart and expose a new surface that can be leached for additional uranium, erbium, and magnesium. This mechanism not only explains the sample compositions prone to dissolution both before and after exposure to nitric acid, but also the linear kinetics of that dissolution. This is

116

also evidence that zirconia alone is unable to predict the behavior of the composite and that cerium oxide is not a suitable chemical homolog for uranium oxide as it is not soluble from the zirconia matrix. Plutonium oxide will be evaluated in future studies to assess the accuracy of uranium as a plutonium homolog.

### 5.2.2 Sulfuric acid dissolution with uranium containing ceramic

A single sample composition, $Zr_{0.148}Mg_{0.834}U_{0.010}Er_{0.007}O_{1.16}$, was tested for dissolution in sulfuric acid. Experiments were performed with 5 M, 9 M, and concentrated 18 M sulfuric acid. The acid was heated to boiling and samples were immersed for over 100 hours. Sulfuric acid has a stronger nucleophile, $SO_4^{2-}$, than that of nitric acid ($NO_3^-$), which may make it possible to attack the cation sites of the zirconia and dissolve the material. Sulfuric acid is not the acidic media used in reprocessing. Therefore, an additional step would be required to precipitate out the dissolved material and redissolve it in nitric acid for the purpose of reprocessing. This would add additional complication and cost to the recycling of this fuel. It does however, eliminate the need to use hydrofluoric acid, which would reduce the radiotoxicity of the solvent used in reprocessing. Sample dissolution was followed by examining the concentration of cations in solution by inert coupled plasma – atomic emission spectroscopy and the nature of those species was evaluated by time resolved laser spectroscopy.

It was found that 5 M and 9 M sulfuric acid were inadequate at dissolving any appreciable amount of the zirconia phase as seen by ICP-AES, which has an approximate detection limit of 1-10 ppm in the method described above. Concentrated sulfuric acid was also unable to dissolve zirconium, uranium, or erbium indicating that kinetics factors play a large role in the dissolution of this material. Magnesium oxide was easily

117

dissolved within 10 hours by all concentrations of sulfuric acid. Its kinetics were fast enough and the extent of dissolution was so complete that it seemed independent of the sulfuric acid concentration under these conditions as can be seen in Figure 71. It is shown there that both 5 M and 9 M sulfuric acid dissolve the magnesium oxide phase to completion within 10 hours at virtually the same rate. This fast, complete dissolution of magnesium oxide should leave behind a porous zirconia matrix with a high surface area to volume ratio that will improve the kinetics of the overall dissolution.
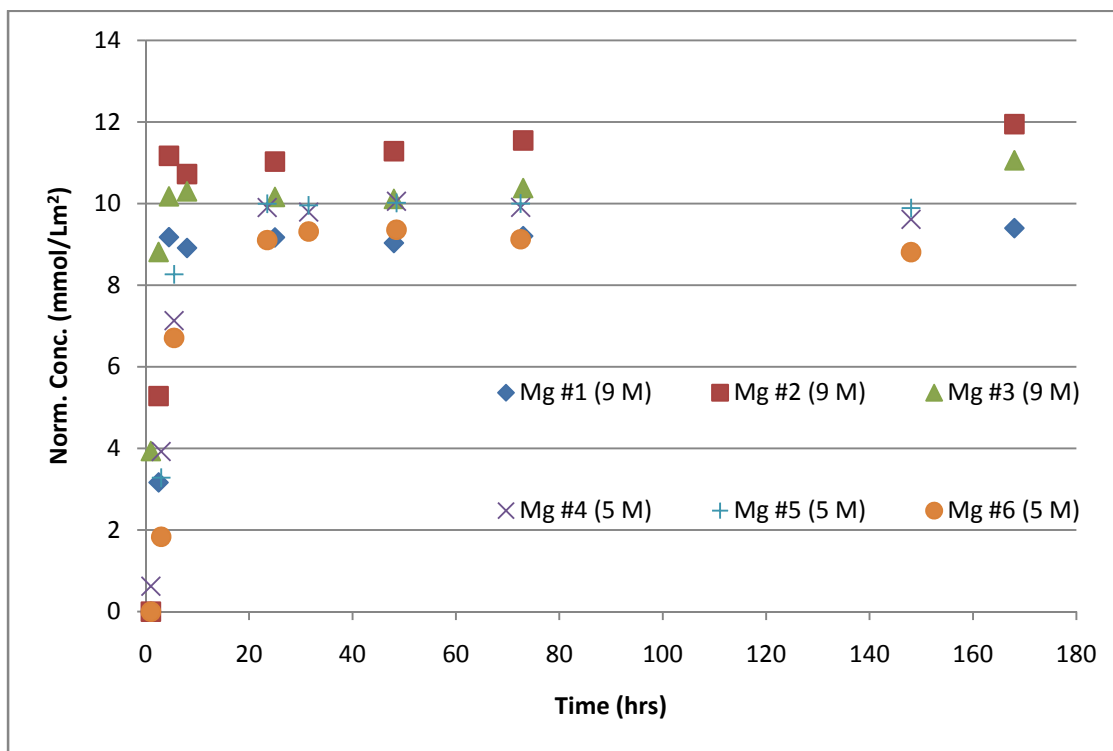


Figure 71: Surface area normalized concentration of magnesium from six samples of $Zr_{0.148}Mg_{0.834}U_{0.010}Er_{0.007}O_{1.16}$ in 5 M and 9 M sulfuric acid.
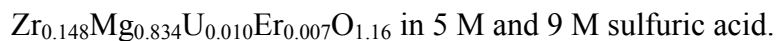
Concentrated sulfuric acid (18 M) was the only examined condition that was successful in dissolving any of the zirconia phase. As can be seen in Figure 72,

concentrated sulfuric acid was able to dissolve a measurable amount of zirconium in solution and was able to solubilize an initial amount of uranium and erbium within the first 24 hours of the experiment, which remained constant for the remainder of the time studied. The sample size of these experiments did not exceed 450 mg in 150 mL of sulfuric acid. The amount of uranium dissolved in solution was less than 12 wt. % of the total uranium in the sample. The erbium was significantly more soluble with 46 wt % of the total erbium dissolved in concentrated sulfuric acid.
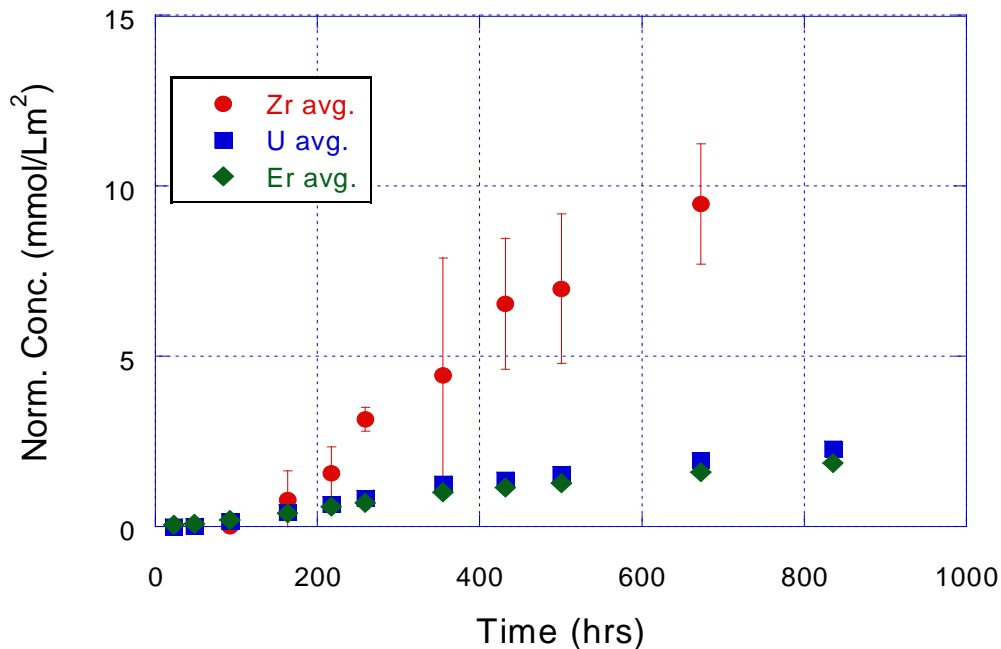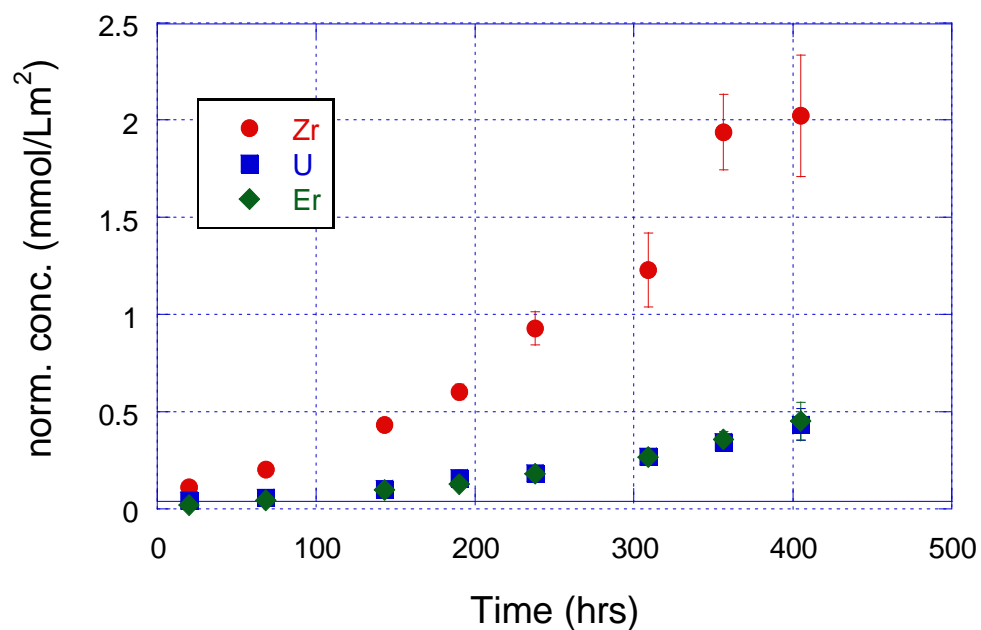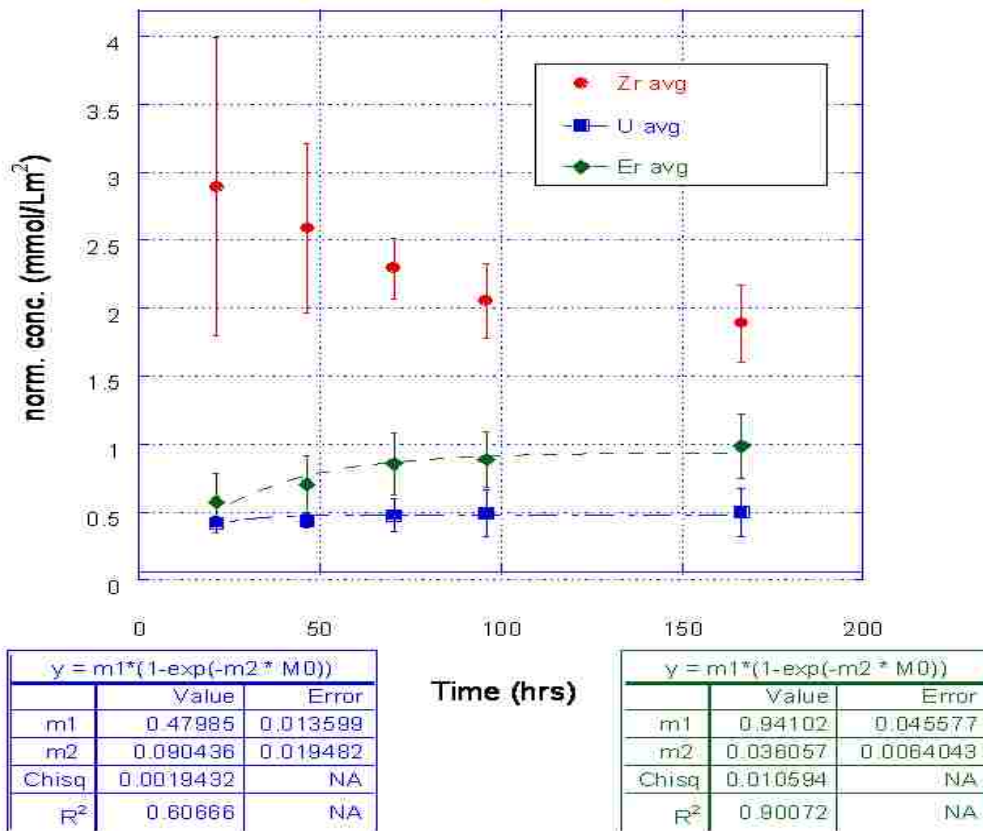


Figure 72: Surface area normalized concentrations of $Zr_{0.148}Mg_{0.834}U_{0.010}Er_{0.007}O_{1.16}$ in concentrated sulfuric acid. Error bars represent standard deviation of three samples.

The zirconium exhibits different behavior in that its concentration reaches a maximum at 24 hours with a significant standard deviation between samples and then drops to an equilibrium amount of around 2 mmol/Lm$^2$. This is due to the low solubility of zirconium in sulfuric acid. The sulfuric acid is successful in breaking up the matrix and releasing the cations within the zirconia. The uranium and erbium are solubilized to an extent and the zirconium is suspended as a colloid. As the colloids conglomerate, they drop out of solution lowering the concentration to an equilibrium amount of solubilized zirconium. This also accounts for the large range of concentrations at the maximum zirconium concentration as this is based on suspended colloids which is highly influenced by particle size distribution, which varies from sample to sample of crushed ceramic.

Colloidal suspension presented more of a problem with samples that were finely crushed than those that had a slightly lower surface area to volume ratio. This was confirmed by time resolved laser spectroscopy. At 200 nsec after the laser pulse [Figure 73] the sample with a small surface area to volume ratio shows a typical fluorescence pattern due to the presence of uranyl, though enhanced because of the high concentration of sulfate. The sample with a slightly higher surface area to volume ratio has a significant background due to scattering in addition to typical uranyl fluorescence spectra. This background was proven to be due to colloidal scattering by taking a spectra at 1000 nsec after the laser pulse at which time the scattering process has concluded. At this time, the background seen in the previous spectra is not present and only the contribution due to uranyl fluorescence is present as seen in Figure 74. The lifetimes of the two fluorescent samples indicate that they have slightly different speciation, though this may be an effect of the highly complexing environment. Also, the sample may have

120

had colloidal material encompassing the uranyl ion allowing it a non-radiative de-excitation route which would have acted as a static quenching agent.
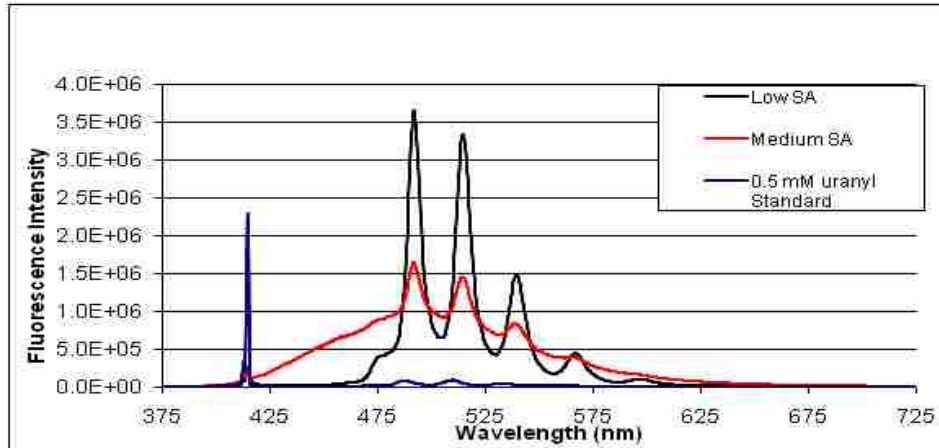


Figure 73: Time resolved laser fluorescence of two samples of

$Zr_{0.148}Mg_{0.834}U_{0.010}Er_{0.007}O_{1.16}$ labeled by relative surface

area to volume ratios 200 nsec after fluorescence.
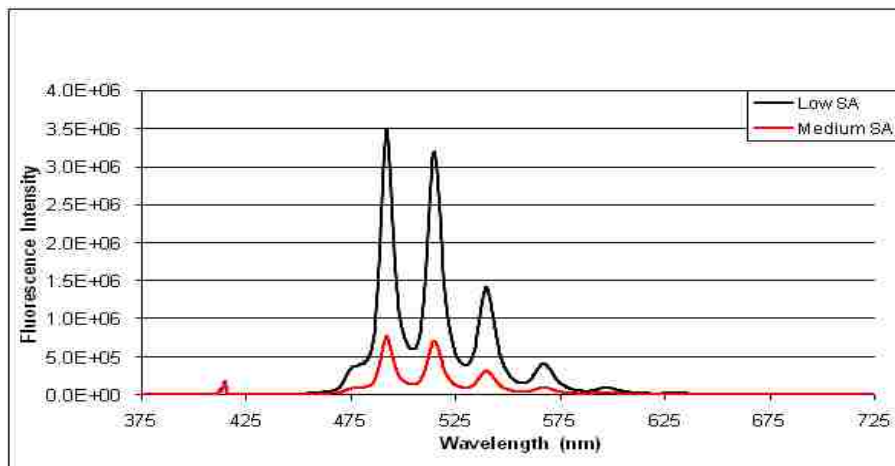


Figure 74: Time resolved laser fluorescence of two samples of

$Zr_{0.148}Mg_{0.834}U_{0.010}Er_{0.007}O_{1.16}$ labeled by relative surface

area to volume ratios 1000 nsec after fluorescence.

### 5.2.3 Conclusion of acidic dissolution with uranium containing ceramic

This study was successful in exploring the possibility of reprocessing zirconia-magnesia inert matrix fuel through dissolution in nitric and sulfuric acid. These studies were unique in that they incorporated a fissile component using an actinide and a burnable poison as erbium oxide. It was found that this is vital to accurately represent the dissolution behavior of the ceramic and that uranium has a different chemical behavior than cerium, a common actinide homolog, under these conditions. This is best illustrated in the dissolution behavior of the material in concentrated nitric acid. It was shown that at low levels of zirconium oxide, the high concentration of uranium within the zirconia phase and high surface area to volume of that phase enables the leaching of uranium, erbium, and magnesium from the zirconia lattice. At significantly high levels of these substituting ions it is possible to destabilize the lattice due to leaching and consequently dissolve the zirconia phase through a linear, incongruent dissolution process. This process does however require a great deal of time and only happens under specific chemical compositions. Because of this, sulfuric acid was also explored as a means of dissolving the fuel. It was found that only 12 wt. % of the uranium in the sample was dissolved under current experimental conditions. This would mean that large ratios of sulfuric acid to fuel would be needed to dissolve the material completely, making it a highly inefficient process. In addition there is significant formation of colloids that conglomerate and settle to the bottom of the vessel. This could pose engineering problems in the processing of large amounts of material. Both sulfuric and nitric acid pose problems to the dissolution of zirconia-magnesia inert matrix fuels. Future studies will use plutonium as the fissile component of the fuel and compare chemical behavior to

that of the uranium and cerium homolog studies. In addition future studies will also incorporate the use of hydrofluoric acid to further enhance the dissolution process with nitric acid.


### 5.3 Acidic dissolution with plutonium containing ceramic

### 5.3.1 Nitric acid dissolution with plutonium containing ceramic

Three sample compositions ($Zr_{0.21}Mg_{0.77}Pu_{0.011}Er_{0.0078}O_{1.2}$, $Zr_{0.093}Mg_{0.89}Pu_{0.0065}Er_{0.0052}O_{1.1}$, and $Zr_{0.061}Mg_{0.93}Pu_{0.0059}Er_{0.0045}O_{1.1}$) were used to explore the dissolution of plutonium containing ceramic in nitric acid. These compositions were chosen because they are comparable to the sample compositions tested with uranium containing samples ($Zr_{0.148}Mg_{0.834}U_{0.010}Er_{0.007}O_{1.16}$ and $Zr_{0.070}Mg_{0.914}U_{0.009}Er_{0.006}O_{1.08}$). Pellets of this material that measured 3 to 4 mm in diameter were placed in a round bottom flask with 100 mL of concentrated nitric acid and the solution was brought to a boil (~120 $^{o}$C) for 48 hours. Only plutonium was analyzed for via liquid scintillation counting. This allowed for smaller sample sizes which were chosen to be 100 μL and were diluted with 2 mL of water before adding 10 mL of scintillation cocktail. Samples were counted for a maximum of 1 hour or 2 σ % counting error between 200 and 500 keV. The detection limit of the liquid scintillation counter is 0.1 Bq, which given the method and sample size puts the detection limit at 0.002 wt. % of the total plutonium in the sample. Zirconium, magnesium, and erbium were not analyzed, because their behavior was well described in previous studies with cerium and uranium presented earlier in these studies.

The concentrations calculated from the activity detected by liquid scintillation are

normalized to geometric surface area and plotted in Figure 75. It was found that while
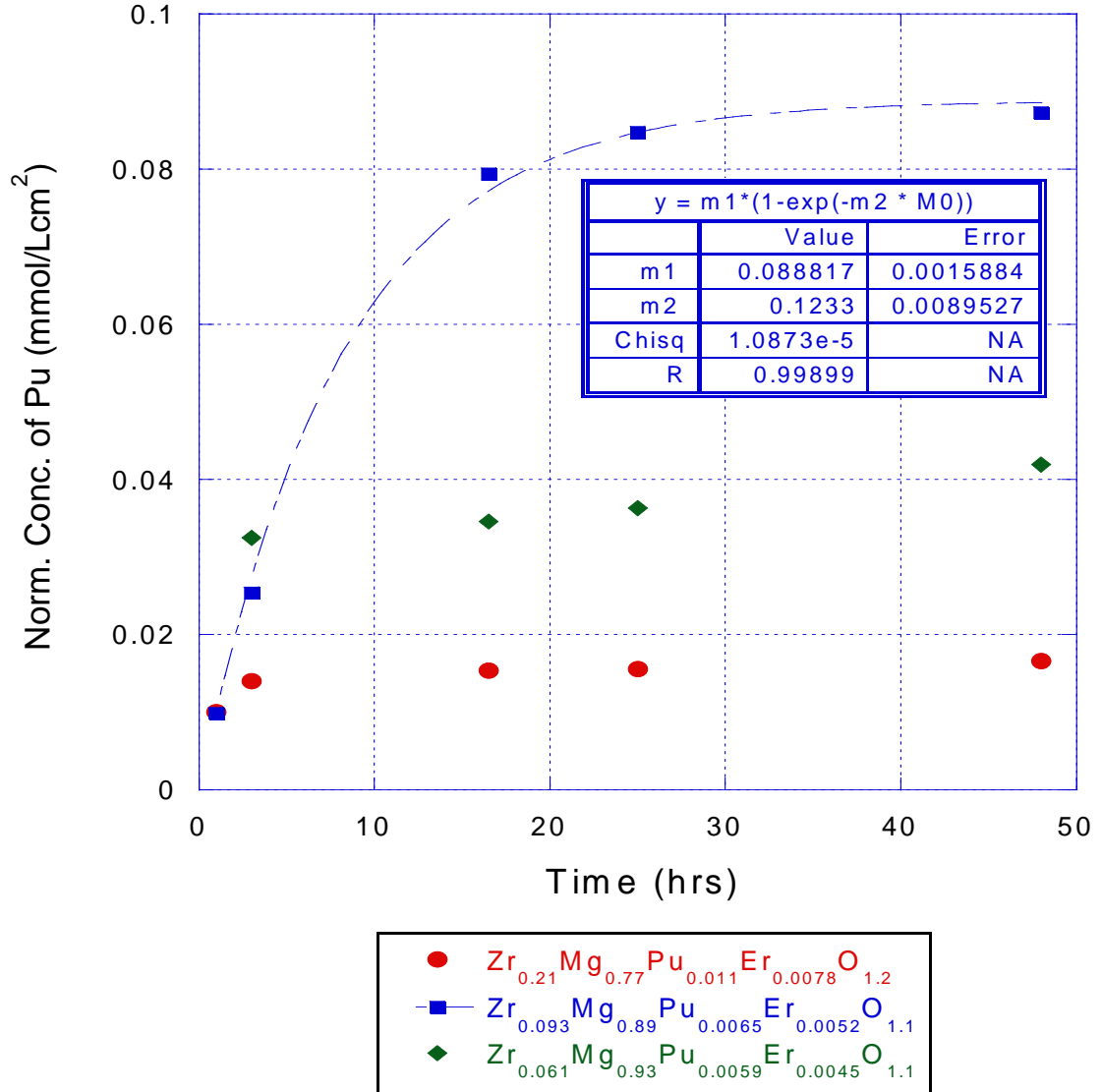


Figure 75: Geometric surface area normalized concentrations of plutonium in

concentrated nitric acid from $Zr_{0.21}Mg_{0.77}Pu_{0.011}Er_{0.0078}O_{1.2}$,

$Zr_{0.093}Mg_{0.89}Pu_{0.0065}Er_{0.0052}O_{1.1}$, and

$Zr_{0.061}Mg_{0.93}Pu_{0.0059}Er_{0.0045}O_{1.1}$

with first order kinetics fit.

within the first 4 hours the amount of plutonium in solution trends with chemical composition. That is to say the more plutonium and magnesium and the less zirconium lead to higher concentration of plutonium dissolved in solution as expected. However, after 4 hours the middle chemical composition ($Zr_{0.093}Mg_{0.89}Pu_{0.0065}Er_{0.0052}O_{1.1}$) continues to increase while the other two compositions seem to plateau. It is inconclusive from the data collected as to the kinetics mode of these two samples. It is possible that they follow first order kinetics but have reached a diffusion controlled maximum where the zirconia matrix makes it impossible to further leach plutonium, which appears to be the case in $Zr_{0.21}Mg_{0.77}Pu_{0.011}Er_{0.0078}O_{1.2}$. It could also be that this leaching process will continue in a linear trend as it seems to continually increase in sample $Zr_{0.061}Mg_{0.93}Pu_{0.0059}Er_{0.0045}O_{1.1}$. It can be concluded that like uranium this is an incongruent dissolution that involves the leaching of plutonium from the zirconia matrix. The concentration plateau that is reached in all samples is micro molar concentrations while the saturation limit for plutonium in nitric acid is on the order of molar. Because of this it was concluded that the concentration limit achieved in this experiment is due to the ability of zirconia to retain plutonium. Sample $Zr_{0.093}Mg_{0.89}Pu_{0.0065}Er_{0.0052}O_{1.1}$ seems to follow first order kinetics. It was found to have a concentration limit of $0.089\pm0.002$ mmol/Lcm$^2$ and an initial rate constant of $0.12\pm0.01$ hrs$^{-1}$.

This first order behavior is a significant deviation from uranium studies that suggested a linear dissolution rate in nitric acid. This could be due to the increased detection limit with plutonium. It is possible that uranium follows first order kinetics for the first 48 hours while the concentrations, below 0.03 mM, are too low to be monitored by ICP-AES. After this period of time it is hypothesized that all of the plutonium that is

close to the surface is in solution and a leaching process then dictates the kinetics and follows a linear trend. If the kinetics are assumed to be linear after the initial 24 hours then the slope of that line can be estimated by the slope of the points taken after 24 hours. If this is done then the slopes are 0.43, 1.1, and 2.4 mmol/L·hrs·cm$^2$ x 10$^{-4}$ for samples $Zr_{0.21}Mg_{0.77}Pu_{0.011}Er_{0.0078}O_{1.2}$, $Zr_{0.093}Mg_{0.89}Pu_{0.0065}Er_{0.0052}O_{1.1}$, and $Zr_{0.061}Mg_{0.93}Pu_{0.0059}Er_{0.0045}O_{1.1}$ respectively. This rate trends with composition in the same way that it did for uranium. It also increases by the same order of magnitude for the same range in compositions as it did for uranium. This further supports that the kinetics are similar. It is recognized that this trend is only determined from two points and therefore impossible to determine a quantitative result. It is presented here merely as a suggestion to behavior and should be a subject for further study. The detection limit for the uranium studies was not low enough to detect the first order behavior in the beginning of the dissolution and the plutonium dissolution was not carried on long enough to conclusively identify the linear behavior at greater time.

This explanation of the kinetics does not explain the differences in the quantity of material dissolved into solution. A table of the physical characteristics of the pellets used in this study is found in Table 12. As can be seen in the table above, the samples show

Table 12: Physical properties for plutonium containing inert matrix fuel used in nitric acid dissolution study.

| Sample Composition | Total Pu in Sample | Geometric Surface Area | Mass of Sample | Density of Sample |
|---|---|---|---|---|
| $Zr_{0.21}Mg_{0.77}Pu_{0.011}Er_{0.0078}O_{1.2}$ | 2.98 mg | 45 mm$^2$ | 72.0 mg | 3.6 g/cm$^2$ |
| $Zr_{0.093}Mg_{0.89}Pu_{0.0065}Er_{0.0052}O_{1.1}$ | 2.60 mg | 45 mm$^2$ | 84.4 mg | 4.2 g/cm$^2$ |
| $Zr_{0.061}Mg_{0.93}Pu_{0.0059}Er_{0.0045}O_{1.1}$ | 2.72 mg | 43 mm$^2$ | 91.0 mg | 4.2 g/cm$^2$ |

very little difference in physical properties.   The maximum amount of plutonium in
solution does not show a trend with density, surface area, or mass of sample.  The sample
with the least amount of plutonium shows the highest amount in solution while the
highest amount of plutonium in a sample has the lowest amount in solution.    The
difference in solution is far greater than the 15 % relative difference in plutonium
content.   The amount of plutonium in solution as compared to the total amount of
plutonium in the sample can be seen in Figure 76 as the wt. % of plutonium in solution.
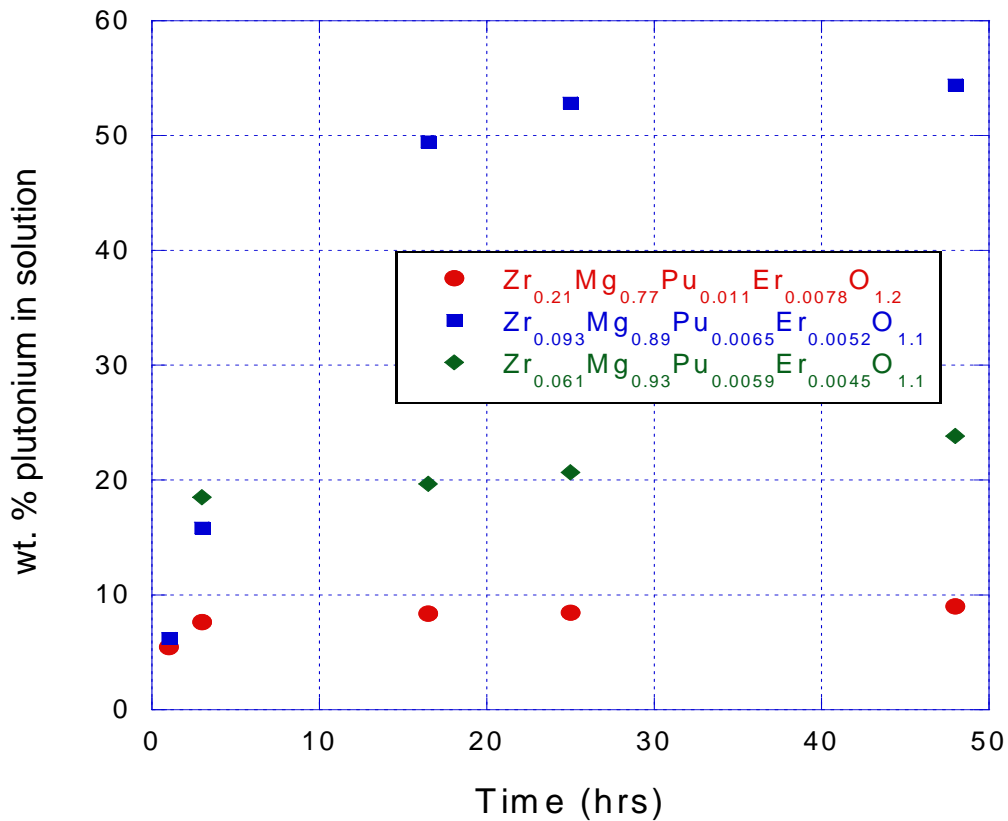


Figure 76: Weight percent of plutonium in concentrated nitric acid from

$Zr_{0.21}Mg_{0.77}Pu_{0.011}Er_{0.0078}O_{1.2}$, $Zr_{0.093}Mg_{0.89}Pu_{0.0065}Er_{0.0052}O_{1.1}$,

and $Zr_{0.061}Mg_{0.93}Pu_{0.0059}Er_{0.0045}O_{1.1}$
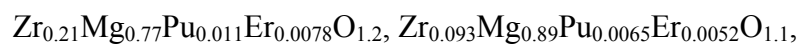
This difference in amount of plutonium initially dissolved into solution is believed to be due to the effective surface area of the zirconia phase. These samples were broken in order to sample for characterization studies and it is possible that differences due to sampling effect the amount of zirconia surface that is accessible to the nitric acid. The greater the accessible surface area the more of the plutonium is able to be solubilized by the nitric acid. In the case of $Zr_{0.093}Mg_{0.89}Pu_{0.0065}Er_{0.0052}O_{1.1}$ more than 50 wt. % is able to be dissolved in the initial 48 hours.

Interestingly if it is assumed that the linear rate proposed is true for all samples, both samples $Zr_{0.21}Mg_{0.77}Pu_{0.011}Er_{0.0078}O_{1.2}$ and $Zr_{0.093}Mg_{0.89}Pu_{0.0065}Er_{0.0052}O_{1.1}$ will take the same amount of time to dissolve, approximately 30 days. The greater linear rate due to chemical composition is able to compensate for the low amount of plutonium immediately dissolved due to low effective surface area. Given these assumptions, $Zr_{0.061}Mg_{0.93}Pu_{0.0059}Er_{0.0045}O_{1.1}$ will take over twice as long to dissolve at 70 days. These times are only slightly faster than studies performed with uranium that suggested complete dissolution could be achieved in 70 to 160 days depending on sample composition. Further experimentation is needed to determine if these observations are differences due to the variation in chemistry from uranium to plutonium or if they are merely two different stages of the same kinetics mechanism.

5.3.2 Hydrofluoric acid – nitric acid wet ashing of plutonium containing inert matrix fuel

One sample each of $Zr_{0.76}Mg_{0.10}Pu_{0.078}Er_{0.062}O_{1.9}$, $Zr_{0.64}Mg_{0.29}Pu_{0.029}Er_{0.041}O_{1.7}$, $Zr_{0.56}Mg_{0.36}Pu_{0.037}Er_{0.044}O_{1.6}$ and $Zr_{0.44}Mg_{0.47}Pu_{0.042}Er_{0.048}O_{1.5}$ were used in a dissolution experiment with hydrofluoric acid. The physical properties of the samples are listed in Table 13. Samples were placed in a 10 mL Teflon vial and 5 mL of 7 M nitric acid and

0.05 M hydrofluoric acid solution was added to the vial. An addition 1-2 mL of 30 % hydrogen peroxide was added to the vial and the vial was heated to dryness. This was repeated five times for each sample before the sample was reconstituted in 7 M nitric acid [Section 2.10]. The amount of plutonium in solution was monitored before each heating by removing a small sample and measuring the activity by LSC. The samples for LSC were not filtered, with the exception of after the sample was reconstituted in 7 M nitric acid. At that point the sample was filtered with a 0.45 µm filter and then counted.

Table 13: Physical properties of plutonium containing inert matrix fuel samples used in HF-HNO$_3$-peroxide dissolution.

| Sample Composition | Total Pu in Sample | Geometric Surface Area | Mass of Sample | Density of Sample |
|---|---|---|---|---|
| $Zr_{0.76}Mg_{0.10}Pu_{0.078}Er_{0.062}O_{1.9}$ | 1.9 mg | 8.8 mm$^2$ | 11.9 mg | 5.5 mg/cm$^3$ |
| $Zr_{0.64}Mg_{0.29}Pu_{0.029}Er_{0.041}O_{1.7}$ | 2.63 mg | 16.5 mm$^2$ | 35.1 mg | 5.5 mg/cm$^3$ |
| $Zr_{0.56}Mg_{0.36}Pu_{0.037}Er_{0.044}O_{1.6}$ | 1.93 mg | 13.2 mm$^2$ | 19.7 mg | 4.6 mg/cm$^3$ |
| $Zr_{0.44}Mg_{0.47}Pu_{0.042}Er_{0.048}O_{1.5}$ | 1.4 mg | 7.0 mm$^2$ | 11.7 mg | 7.7 mg/cm$^3$ |

There was no evidence of a change in activity due to filtration and it was therefore determined that colloid formation with plutonium in nitric acid was not a significant concern. There was also no indication that the final addition of nitric acid left previously dissolved material undissolved. That is to say that the material that was dissolved by the nitric-hydrofluoric-peroxide solution is soluble in nitric acid. Because of this, the amount of activity in the final nitric acid solution is taken to be the total amount of plutonium dissolved over the five wet ashing cycles. The amount of plutonium dissolved in solution increased after every wet ashing cycle, but it was erratic and inconsistent from sample to

sample. This resulted in little information on the kinetics of the dissolution. The total amount of plutonium that was dissolved was determined and is given in Table 14. As can be seen in the amount of plutonium dissolved in nitric acid, there is no trend with chemical composition. This coupled with no trend in physical properties given in Table 13, suggests that the kinetics and extent of dissolution is dependent on a property that has not been measured, such as effective surface area of the zirconia phase. This would be consistent with previous studies involving nitric acid and would further support the incongruent leaching process described previously. This dissolution process is successful in dissolving up to 81.4 wt. % of the total plutonium from sample $Zr_{0.56}Mg_{0.36}Pu_{0.037}Er_{0.044}O_{1.6}$. This indicates that this solution can be used to successfully dissolve significant amounts of the material. Increasing the surface area by crushing the material should aid in the dissolution process. Crushing of the material can be aided by dissolving the magnesium oxide phase in an initial dissolution step of nitric acid, which would leave behind a porous zirconia phase that would be easily crushed exposing a large surface area. It also has the advantage that samples are already dissolved in the media of choice for performing separations in a reprocessing scheme.

Table 14: Weight percent dissolved from plutonium containing inert matrix fuel in HF-$HNO_3$-peroxide solution.

| Sample Composition | wt. % dissolved |
|---|---|
| $Zr_{0.76}Mg_{0.10}Pu_{0.078}Er_{0.062}O_{1.9}$ | 47.9 |
| $Zr_{0.64}Mg_{0.29}Pu_{0.029}Er_{0.041}O_{1.7}$ | 29.7 |
| $Zr_{0.56}Mg_{0.36}Pu_{0.037}Er_{0.044}O_{1.6}$ | 81.4 |
| $Zr_{0.44}Mg_{0.47}Pu_{0.042}Er_{0.048}O_{1.5}$ | 72.3 |

5.3.3 Conclusions of acidic dissolution study with plutonium containing inert matrix fuel

It was found that nitric acid is successful in at least partially dissolving plutonium from a zirconia matrix. It is proposed that the first 24 hours of dissolution is dominated by first order kinetics as the plutonium at the surface is dissolved by nitric acid. This was not observed in uranium due to detection limits. After 24 hours it is hypothesized that the kinetics will follow a linear trend due to the leaching of plutonium from the zirconia matrix leading to incongruent dissolution. This was observed in uranium and the rate was found to trend with both magnesium oxide content and concentration of plutonium within the zirconia phase. This behavior in plutonium containing samples is supported by fitting points taken after 24 hours to a line, which shows the same trend as in rates determined in uranium samples. The amount of plutonium in solution at any time is related to both the rate of dissolution and effective surface area of zirconia. This effective surface area is why the sample with moderate magnesium and plutonium exhibited the greatest amount of dissolved plutonium after 48 hours. It was concluded that given the current kinetics model it would take between 30 and 70 days depending on composition and surface area to completely dissolve the plutonium from the material, which is only slightly faster than with uranium (70 to 160 days).

Hydrofluoric acid and hydrogen peroxide were added to nitric acid to improve the dissolution kinetics of the experiment. It was found that in five wet ashing cycles it was possible to dissolve up to 81 wt. % of the plutonium from the matrix. This is significantly more and also much faster than with nitric acid alone. The amount of plutonium dissolved continues to increase with each ashing, so it is predicted to be possible to use this dissolution method for the complete dissolution of plutonium. The

amount of plutonium dissolved with each ashing was inconsistent and therefore impossible to predict the kinetics.  The amount of plutonium dissolved did not trend with the physical or chemical properties that were measured.  It is believed to be due to the effective surface area of the zirconia phase as was the case with nitric acid dissolution of uranium containing samples.  It should also be noted that the HF-$HNO_3$-peroxide dissolution study was carried out with sample compositions that were more durable (higher zirconium oxide concentrations) than those that were carried out with nitric acid alone.  Therefore, the sample compositions with greater concentrations of plutonium and magnesium oxides should dissolve faster and to a greater extent than the samples with higher zirconium oxide.

CHAPTER 6


IRRADIATION DAMAGE STUDIES

6.1 Heavy ion irradiation in fluorite and related structures

Radiation tolerance is vital to nuclear materials that are to be used in high dose fields, such as fuels and waste forms. The dissolution properties presented in previous chapters are only valid if the material remains unchanged after the high irradiation dose it will receive during its lifetime or function. This chapter presents the theories for irradiation tolerance in fluorite structure derivatives published by Sickafus et. al.(60) and uses them to explain radiation damage studies in zirconia-magnesia inert matrix fuel as compared to the delta phase compound $UY_6O_{12}$.

Sickafus suggests using phase diagrams to predict irradiation tolerance in fluorite structure derivatives. Delta phase compositions of $A_4B_3O_{12}$ and pyrochlore compositions of $A_2B_2O_7$ where B is zirconium oxide were studied specifically. It can be shown in the binary temperature-composition (T-C) phase diagrams of zirconium oxide and the lanthanides that there are trends in the stability of these phases. As the cation size decreases across the rare earth compounds from lanthanum to gadolinium the temperature of the order to disorder transition from pyrochlore to disordered fluorite goes down dramatically [Figure 77]. At dysprosium there is no stable delta or pyrochlore phase and the phase diagram is dominated by the disordered fluorite structure. After this, the order to disorder transition temperature from a delta phase to a disordered fluorite goes up slightly as the cation radius of the lanthanide is increased [Figure 77]. Molecular statics calculations show that this trend is duplicated in the amount of energy it takes to create a

cation antisite and anion Frenkel defect (60). It is not surprising that the higher the energy it takes to create a point defect the more stable the phase is to temperature.

Radiation fields lead to point defects that cannot be avoided. Therefore, the better equipped the lattice is at storing these defects, the more radiation tolerant (at least to amorphization) the material is. If these point defects result in little stored energy, then it is less likely for them to cause changes in structure such as amorphization or defect clustering. These processes of lowering stored lattice energy result in swelling and drastically change the dissolution properties of the material and should therefore be avoided. Material with a low order to disorder transition temperature will correspond to having low stored lattice energy due to defects caused by radiation. Therefore, material with a low order to disorder transition temperature should perform better than those with higher temperature transitions and disordered fluorites should be highly radiation tolerant in terms of amorphization resistance. This idea of predicting radiation damage behavior from T-C phase diagrams was suggested by Sickafus et. al. (60) and is merely summarized here for clarity as it is relevant to irradiation studies presented in subsequent sections.

The importance of this in the zirconium oxide system is that lanthanides similar to the size of dysprosium (where there is no ordered sublattice) should show the most radiation tolerance. Furthermore, delta phase compounds should exhibit superior resistance to amorphization as compared to pyrochlores, which have been championed lately as highly radiation tolerant (61). Disordered fluorites will have the highest resistance to amorphization as compared to both delta phase and pyrochlore compounds. The study presented in this chapter uses the irradiation of a delta phase compound ($UY_6O_{12}$) and the

zirconia-magnesia inert matrix fuel, a disordered fluorite structure, to illustrate this point. If the crystal structure remains intact then the material behavior should be similar to that of the pristine sample. Therefore, the material should behave similar before and after use as a nuclear fuel, or after extended use as a waste form.
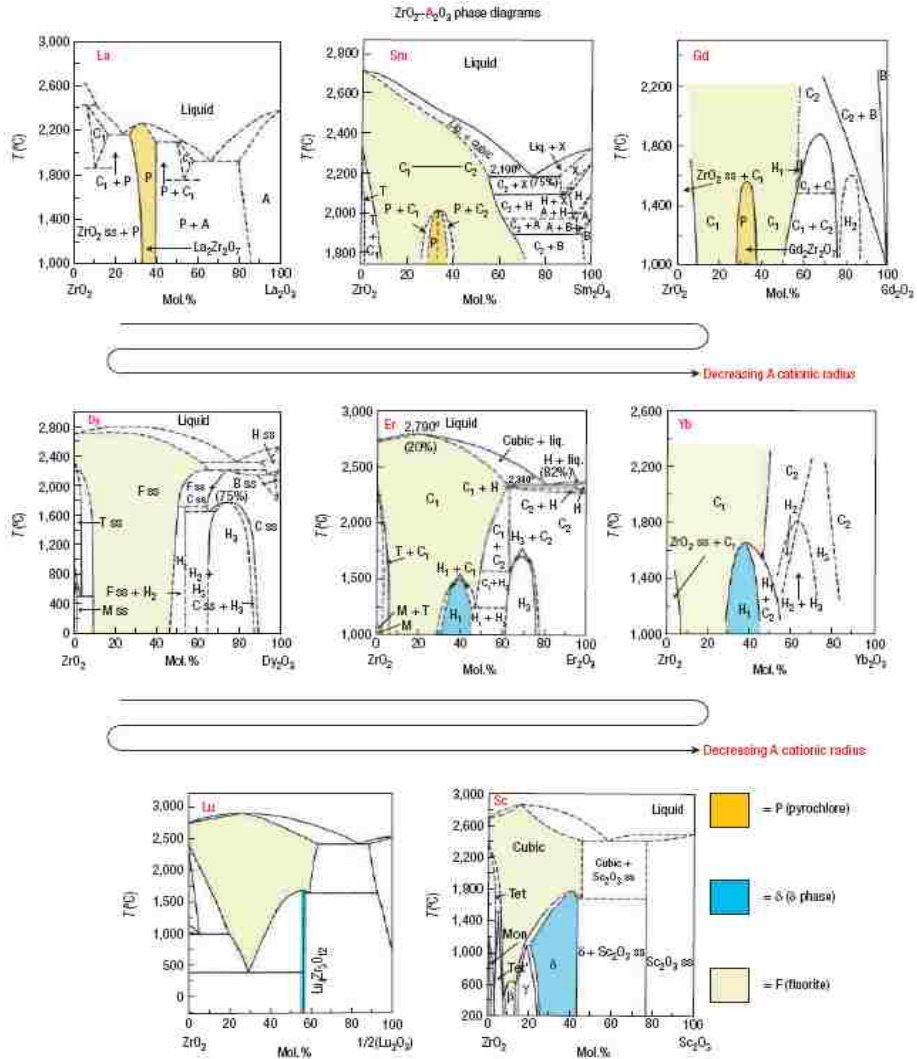


Figure 77: Selected T-C phase diagrams[(62)] in which various sesquioxides ($A_2O_3$) are mixed with the dioxide, zirconia ($ZrO_2$). Stability regions for the pyrochlore (P), delta phase ($\delta$) and fluorite (F) crystal structures are colored for clarity.

135

## 6.2 Heavy ion irradiation of $UY_6O_{12}$

The $\delta$-$Y_6U_1O_{12}$ exposed to heavy ion irradiation at cryogenic temperature does not amorphize, but undergoes an order-to-disorder transformation at a relatively high displacement damage dose. Density functional theory (DFT) is also used to calculate the energy to form a cation antisite in $Y_6U_1O_{12}$ and uranium surrogate $\delta$-phase compounds $Y_6W_1O_{12}$ and $Yb_6W_1O_{12}$. DFT results reveal that $Y_6U_1O_{12}$ with lowest cation antisite formation energy exhibits higher radiation-induced amorphization resistance than $Y_6W_1O_{12}$ and $Yb_6Y_1O_{12}$ (63).

Yttrium oxide (99.9 %) powder from Alpha Aesar was calcined at 1000 °C for 12 h, and mixed with $UO_2$ powder from Bio-Analytical Industries in the molar ratio of 1:3. The mixture was then ball milled in a stainless steel cup and pressed in a SPEX 13 mm die. Resulting pellets were oxidized in air for 4 h in a Mellen high temperature tube furnace at 350 °C, then up to 1500 °C for 12 h. The reaction was not completed so pellet fragments were placed in a box furnace for 72 h at 1000 °C under air, then remilled, repressed and resintered under air at 1500 °C for 72 h. X-ray diffraction measurements showed that the sintered pellets are primarily $\delta$-phase crystal structure, a structure characterized by rhombohedral symmetry. Ion irradiations were performed as described in Section 2.1. Irradiated samples were analyzed using both grazing incidence X-ray diffraction (GIXRD) and transmission electron microscopy (TEM) as described in Section 2.4 and 2.1, respectively. Irradiated samples were prepared in cross-sectional geometry for TEM examination using focused-ion-beam (FIB). TEM investigations were performed using Philips CM-30 and FEI Tecnai F30 electron microscopes operating at 300 kV [Section 2.14].

Figure 78 shows GIXRD patterns obtained from pristine $Y_6U_1O_{12}$ and $Y_6U_1O_{12}$ irradiated with 300 keV $Kr^{++}$ ions to fluences of $5\times10^{19}$ $Kr/m^2$ and $2\times10^{20}$ $Kr/m^2$. These ion fluences correspond to peak displacement damage doses of ~ 12 and 50 dpa (these are estimates based on the Monte Carlo ion transport code SRIM (64); 40 eV was used for the displacement threshold energy for all target atoms in these calculations). The pristine GIXRD pattern in Figure 78 is consistent with the rhombohedral δ-phase $Y_6U_1O_{12}$ structure.
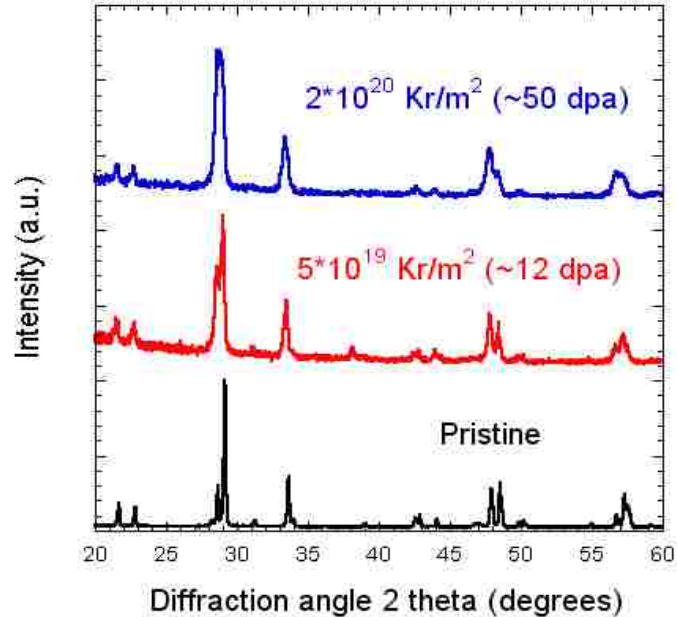


Figure 78: Grazing incidence X-ray diffraction (GIXRD) patterns obtained from $Y_6U_1O_{12}$ before and after irradiation with 300 keV $Kr^{++}$ ions.

Up to irradiation fluence of $2\times10^{20}$ $Kr/m^2$, some subtle peaks associated with the fluorite structural derivative δ phase disappear or diminishing with increasing ion dose, and some δ-phase peaks seem to persist; while the four prominent diffraction peaks (at ~29°, 34°,

48°, 57° 2θ) are more or less unaffected by irradiation. These peaks can be interpreted as arising from the parent fluorite structure. Also, these fluorite peaks broaden following ion irradiation, which is due either to decreased grain size or increased lattice strain.

Figure 79 shows a cross-sectional TEM image obtained from $Y_6U_1O_{12}$ irradiated with 300 keV $Kr^{++}$ ions to a fluence of $2\times10^{20}$ $Kr/m^2$ (corresponding to ~ 50 dpa). The inset microdiffraction (μD) patterns indicate a change in structure between the unirradiated substrate (bottom pattern) and the irradiated layer (top pattern). The substrate μD pattern is consistent with the rhombohedral δ-phase $Y_6U_1O_{12}$ structure. Superlattice reflections characteristic of pristine $Y_6U_1O_{12}$ are seen to disappear in the μD pattern obtained from the irradiated layer. This μD pattern from the irradiated layer can be indexed as consistent with a cubic, disordered fluorite phase.
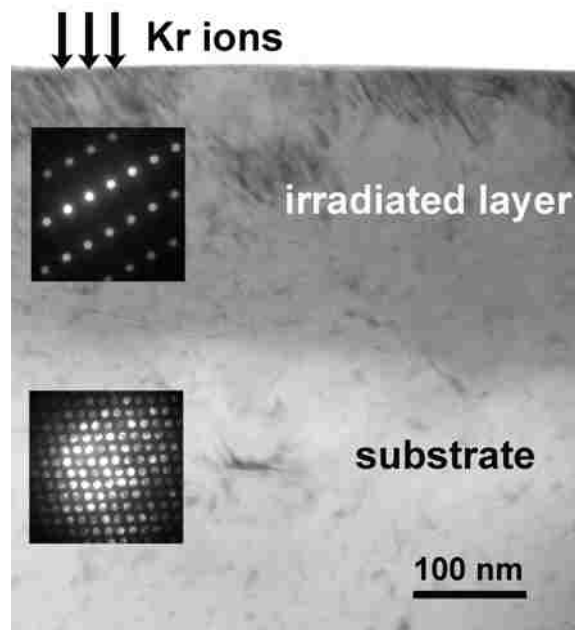


Figure 79: Cross-sectional TEM bright-field image and microdiffraction patterns (inset) for $Y_6U_1O_{12}$ irradiated to a fluence of 2 x $10^{20}$ $Kr/m^2$ (~50 dpa).

The structural changes observed in the high-dose ion irradiated δ-phase $Y_6U_1O_{12}$ sample were further investigated using high-resolution TEM (HRTEM). Figure 80 shows HRTEM micrographs obtained from the same sample as in Figure 79 at the interface between lower irradiated layer and unirradiated substrate. These micrographs were obtained with the electron beam aligned along $\vec{B}$ = [121] with respect to the rhombohedral δ-phase $Y_6U_1O_{12}$ substrate (using the 3-index system for indexing hexagonal directions). In Figure 80, two distinct structural regions, labeled "substrate" and "irradiated", are apparent. Insets shown in Figure 80 are diffractograms obtained using the fast Fourier transform (FFT) method, from the substrate and irradiated regions in the HRTEM micrograph. These diffractograms are consistent with the μD patterns in Figure 79. The HRTEM observations confirm that $Kr^{++}$ ion irradiation induces an order to disorder transition in the buried irradiated layer of $Y_6U_1O_{12}$.
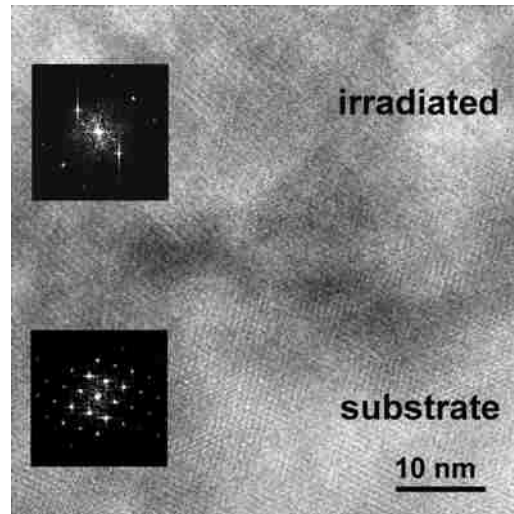


Figure 80: High-resolution TEM (HRTEM) micrographs obtained from the interface between the lower irradiated region and the unirradiated substrate in Fig. 74. The micrograph was obtained with the electron beam aligned along the [121] direction.

139

GIXRD and TEM observations indicate an irradiation-induced phase transformation in $Y_6U_1O_{12}$ from an ordered, δ-phase structure with rhombohedral symmetry to a fluorite phase with cubic symmetry by the highest experimental dose of ~50 dpa. We interpret this transformation to the cubic fluorite phase as an order-to-disorder (O-D) transformation, analogous to that seen in previous radiation damage studies on 6:1:12 uranium surrogate δ-phase compounds (δ-$Y_6W_1O_{12}$ and δ-$Y_6W_1O_{12}$ (63)). For irradiated delta phase compounds, cation antisite defects must form on the cation sublattice and anion Frenkel defects must be created on the anion sublattice in order to achieve this transformation. With this order to disorder transformation the rhombohedral symmetry of the ordered δ-phase vanishes in favor of cubic symmetry. These reactions lead the material transforms to a structure indistinguishable from the fluorite ($CaF_2$) crystal structure. We refer to this radiation-induced structure as a "disordered fluorite" phase.

It is interesting that δ-$Y_6U_1O_{12}$ compound irradiation result shows very strong amorphization resistance and remains crystalline to a high dose of 50 dpa, while uranium surrogate δ-phase compounds $Y_6W_1O_{12}$ and $Yb_6Y_1O_{12}$ undergo amorphous transitions at the same dose level. As well known, radiation-induced amorphization resistance is an inherent ability to accommodate atomic lattice disorder, including cation disorder on the A and B sites, as well as on a disordering of oxygen vacancies. The defect-formation energy has a significant effect on the susceptibility of the structure to radiation damage. Under irradiation, the lattice energy increase rapidly, especially in materials with a high defect formation energy. When the free energy of the crystalline structure during irradiation is greater than the free energy of the aperiodic state, the material is more easily amorphized.

To gain some insight into the defect processes responsible for disordering and amorphization under irradiation, we performed density functional theory (DFT) calculations to determine the energy to create an antisite pair in $Y_6U_1O_{12}$ and uranium surrogate $\delta$-phase compounds $Y_6W_1O_{12}$ and $Yb_6W_1O_{12}$ (65). We calculated the formation energy $E_f$ of a cation antisite pair via the relation $E_f = E_{(AB)} + E_{(BA)} - 2 \times E_{perfect}$ where $E_{(AB)}$ is the energy of a simulation cell with an A cation on a B site, $E_{(BA)}$ is the energy of a simulation cell with a B cation on an A site, and $E_{perfect}$ is the energy of a simulation cell of perfect delta phase. Figure 81 shows the DFT results for these three compounds in order of decreasing $A^{3+}/B^{6+}$ radius ratio, cation antisite formation energies of for $Y_6W_1O_{12}$, $Yb_6W_1O_{12}$ and $Y_6U_1O_{12}$ are $E_f$ =11.90, 10.25, 8.21 eV, respectively.
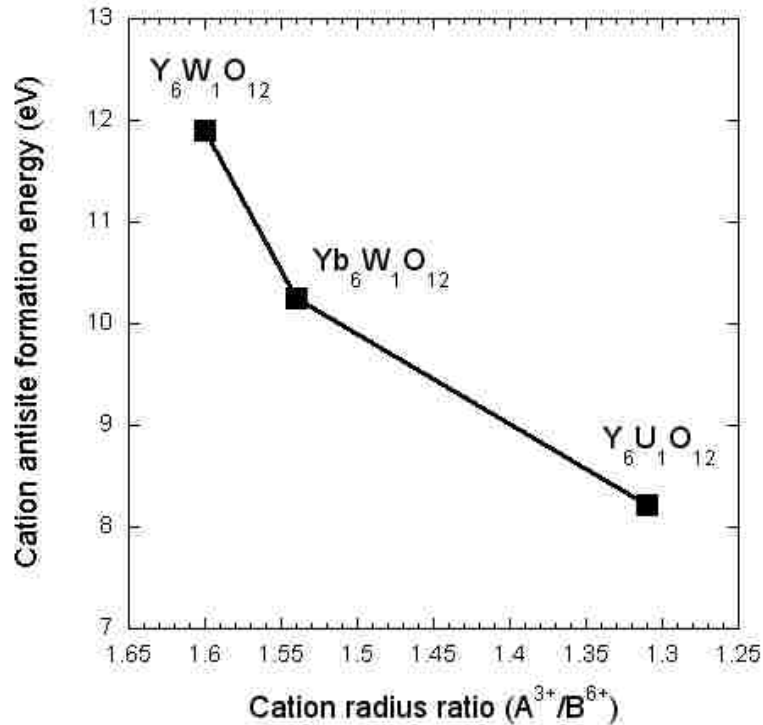


Figure 81: DFT calculations for the energy to form cation antisite in $Y_6U_1O_{12}$, $Y_6W_1O_{12}$ and $Yb_6Y_1O_{12}$ in order of decreasing $A^{3+}/B^{6+}$ radius ratio.

These are relatively large numbers, larger than equivalent energies found for other materials with empirical potentials (60). This suggests that disordering might be relatively difficult in these materials. However, the trends in disordering and amorphization tendencies predicted by these numbers show different agreements with the experimental results described above. The uranium compound has lower antisite formation energy suggesting that they will amorphize at higher dose. Exceptional resistance to radiation-induced amorphization in $Y_6U_1O_{12}$ is indeed observed experimentally, however, we do not observe $\delta-Y_6U_1O_{12}$ to undergo an ordered rhombohedral to disordered cubic fluorite transformation as readily as do the $\delta-Y_6W_1O_{12}$ and $\delta-Yb_6W_1O_{12}$ compounds.

The antisite formation energy in the uranium compound is quite high, suggesting that this material is strongly ordered. That a material with such a strong propensity for ordering does not amorphize under irradiation is interesting and challenges our previous understanding of amorphization resistance (60). However, the ability of a material to accommodate disorder via mechanisms such as antisite formation is only part of the story for amorphization resistance. Also of key importance is the number and types of defects produced during irradiation. It may be that in this material, because of the very high mass of the cations, the anions play the dominant role in absorbing the energy of the incoming radiation and dissipating it in the system. Future work will investigate the defect production and anion behavior in these materials.

We also note that the cation antisite formation energy is increased with the larger disparity between cation ionic radii in Figure 81. This large size difference is not favorable to cation antisite reactions, thus limiting the atomic mechanisms available for

142

lattice recovery from radiation damage. Clearly, the cation radius ratio of $Y_6U_1O_{12}$ is much smaller than that of tungsten compounds, which suggests $Y_6U_1O_{12}$ possesses more ability to accommodate disorder and greater stability for the crystalline. Work is in progress on additional uranium bearing 6:1:12 compounds to determine if the cation radius ratio and cation antisite formation energy are indeed important parameters in determining susceptibility to radiation-induced amorphization.

In summary, we performed Kr ion irradiation experiments under cryogenic conditions on polycrystalline δ-phase $Y_6U_1O_{12}$, and DFT calculations for the cation antisite formation energy. GIXRD measurements and TEM observations revealed δ-phase $Y_6U_1O_{12}$ possesses higher radiation resistance to amorphization than uranium surrogate δ-phase compounds $Y_6W_1O_{12}$ and $Yb_6Y_1O_{12}$. The material did, however, undergo an order to disorder transition at high doses (~ 50 dpa). The theoretical simulation also supports that $Y_6U_1O_{12}$ should be more resistant to radiation damage than the tungsten homolog due to the low cation antisite formation energy and similar cationic radii. This is further evidence that there is nothing mysterious about pyrochlore compounds and that the search for radiation tolerant material should aim toward structures that naturally accommodate disorder. The significance of the irradiation of $UY_6O_{12}$ is that it is the first, to our knowledge, demonstration of significant radiation tolerance (specifically amorphization resistance) in a fluorite derivative compound containing a substantial actinide concentration and irradiated to a substantial dose (greater than 10 dpa). This study is compared to the irradiation of the zirconia-magnesia inert matrix fuel in the following section.

## 6.3 Heavy ion irradiation of zirconia-magnesia inert matrix fuel

A uranium containing inert matrix fuel of the composition $Zr_{0.251}Mg_{0.728}U_{0.012}Er_{0.009}O_{1.27}$ was irradiated with 300 keV $Kr^{++}$ ions to a fluence of 2 x $10^{16}$ $Kr/m^2$ at liquid nitrogen temperatures. The sample was prepared as described in Section 3.2 and then polished to a mirror finish (1 micron). Structural changes were evaluated by GIXRD before and after the irradiation. The GIXRD patterns taken after the irradiation were collected at $0.25^o$, $0.5^o$, $0.75^o$ and $1.0^o$ incidence angle to probe different depths of the sample. Since the $Kr^{++}$ ions have a small penetration depth of a few hundred nanometers the incidence angle should be able to probe from only the irradiated layer at the most shallow angles to the irradiated layer and some of the substrate at higher angles. This allows identifying differences in the irradiated layer as compared to the substrate.

SRIM calculations were used to determine the dose due to the irradiation in displacements per atom and to estimate the amount of $Kr^{++}$ deposited in various depths of the sample. It was found that the maximum dose was ~ 42 dpa at 200 nm beneath the surface and that the damage extended to 600 nm below the surface. This is a relatively high dose, although lower than the 50 dpa used previously, for the material and the fluence used for this dose is the same as that for $UY_6O_{12}$. Even so, these two irradiations are close enough to be comparable for radiation tolerance purposes. The maximum concentration of $Kr^{++}$ in the sample is 2.3 atomic % at 300 nm and the $Kr^{++}$ range extends to 650 nm into the substrate. A graph of the dose and $Kr^{++}$ concentration as calculated by SRIM can be seen in Figure 82.
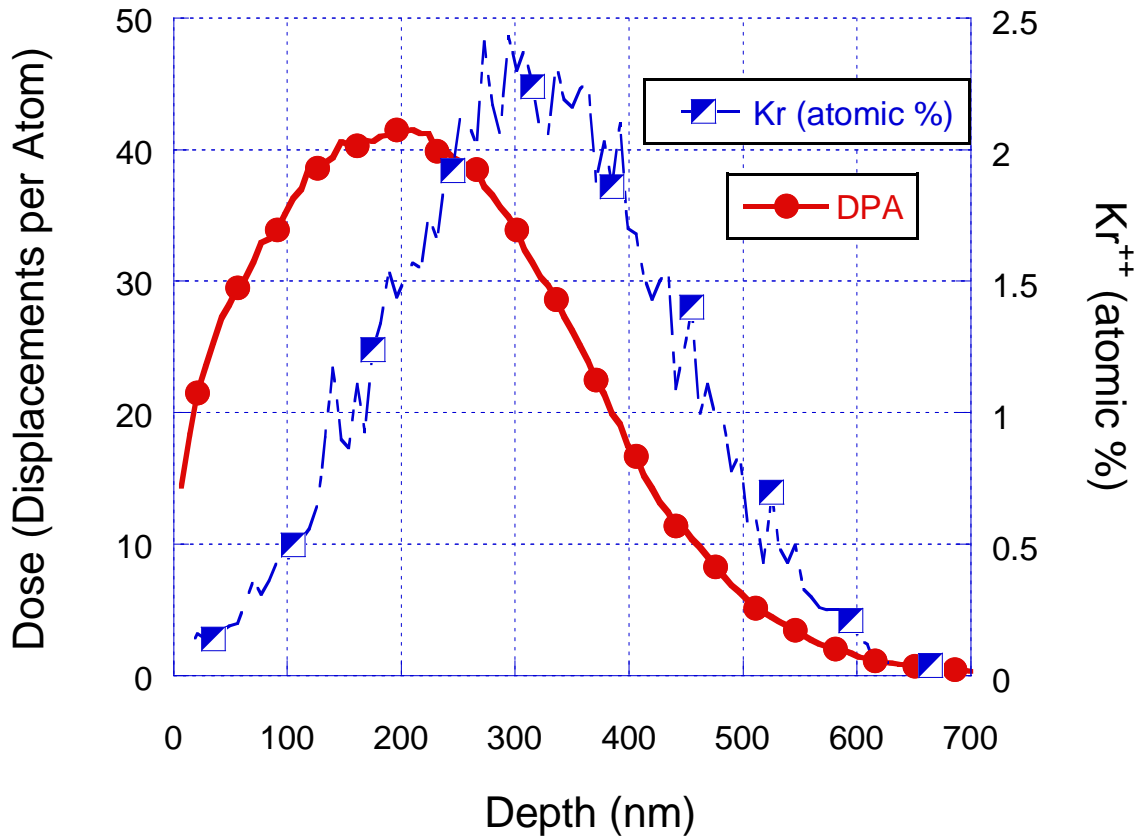
Figure 82: Dose in displacements per atom (DPA) and $Kr^{++}$ concentration as a function of penetration depth.

GIXRD was performed on the sample after irradiation to evaluate any changes in crystal structure (Figure 83). It can be seen that there are only the major fluorite peaks from both the zirconia phase and magnesia phase as there was in the pristine starting material (Figure 84). Furthermore, there is no change in the pattern as the incident angle is changed. This suggests that there is no difference between the irradiated material and the substrate. Not only is there no change in intensity, but there is little peak broadening as was seen in the irradiation of $UY_6O_{12}$. There is no ordered sub-lattice, so there is no possibility of an order to disorder transition. The disordered fluorite structure lends itself

to accommodating any cation on any cation site and oxygen vacancies can also distribute themselves in a random fashion. This minimizes the stored energy within the lattice and will therefore accommodate high radiation fields without amorphization.
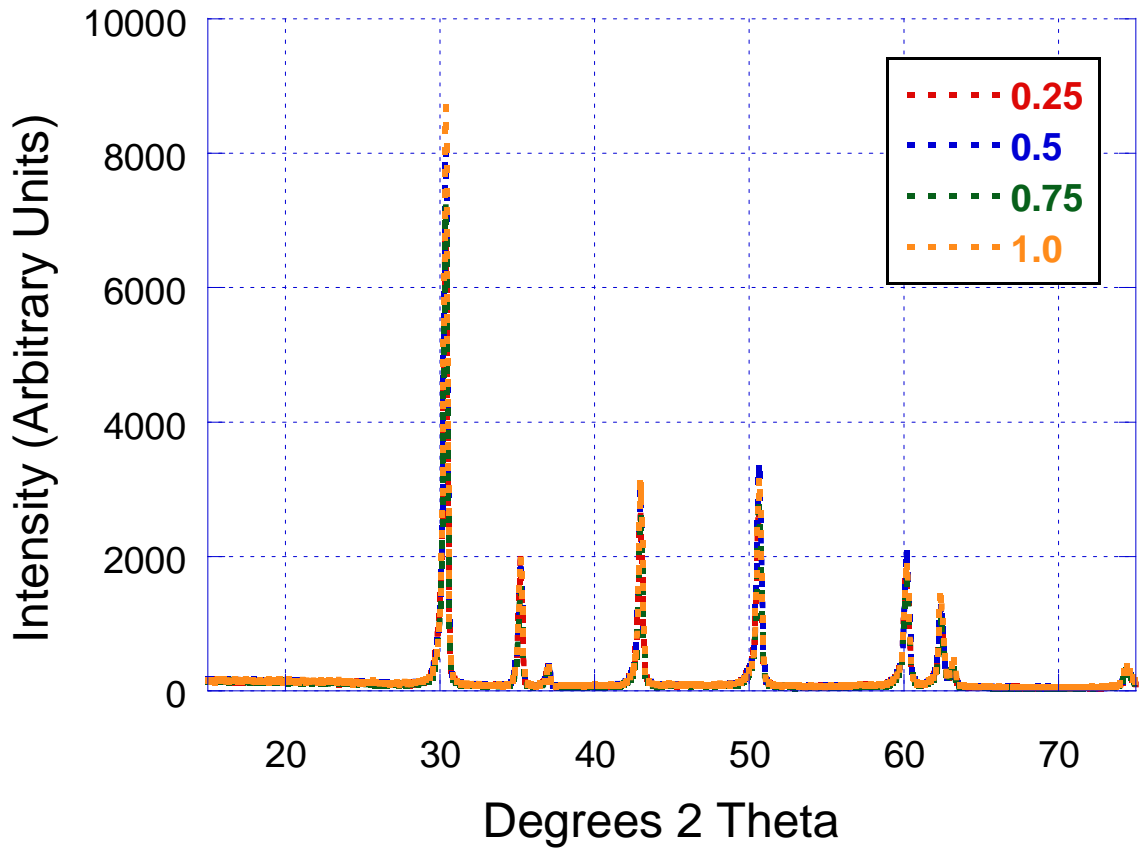


Figure 83: Grazing Incidence X-ray Diffraction pattern of irradiated uranium containing zirconia-magnesia inert matrix fuel at 0.25, 0.5, 0.75 and 1.0 $^{\circ}$ incident angle.

This is a significant finding for a number of reasons. It validates the theories put forth by Sickafus et. al. (60). The disordered fluorite structure has superior radiation tolerance in terms of amorphization resistance, because it is able to accommodate disorder within the lattice without accumulating a significant amount of lattice energy.

This irradiation study also validates the solubility studies performed on the synthesized material as the material remains unchanged and should therefore behave similarly. It will be necessary to repeat the studies with irradiated material to confirm the behavior of the material. The fact that the material does not undergo any significant change, however, is a good indication that the irradiated material will perform similar to the as unirradiated synthesized material. This confirms that zirconia-magnesia inert matrix fuel will not undergo any significant structural changes due to radiation damage to high dose (~ 42 dpa).
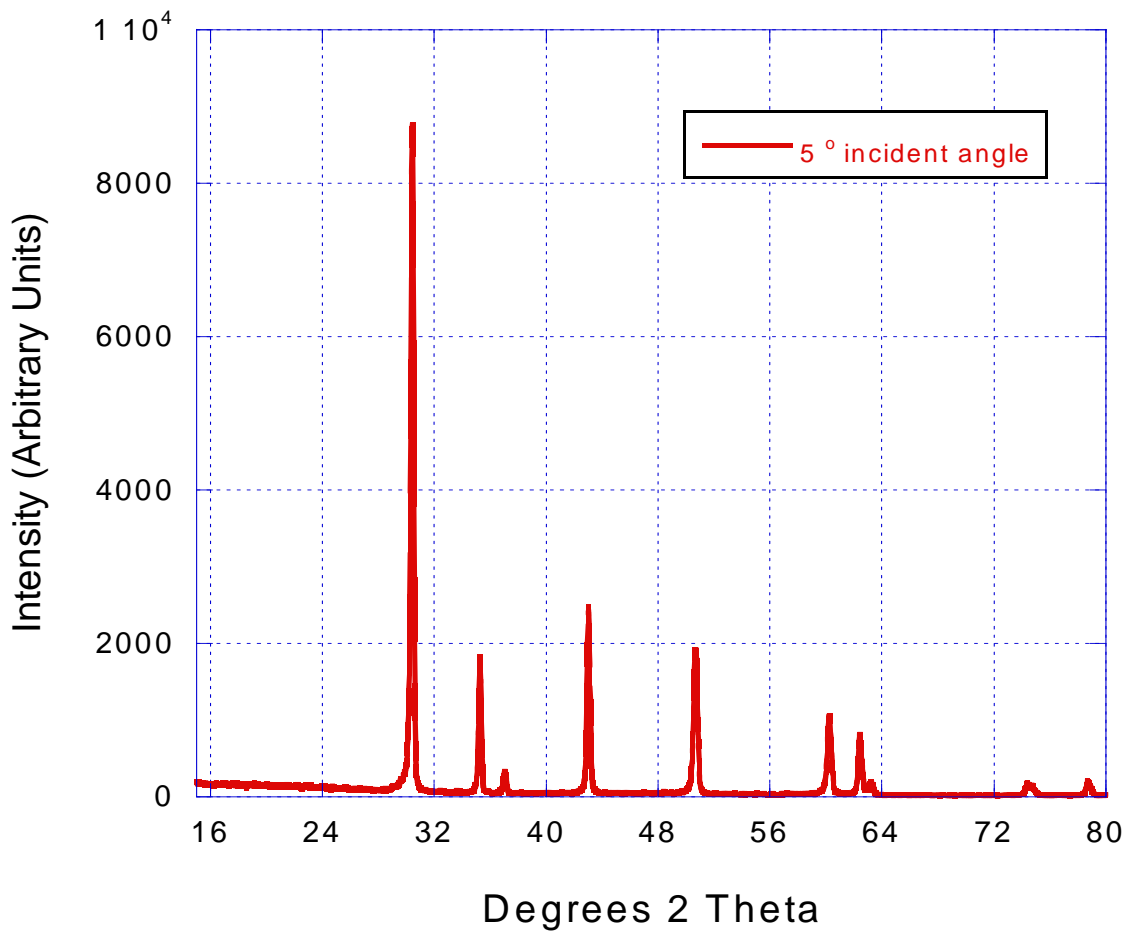


Figure 84: GIXRD pattern of pristine $Zr_{0.251}Mg_{0.728}U_{0.012}Er_{0.009}O_{1.27}$.

6.4 Conclusions from heavy ion irradiations

It was proposed by Sickafus et. al. (60) that radiation tolerance (particularly amorphization resistance) in fluorite structural derivatives can be predicted from temperature - composition phase diagrams. Furthermore, it is favorable to amorphization resistance in order to be able to accommodate disorder in the form of cation antisite and anion Frenkel defects. The energy required to make these defects is a good indication of temperature – composition diagram features and therefore radiation induced amorphization resistance. If it is possible to accommodate these defects with a minimal amount of energy, then the material will be highly radiation tolerant. Therefore, one of the best possible options for a radiation tolerant material is a disordered fluorite.

To test this theory a fluorite derivative, $UY_6O_{12}$, was irradiated to high dose and compared to irradiations of uranium surrogate compositions of $WY_6O_{12}$ and $WYb_6O_{12}$. It was found through density functional theory (DFT) calculations that the energy of a cation antisite and Frenkel defect pair are lower in the uranium compound than in the tungsten surrogate compounds. It is therefore predicted that the uranium compound will have a greater ability to accommodate disorder and therefore not undergo amorphization as easily as the tungsten compounds. Under irradiation studies to a dose of ~ 50 dpa it was found that $UY_6O_{12}$ undergoes an order to disorder transition, but no amorphization. This is further evidence of the ability to predict radiation tolerance from T – C phase diagrams.

Finally, the uranium containing zirconia-magnesia inert matrix fuel with the composition $Zr_{0.251}Mg_{0.728}U_{0.012}Er_{0.009}O_{1.27}$ was irradiated. It was found that the material did not change in any way detectable by GIXRD. The GIXRD patterns probing different

depths of the material show no difference in structure and are identical to the pristine starting material. This further supports the superior radiation tolerance, at least to amorphization resistance, of disordered fluorite structures which is well described by Sickafus et. al. (60). This also supports dissolution studies performed on as synthesized material as there was no change in chemical structure. It is shown that the material should undergo little to no change with use as an advanced fuel or waste form. Therefore, the as synthesized material should behave similar to the irradiated material in dissolution studies as long as the material is compared to that of similar dose as calculated by SRIM.

CHAPTER 7

CONCLUSIONS AND RECOMMENDATIONS

7.1 Synthesis and characterization

The precipitation method used to synthesize zirconia magnesia inert matrix ceramics has been used to produce dual phase material with intimate mixing between phases. It has also been shown to form a solid solution at less severe temperatures (510 $^{o}$C) and durations than the corresponding dry synthesis route as demonstrated by TGA/DSC [Figure 6]. This could be beneficial for burning higher actinides with low sublimation temperatures, such as americium. The $ZrO_2$ requires very little MgO in the presence of $CeO_2$ and $Er_2O_3$ to fully stabilize the cubic zirconia phase. This zirconia phase can accommodate up to 14 % (wt/wt) fissile material and up to 12 % (wt/wt) burnable poison. A consistent 5 % (wt/wt) MgO is contained in the zirconia phase allowing for a reliable estimate of the quantity of the periclase phase that will be present for a given composition. The relative amount of Mg is found to determine the phase composition of the resulting material. With no MgO, $ZrO_2$ is in both baddeleyite and tetragonal phases. As little as 3.2 % (wt/wt) and as much as 6.9 % (wt/wt) MgO resulted in a single cubic zirconia phase. A MgO (periclase) phase precipitated at MgO concentrations at and above 11.5 % (wt/wt) MgO. A third phase of cubic Ce-Er oxide was found after exceeding the solubility limit of the zirconia. This was found at $ZrO_2$ concentration of 30 % (wt/wt) with Ce and Er concentrations of 8.3 % and 5.2 % (wt/wt) respectively. This phase is also present in the absence of zirconia. The periclase phase remains pure which will allow it to retain its thermophysical properties, most importantly thermal diffusivity

and thermal conductivity, and to further improve the reactor-related qualities of the overall ceramic.  This characterization study was performed to lay a foundation for dissolution studies of zirconia-magnesia inert matrix fuel under conditions relevant to an advanced fuel cycle with uranium and plutonium [Table 6].

Uranium containing inert matrix ceramic was successfully synthesized in a two phase ceramic consisting of cubic zirconia and periclase.  The periclase phase remains pure showing a low affinity for all other cations in the ceramic, which will allow the periclase phase to retain its thermophysical properties, most importantly thermal conductivity and thermal diffusivity.  Magnesium, uranium, and erbium are able to substitute in the zirconia lattice at different levels to create a solid solution.  Magnesium concentrations within the zirconia phase remains constant at 5 wt. %.  Uranium and erbium concentrations within the zirconia were as high as 20 and 10 % (wt/wt) respectively.  These findings are confirmed by x-ray diffraction and electron microprobe analysis and further agree with previous studies performed with cerium as a plutonium homolog although the solubility limit for uranium was found to be higher than that of cerium within the zirconia under these conditions.  The higher solubility limit for uranium in zirconia as compared to cerium is an important deviation in behavior between the actinides and the lanthanide homolog.  The bond deformation due to the incorporation of uranium into the zirconia lattice was determined in the first two atomic shells by XAFS [Table 8].

A zirconia-magnesia simulated inert matrix fuel containing plutonium oxide as the fissile material and erbium oxide as a burnable poison was successfully synthesized as a dual phase ceramic using a precipitation method over a range of compositions.  This

151

material was characterized by x-ray diffraction in an effort to identify and quantify crystalline phases present. It was shown in most samples that the material consisted of cubic zirconia and cubic MgO (periclase). Optical microscopy was used to visualize phase mixing, microstructure, and pore space. Electron probe microanalysis was used to map elemental concentrations over wide areas. This demonstrated the homogeneity of each phase and confirmed that plutonium and erbium are incorporated into the zirconia phase resulting in a solid solution. This will simplify modeling and achieved new findings from this work. Secondary electron microscopy equipped with energy dispersive spectroscopy was used to determine the stoichiometry of each phase. It was determined that the periclase phase was pure MgO. This will allow it to retain its heat transfer properties, specifically thermal diffusivity and thermal conductivity. Analysis of the zirconia phase shows a presence of all cations involved to different concentrations. Magnesium is incorporated into the zirconia at 3-4 wt. % which defines the limit of isomorphic substitution for magnesium in zirconia under these conditions. The solubility limits of plutonium and erbium in zirconia were not reached, however the highest concentration of plutonium and erbium found in the zirconia were 16 and 12 wt. %, respectively. This high solubility limit will allow fissile material to be loaded into the fuel even at low concentrations of zirconium oxide. These studies established that a dual phase composition of cubic zirconia solid solution and magnesium oxide can be achieved with plutonium and erbium oxide.

## 7.2 Aqueous dissolution

Aqueous dissolution studies were performed with cerium oxide containing inert matrix ceramic in order to establish protocols and validate procedures with non-radioactive material.  These studies have also been used to assess the effectiveness of cerium as a plutonium homolog both structurally and chemically.  Soxhlet corrosion studies have found that zirconia is a highly resilient material that does not dissolve or release cations incorporated into its matrix in aqueous media as tested in these experiments.  The corrosion of the material is dictated by its magnesium oxide content.  Once this magnesium oxide concentration is greater than 30 wt. % there is a measurable corrosion rate.  This corrosion rate increases by almost an order of magnitude when the magnesium oxide concentration is nearly doubled to 56 wt. %.  Experiments were performed to simulate dissolution under reactor conditions in the event of a cladding failure.  These experiments performed with turbid water at 300 $^{\circ}$C found that the fuel pellet was physically destroyed within 48 hours, but there was no evidence of dissolution of the zirconia phase or any of its components for up to 250 hours.  These studies have been effective in establishing parameters and procedures to be used with actinide containing inert matrix fuel.

Aqueous dissolution studies with inert matrix ceramic containing uranium oxide as a fissile component and plutonium oxide homolog and erbium oxide as a burnable poison were performed for corrosion resistance should the fuel be adopted for a "once through then out" fuel cycle scheme.  A Soxhlet corrosion study was performed to quantify the mass loss of the material with different magnesia to zirconia ratios over long periods of time (>2,000 hours).  It was found that samples with magnesium oxide content up to 30

wt. % showed minimum corrosion rates due to the stabilizing effect of zirconia. Samples with magnesium oxide content of 60 wt. % or more showed no stabilizing effect from zirconia and had corrosion rates similar to that of samples with an inert matrix of pure magnesium oxide. A moderate magnesium oxide concentration of 45 wt. % displayed an intermediate corrosion rate. It is proposed that the corrosion of samples containing high zirconium oxide concentration is dominated by corrosion along the surface. Higher magnesium oxide concentrations lead to $Mg(OH)_2$ formation along grain boundaries dislodging entire grains leading to accelerated corrosion rates.

A pulse flow dissolution study [Section 2.10] was conducted with three sample compositions of varying magnesium oxide to zirconium oxide ratios in three solutions (deionized water, silicate-bicarbonate solution, and brine). There was no evidence of zirconium, uranium, or erbium in solution for any sample by ICP-AES indicating that the cubic zirconia phase remained in tacked and no cations were leached from the phase, with a detection limit of 0.03 mM. This will immobilize the material even in the event that the pellet is physically destroyed through the corrosion of the magnesia phase. The pellets were physically destroyed to different degrees due to the dissolution of the magnesium oxide phase. Rate and degree of corrosion was found to be proportional to magnesium oxide content, which is consistent with the Soxhlet study. Magnesium oxide hydration and dissolution was followed by SEM imaging and XRD analysis. Brine was found to be the most corrosive solution followed by deionized water. Silicate-bicarbonate solution was found to be the least corrosive due to the formation of a magnesium silicate on the surface that prohibits further corrosion. This protective layer does not fully prohibit corrosion at magnesium oxide concentrations greater than 45 wt.

%.  This study confirms the corrosion mechanism proposed by previous studies and expands that knowledge to solutions relevant to environmental conditions.  It further quantifies the limits at which zirconia is significantly stabilizing the magnesium oxide to corrosion by water.

Pressure vessel dissolution studies have shown that the pellet is physically destroyed through the mechanical destruction and dissolution of the magnesium oxide phase by turbid water at 300 $^\circ$C and pressures of 10.3 MPa.  This is a significant difference from those studies performed in static water at 300 $^\circ$C (53).  The zirconia phase remains unchanged and there is no evidence of the release of any uranium or erbium by ICP-AES.

The goal of the aqueous dissolution studies with plutonium was to evaluate the simulated inert matrix fuel containing actual fissile material and burnable poison in reactor and repository conditions.  The inert matrix dissolution was well characterized by dissolution studies with uranium.  The advantage of plutonium is its relatively high specific activity that can be used to significantly lower the detection limit of the material by liquid scintillation counting when compared to ICP-AES.  Even with this lower detection limit it was found that less than 0.8 wt. % of the plutonium is released in static 300 $^\circ$C water.  This study also confirmed previous studies on pellet integrity under these conditions and validates the differences found between static and turbid water corrosion properties.   As a waste form zirconia does not appear to have any corrosion at all within the scope of this study.  The release of plutonium in waste form dissolution studies was found to be less than 0.01 wt. %, which is the detection limit under these experimental conditions.  This material performs extremely well under aqueous dissolution and proves to be a robust material under both reactor and repository conditions.

## 7.3 Acidic dissolution

The main focus of dissolution studies with cerium was to use it as a non-radioactive homolog for actinides within the inert matrix ceramic and to establish methods and protocols that would be applied to studies with actinides. This proved to be invaluable in establishing procedures. The second goal of these studies was to evaluate the effectiveness of cerium as a homolog for uranium and plutonium. It was established in this study that cerium containing zirconia is insoluble in high concentrations of nitric acid. It proved to be somewhat soluble in sulfuric acid. Cerium and erbium follow first order dissolution kinetics in sulfuric acid medium. The kinetics of zirconium and magnesium were not determined due to inconsistent concentrations found in solution. Also, the ceramic was not completely dissolved and a large amount of solid residue remained after 48 hours. These studies are performed in greater detail with uranium to evaluate the solubility of the material in various acids.

Studies using uranium in an inert matrix were successful in testing possibilities for dissolution as a first step in reprocessing. These studies were unique in that they incorporated an actinide as a fissile component and erbium oxide as a burnable poison. It was found that this is vital to accurately represent the dissolution behavior of the ceramic and that uranium has a different chemical behavior than cerium, a common actinide homolog, under these conditions. This is best illustrated in the dissolution behavior of the material in concentrated nitric acid. It was shown that at low levels of zirconium oxide, the high concentration of uranium within the zirconia phase and high surface area to volume of that phase enables the leaching of uranium, erbium, and magnesium from the zirconia lattice. At significantly high levels of these substituting ions it is possible to

destabilize the lattice due to leaching and consequently dissolve the zirconia phase through a linear, incongruent dissolution process. This process does however require a great deal of time and only happens with specific chemical compositions. Because of this, sulfuric acid was also explored as a means of dissolving the ceramic. It was found that only 12 wt. % of the uranium in the sample was dissolved under current experimental conditions. This would mean that the cations involved will have a low solubility in the medium. In addition there is significant formation of colloids that conglomerate and settle to the bottom of the vessel. Both sulfuric and nitric acid pose problems to the dissolution of zirconia-magnesia inert matrix fuels. Further studies were performed with plutonium as the fissile component of the fuel and its chemical behavior was compared to that of the uranium and cerium homolog studies.

It was found that nitric acid is successful in at least partially dissolving plutonium from a zirconia matrix. It is proposed that the first 24 hours of dissolution is dominated by first order kinetics as the plutonium at the surface is dissolved by nitric acid. This was not observed in uranium due to detection limits. After 24 hours it is hypothesized that the kinetics will follow a linear trend due to the leaching of plutonium from the zirconia matrix leading to incongruent dissolution. This was observed in uranium and analysis of the plutonium data shows the rate to trend with both magnesium oxide content and concentration of plutonium within the zirconia phase as would be expected. This behavior in plutonium containing simulated inert matrix fuel is supported by fitting points taken after 24 hours to a line, which shows the same trends in rate as compared to composition that uranium samples did. The amount of plutonium in solution at any time is related to both the rate of dissolution and effective surface area of zirconia. This

effective surface area is why the sample with moderate magnesium and plutonium exhibited the greatest amount of dissolved plutonium after 48 hours. It was concluded that given the current kinetics model it would take between 30 and 70 days depending on composition and surface area to completely dissolve the plutonium from the material, which is only slightly faster than rates determined with uranium as the fissile component(70 to 160 days), which would also suggest similar kinetics.

Hydrofluoric acid and hydrogen peroxide were added to nitric acid to improve the dissolution kinetics of the experiment. It was found that in five wet ashing cycles it was possible to dissolve up to 81 wt. % of the plutonium from the matrix. This is significantly more and much faster than with nitric acid alone. The amount of plutonium dissolved continues to increase with each ashing, so it is expected to be possible to use this dissolution method for the complete dissolution of plutonium. The amount of plutonium dissolved did not trend with the physical or chemical properties that were measured. It is believed to be due to the effective surface area of the zirconia phase as was the case with nitric acid dissolution of uranium containing samples. It should also be noted that the HF-HNO$_3$-peroxide dissolution study was carried out with sample compositions that were more durable (higher zirconium oxide concentrations) than those that were carried out with nitric acid alone. Therefore, the sample compositions with greater concentrations of plutonium and magnesium oxides should dissolve faster and to a greater extent than the samples with higher zirconium oxide that were used for this study.

## 7.4 Radiation tolerance

It was proposed by Sickafus et. al. (60) that radiation tolerance (particularly amorphization resistance) in fluorite structural derivatives can be predicted from temperature - composition phase diagrams. Furthermore, it is favorable to exploit amorphization resistance to be able to accommodate disorder in the form of cation antisite and anion Frenkel defects. The energy required to make these defects is a good indication of temperature – composition diagram features and therefore radiation induced amorphization resistance. If it is possible to accommodate these defects with a minimal amount of energy, then the material will be highly radiation tolerant. Therefore, one of the best possible options for a radiation tolerant material is a disordered fluorite.

To test this theory a fluorite derivative, $UY_6O_{12}$, was irradiated to high dose and compared to irradiations of uranium surrogate compositions of $WY_6O_{12}$ and $WYb_6O_{12}$. It was found through density functional theory (DFT) calculations that the energy of a cation antisite and Frenkel defect pair are lower in the uranium compound than in the tungsten surrogate compounds [Section 6.2]. It is therefore predicted that the uranium compound will have a greater ability to accommodate disorder and therefore not undergo amorphization as easily as the tungsten compounds. Under irradiation studies to a dose of $\sim 50$ dpa it was found that $UY_6O_{12}$ undergoes a partial order to disorder transition, but no amorphization, while the tungsten surrogates amorphize at comparable doses. This is further evidence of the ability to predict radiation tolerance from T – C phase diagrams.

Finally, the uranium containing zirconia-magnesia inert matrix fuel with the composition $Zr_{0.251}Mg_{0.728}U_{0.012}Er_{0.009}O_{1.27}$ was irradiated to a dose of 42 dpa. It was found that the material did not change in any way detectable by GIXRD. The GIXRD

patterns probing different depths of the material show no difference in structure and are identical to the pristine starting material. This further supports the superior radiation tolerance, at least to amorphization resistance, of disordered fluorite structures which is well described by Sickafus et. al. (60). This also validates dissolution studies performed on as synthesized material. It is shown that the material should undergo little to no change with use as an advanced fuel or waste form. Therefore, the as synthesized material should behave similar to the irradiated material to a similar dose in dissolution studies.

## 7.5 Recommendations

The research presented in this thesis addressed several major hurdles to the feasibility of zirconia-magnesia inert matrix fuel. The first was in the synthesis of the material. It was established that a zirconia-magnesia inert matrix fuel could be synthesized with plutonium and erbium oxide via a coprecipitation method. This coprecipitation method allowed for solid solution formation at less extreme sintering temperatures and durations as compared to the dry synthesis route of mixing the oxide powders. The characterization of the material lead to the determination of the solubility limit of magnesium oxide in zirconia, under these conditions. The solubility limit of plutonium and erbium oxide in zirconia was not determined. It can be inferred through studies with cerium and uranium oxide, but it will be necessary to determine this explicitly in future work. Because of this, it was determined that the synthesis of this material was possible given the procedure outlined in this work.

The material that was synthesized in these studies was examined in two aqueous environments. The first was in reactor condition as a nuclear fuel in the event of a cladding failure. It was confirmed that the material is stable to static 300 $^{\circ}$C water, which was determined by earlier studies. Experiments done with turbid 300 $^{\circ}$C water revealed that the magnesia phase was not stable and the sample pellet was physically destroyed. There was less than 1 wt. % of the fissile material released from the zirconia, but since the physical integrity of the fuel was compromised this poses a problem to reactor safety. Further assessment of this scenario needs to be done to determine the effect this would have in an accident scenario. The second aqueous environment that was explored was environmental conditions should the inert matrix be used as the waste form in a once through fuel cycle scenario. Under these conditions the inert matrix performed exceptionally well with less than 0.01 wt. % of the plutonium released from the sample. The fuel pellet is physically destroyed in some conditions, but since the activity is trapped in the zirconia this is not expected to be of consequence. Further study should be performed on spent fuel to determine where other elements, such as fission products and minor actinides, are concentrated and whether they will become mobile under environmental conditions.

Several methods of dissolving the material were explored so that recycling could be an option for the spent fuel. It was determined that sulfuric and nitric acid were inadequate at dissolving the material in efficient quantities and times for reprocessing. Nitric acid dissolution did, however, reveal that a fissile component with multiple oxidation states is necessary to accurately model the chemical behavior of the fuel. Therefore dissolution studies should be performed on material that contains plutonium if

it is to be accurately described. Nitric acid with hydrofluoric acid and peroxide was successful in dissolving the material in a wet ashing procedure. Therefore, this method is recommended for further study to accurately describe the kinetics and solubility limits so that it could be used to dissolve spent zirconia-magnesia inert matrix fuel.

Irradiation studies performed on the material confirm its high tolerance to amorphization. A systematic study was performed to more accurately describe the mode in which materials fail in radiation testing. In this way a better understanding of radiation tolerant materials can lead to better selection methods. Because the zirconia-magnesia material does not undergo amorphization under high radiation dose it should be ideal as a fuel or waste form. The material's crystal structure did not change during irradiation and should therefore behave the same in dissolution studies as the synthesized material.

In conclusion, many of the issues associated with zirconia-magnesia inert matrix fuels were addressed in this work. The synthesis of the material was solved through a coprecipitation process. Compatibility with coolant water was identified as a subject for further study in accident scenarios. The material behaved extremely well as a waste form. A method was identified for dissolving the spent fuel so that reprocessing may be performed. Irradiation studies confirmed the durability of the material in high dose fields making it a suitable nuclear fuel and waste form. In short, zirconia-magnesia remains a promising material for use in advanced nuclear systems as a means of burning plutonium in existing pressurized water reactors.

# REFERENCES

(1)     Lombardi, C.; Luzzi, L.; Padovani, E.; Vettraino, F. *Progress in Nuclear Energy* **2008**, *50*, 944-953.

(2)     Schram, R.P.C.; Klaassen, F.C. *Progress in Nuclear Energy* **2007**, *49*, 617-622.

(3)     Albright, D.; Kramer, K. "ISIS Plutonium Watch, Tracking Plutonium Inventories." http://www.isis-online.org/global_stocks/plutonium_watch2004.pdf, **2004**, accessed June 15, 2009.

(4)     Lombardi, C.; Mazzola, A. *Ann. Nucl. Energy* **1996**, *23*, 1117-1126.

(5)     Rubin, B.; Berman, R.; Bleiberg, M. "The irradiation behavior of $ZrO_2$-$UO_2$ fuels." **1962**, Pittsburg, PA: Bettis Atomic Power Laboratory, Report WAPD-292.

(6)     Warner, H. "Evaluation of low-density single-phase cubic $ZrO_2$-$UO_2$ fuels stabilized by CaO." **1966**, Pittsburg, PA: Bettis Atomic Power Laboratory, Report WAPD-292

(7)     Berman, R. "The homogenization and densification of $ZrO_2$-$UO_2$ fuels stabilized by CaO." **1966**, Pittsburg, PA: Bettis Atomic Power Laboratory, Report WAPD-301.

(8)     Matzke, Hj.; Rondinella, V.V.; Wiss, T. *J. Nucl. Mat.* **1999**, *274*, 47-53.

(9)     Chawla, R.; Konings R.J.M. *Progress in Nuclear Energy*, **2001**, *38*, 455-458.

(10)    Degueldre, C.; Paratte, J.M. *J. Nucl. Mat.* **1999**, *274*, 1-6.

(11)    Krivitski, Yu.; Vorotyntsev, M.F.; Pyshin, V.K.; Korobeinikova, L.V. *Progress in Nuclear Energy* **2001**, *38*, 391-394.

(12)    Damen, P.M.G.; Kloosterman, J.L. *Progress in Nuclear Energy* **2001**, *38*, 371-374.

(13)    Carmack, W.J.; Todosow, M.; Meyer, M.K.; Pasamehmetoglu, K.O. *Journal of Nuclear Materials* **2006**, *352*, 276-285.

(14)    Burghartz, M.; Matzke, Hj.; Leger, C.; Vambenepe, G.; Rome, M. *Journal of Alloys and Compounds* **1998**, *271-273*, 544-548.

(15)    Kloosterman, J.L.; Damen, P.M.G. *Journal of Nuclear Materials* **1999**, *274*, 112-119.

(16)    Lombardi, C.; Mazzola, A.; Padovani, E.; Ricotti, M.E. *Journal of Nuclear Materials* **1999**, *274*, 181-188.

(17)    Wallenius, J. *Journal of Nuclear Materials* **2003**, *320*, 142-146.

(18)    Gosset, D.; Provot, B. *Progress in Nuclear Energy* **2001**, *38*, 263-266.

(19)    Streit, M.; Ingold, F.; Pouchon, M.; Gauckler, L.J.; Ottaviani, J.P. *Journal of Nuclear Materials* **2003**, *319*, 51-58.

(20)    Noirot, J.; Desgranges, L.; Chauvin, N.; Georgenthum, V. *Journal of Nuclear Materials* **2003**, *320*, 117-125.

(21)    Klaassen, F.C.; Bakker, K.; Schram, R.P.C.; Meulekamp, R. Klein; Conrad, R.; Somers, J.; Konings, R.J.M. *Journal of Nuclear Materials* **2003**, *319*, 108-117.

(22)    Lutique, S.; Konings, R.J.M.; Rondinella, V.V.; Somers, J.; Wiss, T. *Journal of Alloys and Compounds* **2003**, *352*, 1-5.

(23)    Schneider, E.A.; Deinert, M.R.; Herring, S.T.; Cady, K.B. *Journal of Nuclear Materials* **2007**, *361*, 41-51.

(24)    Chauvin, N.; Konings, R.J.M.; Matzke, Hj. *Journal of Nuclear Materials* **1999**, *274*, 105-111.

(25)     Nakano, Y.; Akie, H.; Magara, M.; Takano, H. *Journal of Nuclear Materials* **1999**, *274*, 127-134.

(26)     Arima, Tatsumi; Yamasaki, Sho; Torikai, Satoshi; Idemitsu, Kazuya; Inagaki, Yaohiro; Degueldre, Claude *Journal of Nuclear Materials* **2005**, *398*, 296-303.

(27)     Sobolev, V.; Lemehov, S. *Journal of Nuclear Materials* **2006**, *352*, 300-308.

(28)     Degueldre, C.; Arima, T.; Lee, Y.W. *Journal of Nuclear Materials* **2003**, *319*, 6-14.

(29)     Arima, T.; Yamasaki, S.; Yamahira, K.; Idemitsu, K.; Inagaki, Y.; Degueldre, C. *Journal of Nuclear Materials* **2006**, *352*, 309-317.

(30)     Hellwig, Christian; Kasemeyer, Uwe; Ledergerber, Guido; Lee, Byung-Ho; Lee, Young-Woo; Chawla, Rakesh. *Annals of Nuclear Energy* **2003**, *30*, 287-299.

(31)     Ronchi, C.; Ottaviani, J.P.; Degueldre, C.; Calabrese, R. *Journal of Nuclear Materials* **2003**, *320*, 54-65.

(32)     Ledergerber, G.; Degueldre, C.; Heimgartner, P.; Pouchon, M.A.; Kasemeyer, U. *Progress in Nuclear Energy* **2001**, *38*, 301-308.

(33)     Hellwig, Ch.; Pouchon, M.; Restani, R.; Ingold, F.; Bart, G. *Journal of Nuclear Materials* **2005**, *340*, 163-170.

(34)     Thridandapani, R.R.; Folgar, C.E.; Folz, D.C.; Clark, D.E.; Wheeler, K.; Peralta, P. *Journal of Nuclear Materials* **2009**, *384*, 153-157.

(35)     Lee, Y.W.; Kim, H.S.; Kim, S.H.; Joung, C.Y.; Na, S.H.; Ledergerber, G.; Heimgartner, P.; Pouchon, M.; Burghartz, M. *Journal of Nuclear Materials* **1999**, *274*, 7-14.

(36)    Schram, R.P.C.; van der Laan, R.R.; Klaassen, F.C.; Bakker, K.; Yamashita, T.; Ingold, F. *Journal of Nuclear Materials* **2003**, *319*, 118-125.

(37)    Degueldre, C.; Pouchon, M.; Streit, M.; Zaharko, O.; Di Michiel, M. *Progress in Nuclear Energy* **2001**, *38*, 241-246.

(38)    Curran, Gini; Sevestre, Y.; Rattray, Wendy; Allen, Patrick; Czerwinski, K.R. *Journal of Nuclear Materials* **2003**, *323*, 41-48.

(39)    Serizawa, H.; Nakajima, K.; Arai, Y.; Yamashita, T.; Kuramoto, K.; Kinoshita, H.; Yamanaka, S.; Uno, M.; Kurosaki, K. *Progress in Nuclear Energy* **2001**, *38*, 237-240.

(40)    Corcoran, E.C.; Lewis, B.J.; Thompson, W.T.; Hood, J.; Akbari, F.; He, Z.; Reid, P. *Journal of Nuclear Materials* **2009**, *385*, 424-430.

(41)    Kamel, N.; Ait-Amar, H.; Taouinet, M.; Benazzouz, C.; Kamel, Z.; Fodil-Cherif, H.; Telmoune, S.; Slimani, R.; Zahri, A.; Sahel, D. *Progress in Nuclear Energy* **2006**, *48*, 70-84.

(42)    Rice, R.W. *Journal of Materials Science* **1997**, *32*, 3071-3087.

(43)    van Veen, A.; Konings, R.J.M.; Fedorov, A.V. *Journal of Nuclear Materials* **2003**, *320*, 77-84.

(44)    Garrido, Frederico; Vincent, Laetitia; Nowicki, Lech; Sattonnay, Gael; Thome, Lionel *Nuclear Instruments and Methods in Physics Research B* **2006**, *266*, 2842-2847.

(45)    Hellwig, Ch.; Streit, M.; Blair, P.; Tverberg, T.; Klaassen, F.C.; Schram, R.P.C.; Vettraino, F.; Yamahita, T. *Journal of Nuclear Materials* **2006**, *352*, 291-299.

(46)    Restani, R.; Martin, M.; Kivel, N.; Gavillet, D. *Journal of Nuclear Materials* **2009**, *385*, 435-442.

(47)    Streit, M.; Wiesenack, W.; Tverberg, T.; Hellwig, Ch.; Oberlander, B.C. *Journal of Nuclear Materials* **2006**, *352*, 349-356.

(48)    Degueldre, C.; Hellwig, Ch. *Journal of Nuclear Materials* **2003**, *320*, 96-105.

(49)    Matzke, Hj.; Rondinella, V.V.; Wiss, T. *Journal of Nuclear Materials* **1999**, *274*, 47-53.

(50)    Vettraino, F.; Magnani, G.; La Torretta, T.; Marmo, E.; Coelli, S.; Luzzi, L.; Ossi, P.; Zappa, G. *Journal of Nuclear Materials* **1999**, *274*, 23-33.

(51)    Haeck, W.; Malambu, E.; Sobolev, V.P.; Ait Abderrahim, H. *Journal of Nuclear Materials* **2006**, *352*, 285-290.

(52)    Chauvin, N.; Albiol, T.; Mazoyer, R.; Noirot, J.; Lespiaux, D.; Dumas, J.C.; Weinberg, C.; Menard, J.C.; Ottaviani, J.P. *Journal of Nuclear Materials* **1999**, *274*, 91-97.

(53)    Imaura, A.; Touran, N.; Ewing, R.C. *Journal of Nuclear Materials* **2009**, *389*, 341-350.

(54)    Neeft, E.A.C.; Bakker, K.; Belvroy, R.L.; Tams, W.J.; Schram, R.P.C.; Conrad, R.; van Veen, A. *Journal of Nuclear Materials* **2003**, *317*, 217-225.

(55)    Neeft, E.A.C.; Bakker, K.; Buurveld, H.A.; Minkema, J.; Paardekooper, A.; Schram, R.P.C.; Sciolla, C.; Zwaagstra, O.; Beemsterboer, B.; Woittiez, J.R.W.; van Vlaanderen, P.; Tams, W.J.; Hein, H.; Conrad, R.; van Veen, A. *Progress in Nuclear Energy* **2001**, *38*, 427-430.

(56)     Neeft, E.A.C.; Bakker, K.; Schram, R.P.C.; Conrad, R.; Konings, R.J.M. *Journal of Nuclear Materials* **2003**, *320*, 106-116.

(57)     Shukla, P.; Watanabe, T.; Nino, J.C.; Tulenko, J.S.; Phillpot, S.R. *Journal of Nuclear Materials* **2008**, *380*, 1-7.

(58)     Ebert, Fritz; Cohn, Ernst *Z. anorg. U. allgem. Chem.* **1933**, *213*, 321-332.

(59)     Duwez, Pol; Odell, Francis; Brown, Frank H. *Journal of the American Chemical Society* **1952**, *35*.

(60)     Yin, Y.; Argent, B.B. *Journal of phase equilibria* **1993**, *14*, 439-450.

(61)     Scott, H.G. *Journal of the Australian Ceramic Society* **1981**, *17*, 16-20.

(62)     Montross, Charles S. *British Ceramic, Transactions and Journal* **1991**, *90*, 175-178.

(63)     Medvedev, Pavel "Development of dual phase magnesia-zirconia ceramics for light water reactor inert matrix fuel." Ph.D. Dissertation, Texas A&M University, December 2004.

(64)     Medvedev, P.G.; Frank, S.M.; O'Holleran, T.P.; Meyer, M.K. *Journal of Nuclear Materials* **2005**, *342*, 48-62.

(65)     Medvedev, P.G.; Lambregts, M.J.; Meyer, M.K. *Journal of Nuclear Materials* **2006**, *349*, 167-177.

(66)     Medvedev, P.G.; Jue, J.F.; Frank, S.M.; Meyer, M.K. *Journal of Nuclear Materials* **2006**, *352*, 318-323.

(67)     Holliday, Kiel; Hartmann, Thomas; Czerwinski, Ken *Journal of Nuclear Materials* **2009**, doi:10.1016/j.jnucmat.2009.04.013.

(68) Fridman, E.; Shwageraus, E.; Galperin, A. *Nuclear Technology* **2007**, *157*, 157-176.

(69) Holliday, Kiel; Hartmann, Thomas; Poineau, Frederic; Kennedy, J. Rory; Czerwinski, Ken *Journal of Nuclear Materials* **2009**, doi:10.1016/j.jnucmat.2009.06.007.

(70) Holliday, Kiel; Hartmann, Thomas; Czerwinski, Ken *Journal of Nuclear Materials* submitted 2009.

(71) Sickafus, Kurt E.; Grimes, Robin W.; Valdez, James, A.; Cleave, Antony; Tang, Ming; Ishimaru, Manabu; Corish, Siobhan M.; Stanek, Christopher R.; Uberuaga, Blas P. *Nature Materials* **2007**, *6*, 217-223.

(72) Ondik, H.M.; McMurdie, H.F. *Westerville: The American Chemical Society* **1998**.

(73) Wang, S.X.; Begg, B. D.; Wang, L. M.; Ewing, R. C.; Weber, W. J.; Kutty, K. V. Govidan *J. Mater. Res.* **1999**, *14*, 4470-4473.

(74) Tang, M.; Valdez, J.A.; Sickafus, K.E. *Journal of Nuclear Materials* **2008**, *376*, 247.

(75) Ziegler, J.F.; Biersack, J.P.; Littmark, U. *The Stopping and Range of Ions in Solids* New York: Pergamon Press, **1985**.

(76) Tang, M.; Valdez, J.A.; Holliday, K.S.; Uberuaga, B.P.; Dickerson, P.O.; Dickerson, R.M.; Wang, Y.; Czerwinski, K.; Sickafus, K.E. *Journal of Nuclear Materials* **2009**, *389*, 497-499.

VITA

Graduate College
University of Nevada, Las Vegas

Kiel Steven Holliday

Local Address:
2675 Windmill Pkwy. #2911
Henderson, NV 89074

Home Address:
21818 Glen View Dr.
Moreno Valley, CA 92557

Degrees:
Bachelor of Science, Chemistry, 2005
California State University, San Marcos

Special Honors and Awards:
Eagle Scout

Publications:
Tang, M; Holliday, K.S.; Valdez, J.A.; Uberuaga, B.P.; Dickerson, P.O.; Dickerson, R.M.; Wang, Y.; Czerwinski, K.; Sickafus, K.E. "Radiation damage effects in uranium bearing delta-phase oxide $Y_6U_1O_{12}$." Journal of Nuclear Materials (2009), 389, 497-499.

Holliday, Kiel; Hartmann, Thomas; Czerwinski, Ken. "Synthesis and characterization of zirconia-magnesia inert matrix fuels: cerium homolog studies." Journal of Nuclear Materials doi:10.1016/j.jnucmat.2009.04.013.

Holliday, Kiel; Hartmann, Thomas; Poineau, Frederic; Czerwinski, Ken. "Synthesis and characterization of zirconia-magnesia inert matrix fuels: uranium homolog studies." Journal of Nuclear Materials doi:10.1016/j.jnucmat.2009.06.007.

Dissertation Title: Zirconia-Magnesia Inert Matrix Fuel and Waste Form: Synthesis, Characterization and Chemical Performance in an Advanced Fuel Cycle.

Dissertation Examination Committee:
Chairperson, Dr. Ken Czerwinski, Ph.D.
Committee Member, Dr. Gary Cerefice, Ph.D.
Committee Member, Dr. Kurt Sickafus, Ph.D.
Graduate Faculty Representative, Dr. Ralf Sudowe, Ph.D.